University of London
Imperial College of Science, Technology and Medicine
Department of Bioengineering

Improving the Translation of Super Resolution Ultrasound Using Projection Imaging and Microbubbles

Bingxue Wang

Submitted in part fulfilment of the requirements for the degree of
Doctor of Philosophy in Imperial College London, November 2023

Abstract

Visualizing the microvasculature can aid the diagnosis and therapeutic monitoring of diseases with aberrant blood vessel proliferation or cardiovascular conditions. Super-resolution ultrasound (SRUS) imaging has been demonstrated to reveal microvascular structures and flow with sub-diffraction resolution in deep tissues by identifying spatially separated ultrasonic contrast agents (UCA).

However, the clinical translation of this technology is hindered by various issues including the limited view of conventional 2D US imaging, the expensive equipment and computational cost of 3D US imaging, as well as the low detection efficiency of UCA.

The research was first focused on developing new imaging methods. A projection SRUS imaging approach was proposed, demonstrating the ability to expand the field of view to a level comparable to 3D SRUS imaging while maintaining the hardware and computing costs equal to the 2D SRUS imaging level, using the proposed new type of probe. The proposed approach was evaluated in simulation, in vitro, and in vivo. Results indicate that the proposed approach can visualize microvessels in a similar 3D volume as a fully 3D approach but with over an order of magnitude less transducer complexity and computational cost. Following that, an extension of this projection approach was proposed, using a revised design of the probe. The simulation, in vitro, and in vivo results show that improved imaging performance can be achieved with a minor cost increment.

Next, this study explored the use of a new type of contrast agent in SRUS. The performance of conventional commercialized polydispersed microbubbles versus recently developed monodispersed microbubbles was compared in 2D and 3D SRUS. Our initial results show that this new type of monodispersed contrast agent used in this study did not provide a significant advantage over existing ones in improving the UCA detection efficiency.

Acknowledgements

I would like to express my gratefulness to my supervisor Mengxing for his continuous support and guidance. I am also grateful to my supportive and humourous colleagues and co-authors. I would also thank my parents and my aunt for their unconditional support and belief. Last but not least, thank all these failures and successes during my investigations for helping me to know the boundaries of the world, science, and myself better.

Contents

Abstract **i**

Acknowledgements **iii**

1 Introduction **1**

1.1 Motivation and Objectives 1

1.2 Statement of Originality 3

1.3 Copyright Declaration 3

2 Background Theory **5**

2.1 Microvasculature 5

2.2 Microvascular Imaging Techniques 8

2.2.1 Optics 8

2.2.2 Photoacoustic 9

2.2.3 MRI 10

2.2.4 X-ray 11

2.2.5 Summary 14

2.3 Ultrasound Imaging 15

2.3.1 Transducer 16

2.3.2 Transmission and Reception 20

2.3.3 System Descriptions 21

2.4 Contrast-Enhanced Ultrafast Imaging 27

2.4.1 Contrast Agent 27

2.4.2 Contrast Enhanced Ultrasound Imaging 31

2.4.3 Ultrafast Ultrasound Imaging 35

2.4.4 Clutter Filtering 36

2.5 Super Resolution Ultrasound Imaging 39

2.5.1 2D Super Resolution Ultrasound 39

2.5.2 3D Super Resolution Ultrasound 39

2.6 Thesis aims and impact 41

2.6.1 Research objectives 41

2.6.2 Scientific Contribution 42

3 Projection SRUS Imaging **44**

3.1 INTRODUCTION 44

3.2 METHOD 45

3.2.1 Transducers 45

3.2.2 Simulation 47

3.2.3 Simulation Evaluation 48

3.2.4 *In vitro* Experiments 49

3.2.5 *In vivo* Experiments 51

3.2.6 Post-Processing 51

3.3 RESULTS 52

3.3.1 Simulation 52

3.3.2 *In vitro* Experiments 56

3.3.3 *In vivo* Experiments 57

3.4 DISCUSSION 58

3.5 CONCLUSION 63

4 Multi Aperture Projection SRUS Imaging 64

4.1 INTRODUCTION 64

4.2 METHOD 65

4.2.1 Transducers 65

4.2.2 Simulation 66

4.2.3 *In vitro* Experiments 68

4.2.4 *Ex vivo* Experiments 69

4.2.5 Post-Processing 69

4.3 RESULTS 70

4.3.1 Simulation 70

4.3.2 *In vitro* Experiments 73

4.3.3 *Ex vivo* Experiments 74

4.4 DISCUSSION 74

4.5 CONCLUSION 77

5 SRUS using Monodispersed Microbubbles **79**

5.1 Introduction 79

5.2 Method 81

5.2.1 Simulation 81

5.2.2 *In Vitro* Experiment 85

5.3 Result 86

5.3.1 Simulation 86

5.3.2 *In Vitro* Experiment 93

5.4 Discussion 95

5.5 Conclusion 98

6 Conclusion **99**

6.1 Summary of Thesis Achievements 99

6.2 Future Work 99

Bibliography **104**

List of Tables

2.1 Simulation Parameters for different diffraction patterns 25

2.2 Diameter Parameters of SonoVue 30

2.3 Simulation Parameters for bubble response. 31

3.1 Simulation Parameters 47

3.2 Computational Cost 59

4.1 Simulation Parameters 67

4.2 Computational Cost 77

5.1 Simulation parameters for tube phantom simulation. 83

5.2 Post-processing parameters for tube phantom simulations. 83

5.3 Monodispersed microbubble parameters for *in vitro* experiment. 85

5.4 Physical probes parameters for *in vitro* experiment. 85

5.5 Bubble response simulation parameters with different **pulse cycles**. 86

5.6 Bubble response simulation parameters with different **MIs and** f_0 86

5.7 Evaluation results for 2D tube phantom simulation using L12-3v. 90

5.8 Evaluation results for 3D tube phantom simulation using Matrix1024-8MHz. . . 92

List of Figures

1.1 Comparison of Porcine Heart in 2D and 3D SRUS 2

2.1 Functions of the microvasculature. 6

2.2 Comparison of tumor structure in 2D and 3D microscopy. 6

2.3 Comparison of tumor structure in 2D and 3D microscopy. 7

2.4 Imaging activity statistics in the UK. 12

2.5 Overview of a US system pipeline. 15

2.6 Components of the PZT transducer. 17

2.7 Different 1D array probes. 18

2.8 Schematization of a linear array probe. 18

2.9 Evolution of the transducer towards the full 2D array. 19

2.10 Different transmission schemes in ultrasound imaging. 21

2.11 Spatial resolution components. 22

2.12 Different beam patterns. 23

2.13 Fresnel diffraction pattern in the near field at different depth 26

2.14 Simulation of the aperture and Fraunhofer approximation. 27

2.15 Composition of a SonoVue microbubble. 28

2.16 Responses at different levels of MI. 30

2.17 Sonovue bubble response's dependence on the radius. 31

2.18 PI and AM sequences. 33

2.19 Spectrum of PI and AM response. 34

2.20 Conventional and Ultrafast Ultrasound Imaging. 36

2.21 Plane-wave imaging and compounding. 36

3.1 X-ray radiograph and CT images. 44

3.2 Transducer and three imaging schemes. 45

3.3 Ground truth of the cross-tube simulation phantoms. 47

3.4 Top and isometric view of the experiment set-up. 50

3.5 Comparisons of long pitch 1D array probe with the matrix array probe results . 52

3.6 The intensity profile along the axial direction. 53

3.7 (a) Imaging sensitivity and (b) Axial localization errors. 54

3.8 Localization images of the tube phantom. 55

3.9 *In vitro* localization, tracking velocity results. 56

3.10 *In vivo* localization, velocity amplitude, and velocity angle maps. 58

4.1 Transducer and four imaging schemes. 66

4.2 (a) Projection and (b) 3D view of the microvessel flow phantom 67

4.3 Top (a) and isometric (b) view of the experiment set-up. 68

4.4 *Ex vivo* porcine heart experimental setup. 69

4.5 Simulation localization and tracking results using four different methods. 71

4.6 Evaluation results of localization and tracking performance in simulation 72

4.7 *In vitro* localization and tracking results. 73

4.8 *Ex vivo* localization and tracking results. 75

5.1 Size distributions of different microbubbles populations. 82

5.2 Bubble response to different pulse lengths 87

5.3 Bubble response to different pulse cycles and MIs with $f_0 = 1.59$MHz 87

5.4 Bubble response to different pulse cycles and MIs with $f_0 = 3.21$MHz 88

5.5 Single frame B-mode images with pulse cycle = 2 *in simulation* 89

5.6 Localization and tracking results *in simulation* using L12-3v. 90

5.7 Single frame B-mode images with pulse cycle = 8 *in simulation* 91

5.8 Localization and tracking results *in simulation* using Matrix probe. 92

5.9 BMode image using P4-2 *in vitro*, summed 500 frames with mean subtraction . . 93

5.10 PI image using P4-2 *in vitro*, summed 500 frames 93

5.11 AM image using P4-2 *in vitro*, summed 500 frames 94

5.12 BMode image using L12-3v *in vitro*, summed 500 frames with mean subtraction 94

5.13 PI image using L12-3v *in vitro*, summed 500 frames 94

5.14 AM image using L12-3v *in vitro*, summed 500 frames 95

5.15 Localization and tracking results *in vitro* using matrix probe. 95

6.1 A pair of bubbles in two consecutive frames. 101

6.2 3D reconstruction (right) using X-ray projection image (left). 102

6.3 3D reconstructed image using projection Bmode image 103

6.4 Comparisons of the 3D reconstructed results with the ground truth results . . . 103

Chapter 1

Introduction

1.1 Motivation and Objectives

Visualizing the microvasculature can assist with the diagnosis, therapeutic monitoring, and follow-up of disorders that have aberrant blood vessel conditions. Many Back in 2013, early studies demonstrated the ability of Super-Resolution Ultrasound (SRUS) imaging to super resolve microvasculature in depth *in vitro* [1, 2] and *in vivo* [3, 4, 5, 6, 7, 8] by localizing the spatially isolated contrast agents signals. Then researchers applied this imaging technique on different animal models preclinically and pilot studies clinically, including oncology [9, 10, 11, 12], neurology [13, 14, 15, 16] and cardiology [17, 18].

However, one limitation of this technique is the long acquisition time that hinders clinical translation [19]], due to the requirement of the sparsity of contrast agents that results in slow accumulation of localizations to form a final SRUS image. Researchers have tried to use advanced filtering methods [20], sparsity-based algorithms [21] and deep-learning tools without structural priors [22] to improve the separation of contrast agents during the post-processing stage. However, the problem of the filtering method is the ignorance of MB nonlinearity, and the imperfect performance of the filter may overestimate the intensity of larger vessels due to the accumulation effect. The sparsity-based method improves the acquisition time at the cost of the microvessel structural completeness. Besides, the deep learning methods rely on high-

quality training data. As demonstrated in [23], a long short-term memory neural network was used to exploit the spatiotemporal characteristics of microbubbles with higher concentration, providing a higher image reconstruction speed (∼160 ms). However, the risk is that when the vessels twist or when the MB information is sparse in certain vessels, the model will generate artifact vessels that do not exist. Since the model was trained on specific organ data, structural bias will be introduced whenever the vessel distribution in the validation dataset varies. Therefore, how to make these neural network methods more adaptive and generally applicable still needs investigation.

Another limitation is that most research generates 2D images, which are partial visualizations

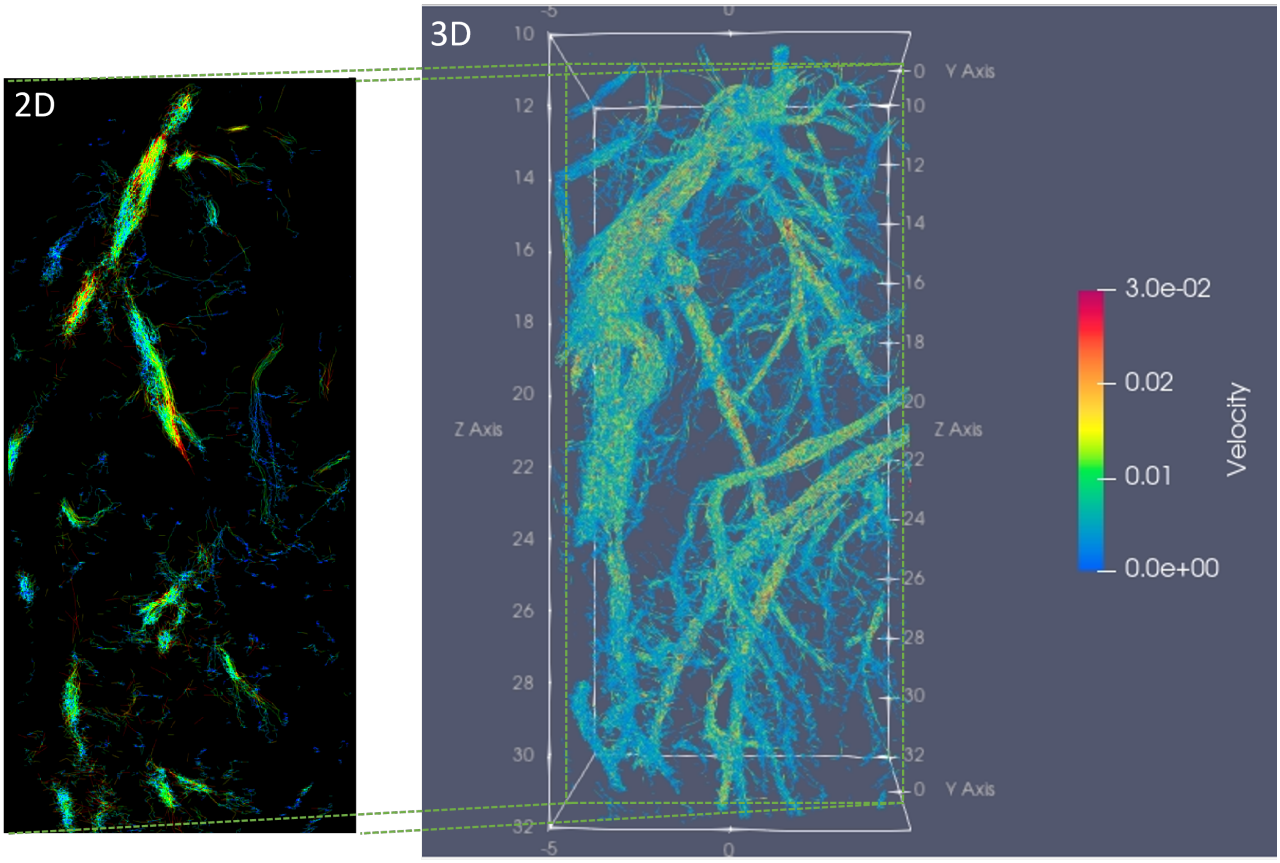


Figure 1.1: Comparison of Porcine Heart in 2D and 3D SRUS

of often complex 3D structures, due to the complexity and high cost of a typical 2D matrix array probe and data acquisition hardware. Fig 1.1 compares the 2D and 3D SRUS images on the same imaging object, where 2D SRUS can only capture segments of the 3D vessels. Although 3D SRUS imaging has brought benefits including larger volume coverage and the ability to track contrast agents in and out-of-plane, the fabrication of customized probes [24]

or matrix array probes [25, 26, 27, 17, 16], the acquisition hardware required and the following computational costs in 3D are expensive.

To address the problem of volumetric coverage, this thesis proposed broad elevation protection SR and multi-aperture projection SR using a 1D array and a 1.75D array, respectively. Results show that the proposed methods can combine the low-cost benefit of 2D SRUS imaging and the broader volume coverage of 3D SRUS imaging. These techniques could have the potential to facilitate the clinical translation of super-resolution ultrasound imaging.

For the other problem, this thesis explores using mono-dispersed microbubbles in super-resolution ultrasound imaging and investigates if it can be used to reduce the acquisition time during the imaging process and if it can improve the SR imaging performance.

1.2 Statement of Originality

We state here that all the research work presented here is my work except where work by others has been properly acknowledged.

1.3 Copyright Declaration

The copyright of this thesis rests with the author. Unless otherwise indicated, its contents are licensed under a Creative Commons Attribution-Non Commercial 4.0 International Licence (CC BY-NC).

Under this licence, you may copy and redistribute the material in any medium or format. You may also create and distribute modified versions of the work. This is on the condition that: you credit the author and do not use it, or any derivative works, for a commercial purpose.

When reusing or sharing this work, ensure you make the licence terms clear to others by naming the licence and linking to the licence text. Where a work has been adapted, you should indicate that the work has been changed and describe those changes.

Please seek permission from the copyright holder for uses of this work that are not included in

this licence or permitted under UK Copyright Law.

Chapter 2

Background Theory

2.1 Microvasculature

Microvasculature plays a critical role via microcirculation from many perspectives, including delivery of nutrients, removal of waste products between the blood and surrounding tissues [28], oxygen distributions [29], as well as cellular communications [30]. Fig 2.1 shows the crucial functions of the microvasculature [31]. Structural alteration in the microvasculature may indicate impaired tissue perfusion, tissue damage, and even cancer.

In detail, new capillaries growing from the existing vascular network, known as the angiogenesis process, will help feed the growth of cancer cells [32], since the proliferation and metastatic spread of cancer cells depends on the adequate supply of oxygen and nutrients and the removal of waste products [33]. Fig 2.2 and Fig 2.3 show the normal architecture and pathological tumor architecture of the brain using a light microscope, respectively. Fig 2.2(a-b) shows the 2D slices of the normal tissue, little vessel segments can be found compared to the enriched 3D vessel network in Fig 2.2(c-d). Tumour histological sections in Fig 2.3(c-d) show substantial aberrant density and proliferative behaviour.

Microcirculation dysfunction is also the key predictor of pathophysiologic conditions such as sepsis and acute heart failure [35]. Besides, diagnosis of diabetes is also assisted by assessing

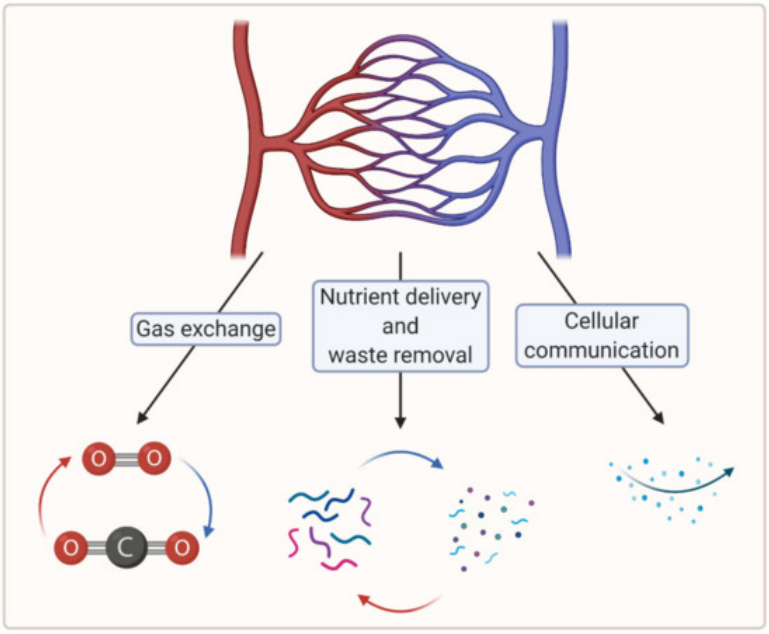


Figure 2.1: Functions of the microvasculature [31].

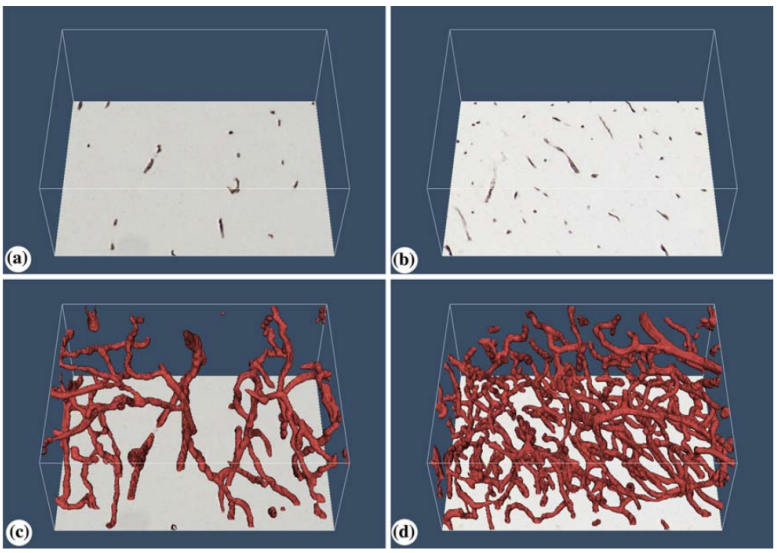


Figure 2.2: The 2D histological sections of normal (a) cerebral white and (b) neocortical grey matter stained for endothelium and corresponding 3D reconstructions of the microvascular architecture (c and d) using a light microscope, volume of box: 494 x 370 x 200 μm, referenced from [34].

the microvascular function, particularly the microvascular function of the retinal, renal, and peripheral nervous systems [36, 37, 38]. For example, increased diameter of retinal venule, and pathological neovascularization that advance to retinal hemorrhage, were associated with incident diabetes and impaired fasting glucose [39, 40]. And persistent reduction in renal perfusion was linked to type-2 diabetes [41]. Diabetic neuropathy is implied by pathological changes like

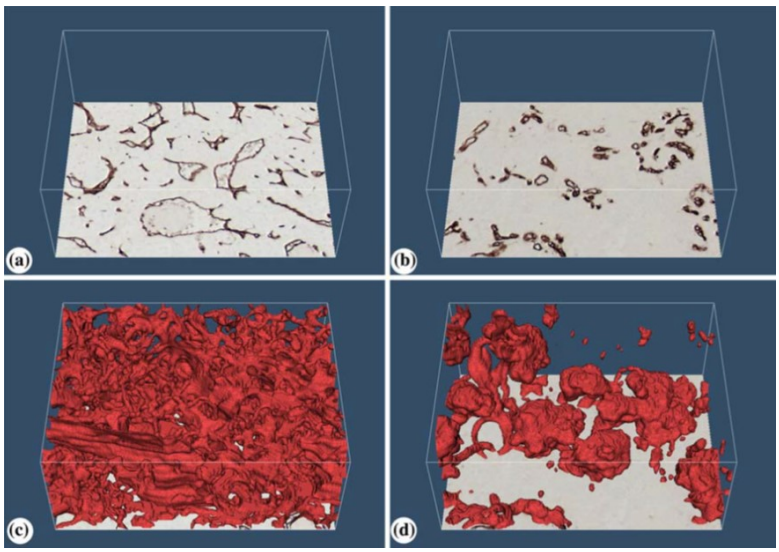


Figure 2.3: The 2D histological sections of (a) hemangioblastoma and (b) glioblastoma multiforme stained for endothelium and corresponding 3D reconstructions of the microvascular architecture (c and d) using a light microscope, volume of box: 494 x 370 x 200 μm, referenced from [34].

the loss of nerve fibers [42] and abnormal neurovascular blood flow that may cause ischemic-neuronal damage [43].

Myocardial imaging also plays a key role in cardiac diagnosis, where ischemic heart disease is the primary cause of heart failure in more than half of patients in North America and Europe [44]. Nevertheless, multiple studies indicate that as the nervous system ages, the microvasculature in certain brain regions becomes rare and the remaining vessels may undergo structural changes leading to a decrease in cerebral blood flow (CBF) [45].

Apart from the density change and perfusion dysfunction, another observation is that vasculature associated with a range of malignancies are irregularly shaped [46], either larger amplitude curves with sharp direction change, with close distances between endpoints, or high-frequency wiggles that produce a high curvature per unit distance (see Fig 2.3(d)) [47]. In addition, tortuosity anomalies can be present in early-stage cancers, extending beyond the margins and affecting the surrounding tissue, which suggests that assessing tortuosity can detect even small malignant tumours [47]. More specifically, retinal vascular tortuosity is considered one of the most crucial signs for detecting diabetes [41, 48]. Evidence also indicates that Alzheimer's disease is a vascular disorder with neurodegenerative consequences, rather than a neurodegenerative disorder with vascular consequences [49]. Vascular changes, including not only decreased

vascular density but also the presence of atrophic and coiling vessels were consistently noted in Alzheimer's disease(AD) [50].

Therefore, visualizing the structure - either density or tortuosity of the microvasculature and measuring the microcirculation condition using advanced imaging technique will help understand the progression of microangiopathy and the critical pathophysiological processes involved, benefiting the diagnosis and treatments for a variety of diseases as mentioned above.

2.2 Microvascular Imaging Techniques

Different imaging modalities are being used for vascular imaging, such as optics, photoacoustic, magnetic resonance imaging (MRI), X-ray, and computed tomography (CT). Many general reviews [51, 52] have illustrated these main technologies and their distinct challenges that currently exist, which are summarised below.

2.2.1 Optics

Optical imaging is the imaging modality that can provide the highest spatial resolution and is mainly used for superficial imaging and subsurface imaging. Fluorescence microscopy techniques such as photoactivated localization microscopy (PALM) [53] has been investigated for intracellular imaging and optical coherence tomography (OCT) [54, 55] has been widely investigated for microvascular imaging.

PALM can overcome the light diffraction limit by localizing isolated fluorophores on a large number of microscope images and achieve a resolution at around 10 nm [53]. However, it is mainly used for live cell imaging. Its ultrasound analog, Super-Resolution Ultrasound (SRUS) or Ultrasound Localization Microscopy (ULM) [56, 57] will be discussed in detail later in this chapter.

In OCT, a short pulse light signal is transmitted through two paths, and then the reflected light traveling from these two paths can avoid interference within a distance of micrometers, being able to be resolved at a level of 1-15 μm [58]. Thereafter, reflectivity profiles and images can be

reconstructed by analyzing the interference patterns. It is specifically useful for morphological tissue imaging with millimeter penetration depth, such as soft tissue of the oral cavity [59], skin [60], and retina [61, 62].

To characterize the blood flow, doppler OCT, also known as optical doppler tomography [63, 64] was later developed by calculating the phase difference between adjacent scans, enabling functional imaging of blood flow in skin [65] and retina [66].

However, this imaging modality is always constrained by the limited imaging depth (1-2 mm) and thus its clinical applications in deeper tissue microvasculature imaging.

2.2.2 Photoacoustic

Photoacoustic (PA) Imaging is a recently developed imaging modality that can be used for microvascular imaging [67, 68]. It combines the benefits of high contrast of optical imaging and the deeper penetration depth of ultrasound imaging.

In PA imaging, laser pulses are used to irradiate tissue and cause the temperature to increase. Then the heat induces thermoelastic expansion of tissue that emits ultrasound waves. These ultrasound signals are received by the ultrasound transducer as a part of the PA imaging system. After that, the PA image can be reconstructed by analyzing the time-of-arrival of the signals as conventional ultrasound image reconstruction.

Chromophores such as hemoglobin and melanin can absorb light more strongly than other chromophores and therefore can be used as PA contrast agents [69]. To further improve the contrast, organic dyes like indocyanine green(ICG) [70] and methylene blue [71] can be used as targeted contrast agents with specific bandwidth clinically. With the help of these contrast agents, PA has been applied to imaging breast [72, 73, 74], skin [75] and retinal [76] morphologically and functionally.

Although having the benefit of higher contrast inherited from optics, this imaging modality is still constrained by the imaging depth and hence its clinical application. Another important biohazard consideration of this relatively novel imaging technique is the non-standardized tissue-specific laser safety limits [77]. The American National Standards Institute (ANSI) de-

fined a gentle limit for the retinal and skin tissue only [78], but currently, there are no clinical FDA-approved PA imaging systems to perform retinal imaging due to safety concerns [79]. However, the present safety restrictions would reduce imaging capability for deeper targets. For example, visualizing the major blood vessels in the liver, where it is challenging to differentiate it from the surrounding tissue during surgery and thus cause liver damage. PA imaging can guide this intervention and reduce the damage, however, the operating level needed exceeds the safety limit [80].

2.2.3 MRI

Magnetic Resonance Imaging (MRI) [81, 82] is one of the most popular non-ionizing medical imaging techniques in clinics. It can offer high spatial resolution with excellent depth penetration.

In MRI, radio frequency pulses are transmitted to cause atomic nuclei such as hydrogen atoms to be realigned to a specific direction. This is called the polarization process, during which RF echoes are emitted and detected by the MRI machine. As hydrogen atoms are abundant in the human body (water and fat), it is very popular to image areas with soft tissue.

To enhance the contrast of MRI images, contrast agents [83, 84] like Gadolinium [85] and Iron oxide [86] were introduced to MRI to improve the characterization of tumor vasculature [87]. Then phase contrast MRI [88] was developed to quantify flow volume and flow rate [89]. To imaging vasculature, Magnetic Resonance angiography (MR angiography) [90] was shown to be able to detect left main coronary artery disease with high sensitivity and specificity [91] and could achieve a resolution of around 1 mm [92].

Functional MRI [93] was recently developed to show cerebral blood flow changes in the brain [94] and is currently being commonly used in neuroimaging for cognitive research [95]. However, even using a high-field MRI device, the resolution is still limited at the sub-millimeter level [96]. Its ultrasound analog, functional Ultrasound Imaging (fUS) [97] will also be introduced in the later part of this chapter.

However, one basic restriction of this imaging technique is the adverse dependency between the

spatial resolution, scanning time and SNR, which can be described as below:

$$SNR \sim \Delta V \times \sqrt{TA} \tag{2.2.1}$$

where SNR means the signal-to-noise (SNR) ratio, ΔV means the voxel size that is inversely proportional to the resolution, TA means the acquisition time. To achieve the desired level of SNR, operators can either reduce the scanning step size or increase the scanning time. Although both are time-consuming, operators typically prefer to increase the scanning time, which is already longer than other imaging modalities. Another hardware issue is that the gradient strength is limited to 300 mT/m on clinical scanners, restricting the minimum slice thickness and sufficient spatial resolution [98].

High-field MRI can partially compensate for the SNR, but may induce undesired heating hazards. The other limitation is the expensive cost as most high-field scanners employ superconducting magnets, which need additional high-power infrastructure and are sensitive to vibrations and adjacent ferromagnetic objects [99]. As the software advances including compressed sensing and deep learning reconstruction, and post-processing methods develop, lower-field machines have regained the interest and have shown to have high performance clinically [100]. However, for visualizing microvasculature, high-field MRI would be ideal, as a study has revealed that even utilizing a 3T equipment, MA angiography still missed many fine perforating arteries [101]. Therefore, MRI is currently unsuitable for microvascular imaging so far due to the limited spatial resolution ($<$ 1mm), the high cost of MRI machines, and ongoing maintenance expenses.

2.2.4 X-ray

X-ray [102] is another main imaging technique used broadly in clinics. In X-ray imaging, generators project the X-ray beam onto the imaging object. As harder, denser structures and soft tissues have different absorption and attenuation coefficients, different amounts of energy will pass through the imaging object and be detected. Then these differences can be used to reconstruct the images with contrast. X-ray projectional radiography [103] and X-ray computed

tomography (X-ray CT) [104] are the two primary X-ray imaging methods.

X-ray Projectional Radiography

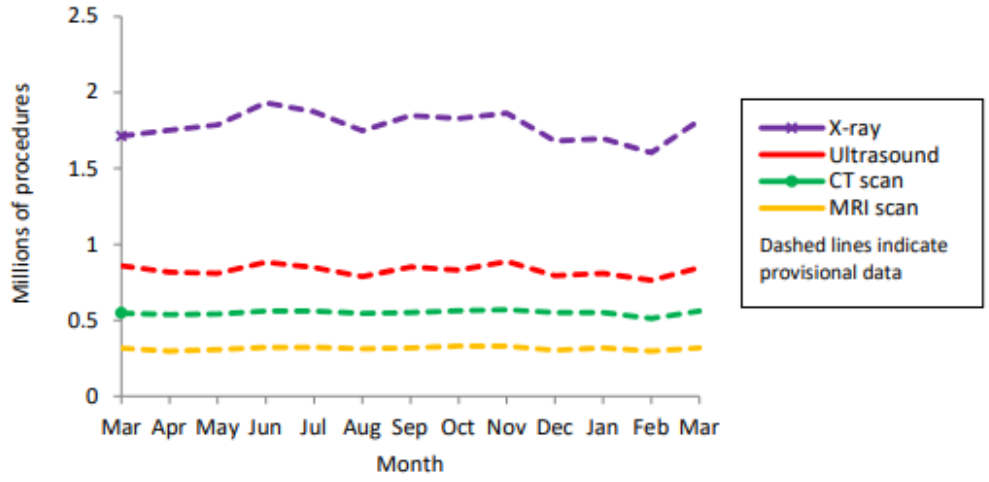


Figure 2.4: Imaging activity happened between March 2021 to March 2022 in England [105].

According to the NHS statisorthopedicsUK [105], X-ray projection radiography remains the most common diagnostic tool, thanks to its low cost and valuable diagnostic information. Fig 2.4 shows the imaging activity that happened between March 2021 to March 2022 in England. X-ray imaging, which specifically refers to X-ray Projection Radiography, is separated from CT scans in statistical analysis and is almost three times more popular than the latter. It is specifically useful for morphological examinations in orthopaedics, dental, lung, and breast diseases. It is also used to visualize blood flow in the aorta [106, 107] and pulmonary [108].

To visualize microvasculature, synchrotron-based X-ray using an advanced nanoparticle contrast agent was able to reveal microvessels with a 20 μmm diameter and extravascular diffusion in the leg tumour [109]. Although promising, the synthetic approaches for these advanced contrasting nanoparticles require further development for large-scale, low-cost manufacturing. Related imaging research should focus more on the direction of clinical implementation [110].

X-ray CT

In the USA [111], X-ray CT examinations have doubled during the past decade thanks to its higher resolution compared to X-ray Projectional Radiography. Multi-slice scan [112], fan-beam scan, or cone-beam scan are used to reduce the effective slice thickness between truncated projections, reducing the blurriness in the reconstructed images. the resolution of this imaging technique can be further improved using advanced reconstruction methods like filtered back-propagation [113]. CT-related vascular imaging techniques are cheaper than MRI and can image deeper than optical imaging.

To enhance the imaging contrast, contrast agents like iodine and barium [114] were also introduced to this imaging modality and enabled the quantification of blood flow [115] and perfusion imaging [116]. With the help of these contrast agents, synchrotron X-ray tomography was able to obtain 3D vascular cortical network with a resolution of several cubic millimetres [117].

One technique for visualizing vasculature using CT, known as CT angiography [118], is the main tool in diagnosing coronary artery disease [119]. However, this imaging technique can only achieve a resolution around 500 μm [120] or 150 μm with ultra-high-resolution machine [121], disabling imaging of the majority of microvasculature that is usually smaller than 200 μm [122].

Micro-computed tomography (micro-CT) is another advanced technique that is demonstrated to visualize a 5 μm wire target [123] and the microvasculature of small animals and can show the details down to the 20 μm voxel limit on rat lung [124]. However, there are still certain distances to be covered when using micro-CT scanning involving soft tissues in vivo or clinically [125]. First, the size of the specimen is limited to a tiny scale in micro-CT. Secondly, in clinical scanners, the imaging object stays stationary while the X-ray source and the detector move around it, whereas in micro-CT, the scanned specimen is mechanically stabilized and rotated. Finally, most micro-CT uses tubes with very small focus spots, which results in a significant amount of scanning time needed. Furthermore, smaller voxels require an increase in the total number of photons, resulting in the energy of the X-rays used in micro-CT imaging being extremely high [126, 127]. At the same time, specimens preserved in formalin solutions and stained by the acidic solution may undergo volume shrinkage during the long imaging process

[128], which may introduce variability and affect the in vivo and clinical application studies. Another shortcoming of this time-consuming imaging procedure is the inadequate temporal resolution, which is still several seconds after technical innovations [129]. This limits its capacity to disclose microvascular flow conditions. Overall, despite the ability to achieve high enough resolution for microvascular visualization, this imaging technique will be confined to morphological specimen imaging at this stage.

Compared to X-ray projectional radiography, CT-scans increase the radiation dose exposure [130], the CT machine is less available, and the examination is more costly. However, the projected view of the 3D anatomical structure provided by X-ray radiography may be less sensitive to certain abnormal situations [131]. As advanced reconstruction and post-processing methods develop, X-ray radiography images are trained to unveil more abnormal features via deep learning networks, which have demonstrated efficiency during the diagnosis of the COVID-19 disease [132]. They are also used to reconstruct 3D images that CT can generate via parametric and statistical models [133] or convolutional neural networks (CNN) [134, 135]. On the contrary, researchers also try to reduce the radiation dose of CT by reducing the number of projections while maintaining the necessary reconstructed image quality during the CT imaging process [136].

But one problem of the X-ray imaging technique is the biodistribution and toxicity of the contrast agents it uses. Studies showed that X-ray radiation may cause chronic kidney disease when using the most common iodine-based contrast agents [137]. And even gold nanoparticles that are claimed to be safer can cause side effects when the dose is not well-controlled [138, 139]. Therefore, an imaging technique that can balance the spatial and temporal reslution for microvasculature imaging, while using more biofriendly contrast agents would be preferred.

2.2.5 Summary

To summarize, optical imaging can scan microvasculature for superficial imaging. Photoacoustic imaging can image deeper, but the successful broader translation requires further safety

investigations. MRI may visualize small vessels with a resolution of ∼100 μm using a high-field machine, which is expensive and less accessible. X-ray imaging techniques can achieve resolutions of several microns, but have the issue of radiation exposure and contrast agent biocompatibility. Leaving a technology gap in the ability to image microvascular with deeper penetration depth to visualize tissue inside, while having the advantages over non-ionizing radiation exposure, accessibility, and good temporal resolution, using biocompatible contrast agents, which can be filled by ultrasound imaging techniques.

2.3 Ultrasound Imaging

Ultrasound is another main imaging technique that the examinations almost doubled in the USA during the past decade thanks to its portable characteristic and advances in relevant signal processing techniques [111].

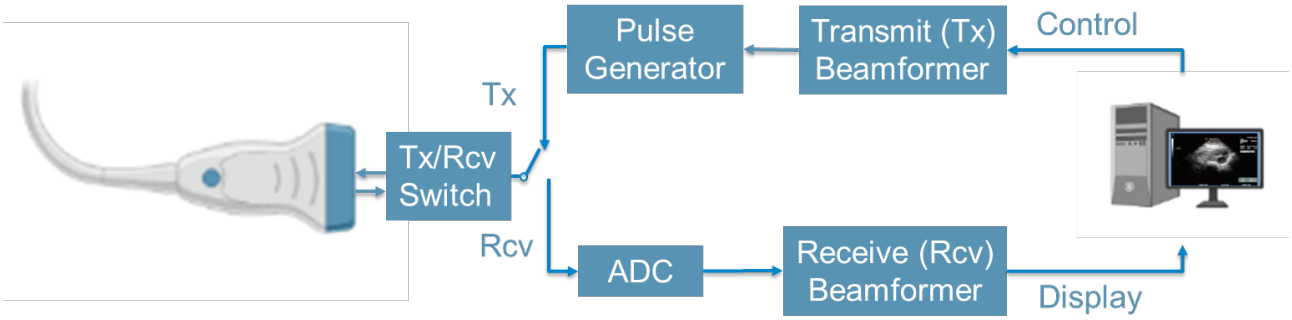


Figure 2.5: Overview of a US system pipeline.

Fig 2.5 shows an overview of a US system pipeline. In transmission, the Transmit beamformer is used to control the electronic focus for each element. Once the delay is defined, the pulse generator transmits excitation signals with a specific frequency, number of pulse cycles, pulse repetition frequency (PRF) and amplitude (voltage). Then the electrical pulse is translated into mechanical stress by the PZT element, which is called the piezoelectric (PZT) effect.
Once the transmission is done, the synchronized Tx/Rcv switch will switch to receive mode until the current pulse repetition period is finished. During this process, the PZT element translates the mechanical echoes emitted from the imaging medium into electrical signals. Then analog-

to-digital converter converts the electricity into digital signals. Then the receive beamformer aligns the signals with appropriate time delays and summed together, reconstructing the ultrasound images. This process is usually implemented on application-specific integrated circuits (ASICs) or field-programmable gate arrays (FPGA) [140].

The following part focuses on the most relevant basics for this thesis, including the mechanisms of the transducer, contrast agents and contrast-enhanced imaging techniques, and most importantly, Super-Resolution Ultrasound.

2.3.1 Transducer

There are different materials can be used to fabricate transducers. The most common materials are the ones having the piezoelectric effect like crystals [141], ceramics [142, 143], polymers [144], composite [145] and most commonly lead zirconate titanate (PZT) [146]. They can convert mechanical energy into electrical energy and vice versa. Another recently developed technology, known as capacitive micromachined ultrasonic transducer (CMUT) [147, 148] uses material like silicon, and translates energy by applying voltages to induce capacitance changes and thus membrane vibrations.

By comparison, the latter material is less sensitive, has a broader bandwidth, and could achieve higher frequency thus improving the imaging resolution [149]. Besides, using CMUT material makes it easier to fabricate 2D arrays with individual electrical connections and the ability to integrate with electronics [147]. As a combination of the higher sensitivity of PZT and easier electronic integration of CMUT, the piezoelectric micromachined ultrasonic transducer (PMUT) has recently developed [150]. However, PMUT develops slower in practice due to challenges such as the manufacturing difficulty of high-frequency thin films, and the fabrication is carried out on special equipment with significant set-up costs [151], while the PZT type of transducer still dominates the market thanks to its manufacturing maturity. For the rest of the thesis, I will focus on PZT transducers, although the imaging methods described in this thesis can be applied to other materials of transducers too.

Transducer Components

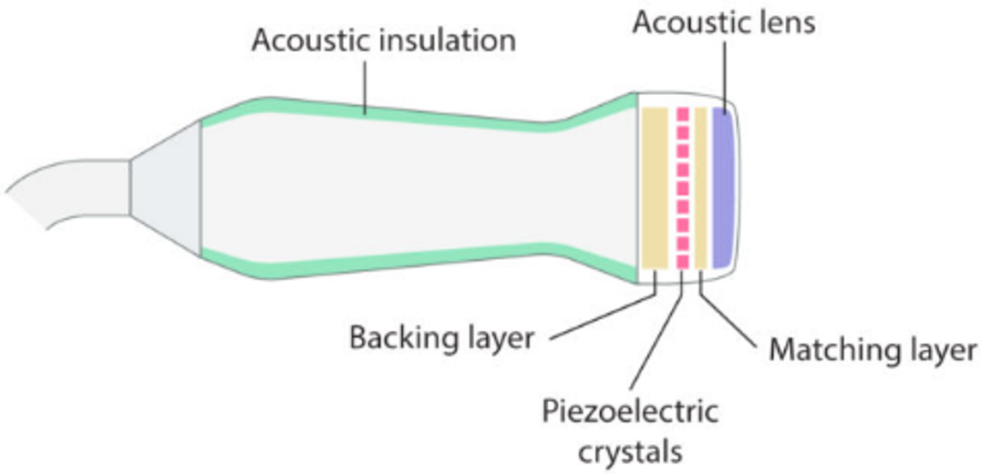


Figure 2.6: Components of the PZT ultrasound transducer.

As shown in Fig 2.6, transducers are composed of passive layers, a PZT layer, and a backing layer. The passive layers include the acoustic lens and the matching layer. The acoustic lens works as a protective layer and also enables focusing along the elevational direction to thin the slice and improve the elevational resolution. The matching layer is used to improve the acoustic impedance mismatch, enabling efficient transmission between the PZT and the imaging medium, and reducing the reflections at the interface.

The PZT layer is where the energy translation happens. The number and arrangement of active PZT elements can create different types of transducers [152, 153].

The backing layer is designed to isolate the PZT element and the casing of the transducer to reduce the reflections between them, thus shortening the pulse length and improving the axial resolution. However, this also causes a broad bandwidth problem when processing the data in the frequency domain.

1D Transducer Arrays

There are three basic types of 1D array transducers, linear array, curved (convex) array, and phased array probe as shown in Fig 2.7. The linear array has a flat front alignment and can provide a rectangular format image. Whereas a convex curved array, with a small footprint,

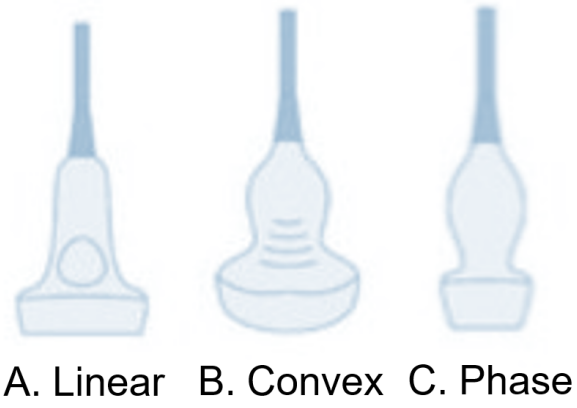


Figure 2.7: Different 1D array probes [154].

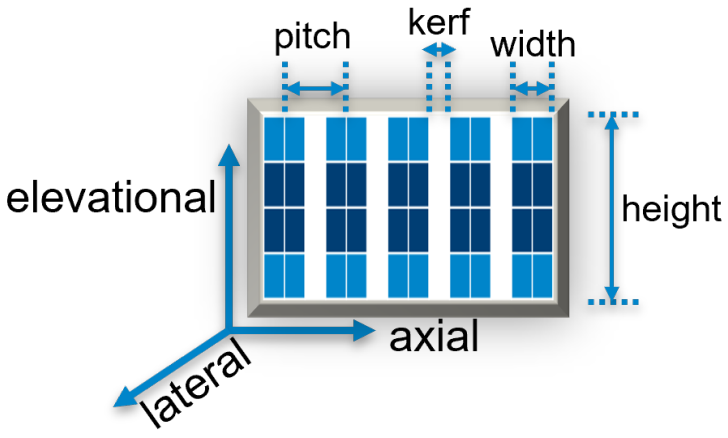


Figure 2.8: Schematization of a linear array probe.

can generate a sector imaging area with a broader imaging field at a deeper imaging depth, therefore, it is popular for abdominal imaging. A phased array has the smallest footprint and thus is popular for cardiac imaging.

Fig 2.8 shows the schematization of a linear array, referenced from [154]. If the element width is smaller than the wavelength, strong side lobes would appear. Similarly, if the element pitch exceeds wavelength/2, grating lobes would appear. Both phenomena would degrade the imaging performance and pose challenges in high-frequency probe fabrication whose wavelength is smaller.

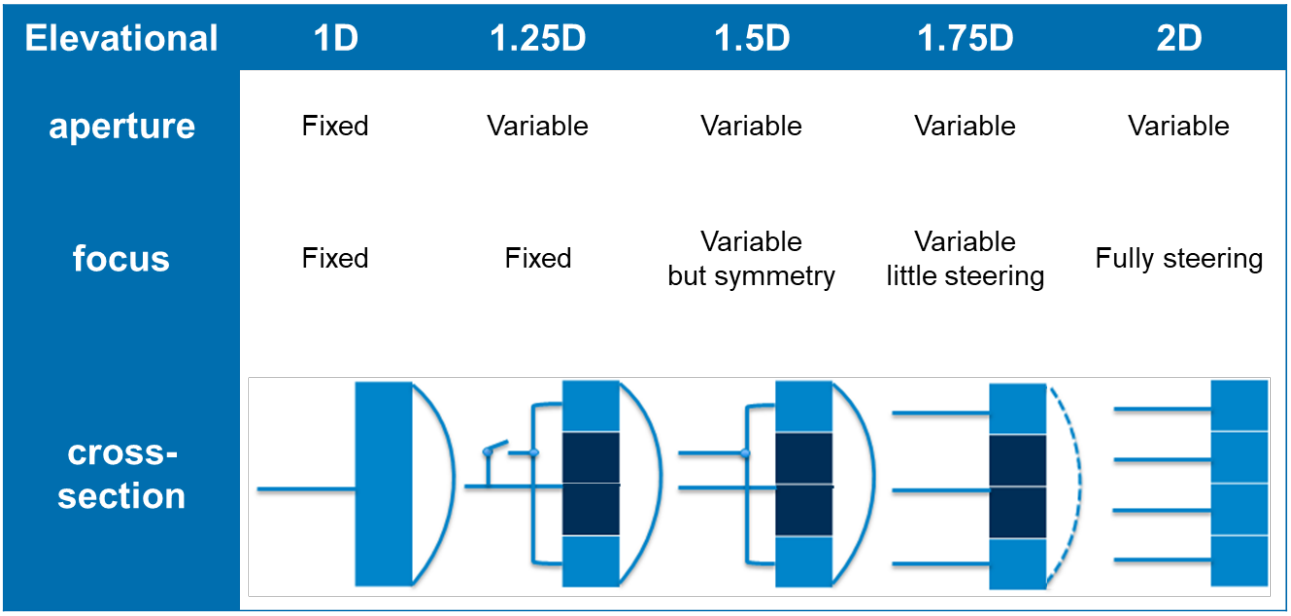


Figure 2.9: Evolution of the transducer towards the full 2D array.

1D+ Transducer Arrays Configurations

Fig 2.9 shows the generations in the evolution of the transducer towards the full 2D matrix array for 3D ultrasound imaging. The process primarily focuses on the addition of elements along the elevational direction to provide the flexibility to steer the beam along this direction. In detail, the 1.25D array transducer provides a switchable, discrete aperture with a fixed elevational focus. The outer row elements are electrically connected in parallel, and data acquisition can be switched between center-row and the center rows using a multiplexor, with the center row and outer row sharing the same channel and pin connections. A 1.5D array transducer [155] requires more channels and connections than a 1.25D array, providing a dynamic aperture with little and symmetrical flexibility in elevational focusing. Both of them have a central row of elements that have double the height of the side row elements to ensure the electrical impedance and acoustic sensitivities between the outer row and centre-row areas are equal [156, 153]. The presence of a physical lens layer also improves elevational resolution and acoustic radiation force impulse (ARFI) [157], helping them gain popularity in the high intensity focused ultrasound (HIFU) treatment for prostate cancer [158, 159].

In a 1.75D array, each row of elements has independent channels and connections, enabling asymmetric focusing. The physical lens layer can be absent in favor of fully electronic beam-

forming [160]. When the rows number is comparable to the lateral elements numbers, a 1.75D array probe without a physical lens layer would become a 2D array probe. 2D array probe inevitably introduces fabrication challenges associated with connecting thousands of elements individually with independent cables, which could also increase the cross-talk levels. Furthermore, as the distinct element size decreases, the impedance mismatch between the element and the cable worsens rapidly, thus decreasing the signal-to-noise ratio [161].

Other Transducer Array Configurations

Apart from the aforementioned standard transducers, some customized transducers were developed to achieve a balance between the channel numbers and imaging performance, especially in 3D US imaging. 2D sparse array with random [161], spiral [162] layouts have been investigated to optimize the configuration. Row-column addressed (RCA) array has also been investigated in 3D US imaging with almost an order fewer elements [163]. A hemispherical array has also been demonstrated for non-invasive ultrasound transcranial therapy in 3D [164, 165].

2.3.2 Transmission and Reception

Fig 2.10 shows the different transmission schemes in ultrasound imaging including (a) plane, (b) focused, and (c) diverging wave transmission. By adjusting the time delay of each element, a focal point can be set at $+\infty$, at a certain depth in front, or virtually on the back, then plane wave, focus wave, and diverging wave can be transmitted, respectively. In conventional ultrasound imaging, a subset of elements is sequentially used to focus on a certain depth to sweep across the imaging region. Whereas in plane wave transmission, the whole aperture of elements is used to insonate the whole imaging region, offering a higher frame rate, but at the cost of contrast-to-noise ratio. Whereas diverging wave transmission is preferred when a larger imaging area is desired, such as abdomen imaging, although the lateral resolution degrades significantly at deeper depth. To characterize microvessel flow, a high frame rate is desired to calculate the slow flow rate which can be as low as several millimeters per second [166, 167].

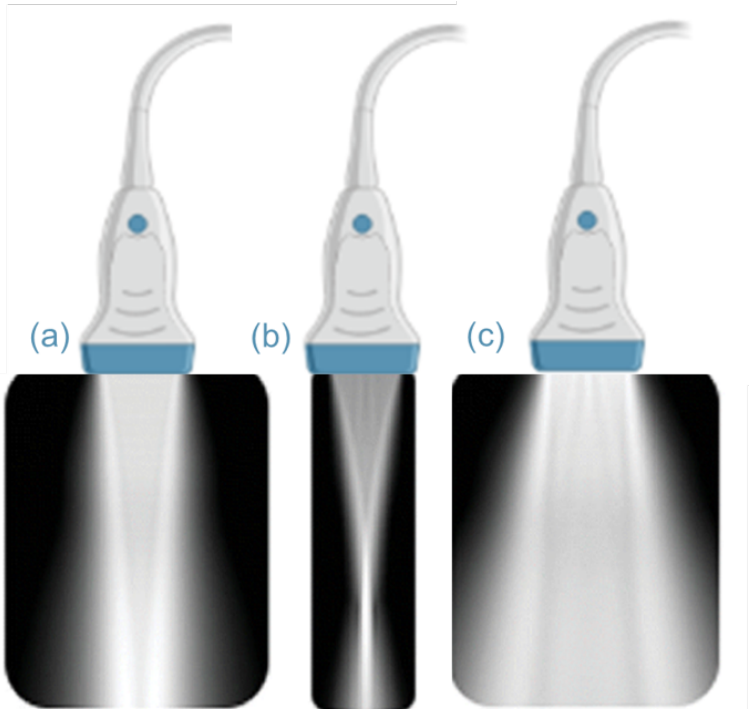


Figure 2.10: Different transmission schemes in ultrasound imaging.

Therefore, experiments included in this thesis will consistently use plane wave transmission. On receive, echoes coming from the same scattering source arrive at each element at different times. According to the arrival time, echoes to each element can be aligned and coherently summed. Repeating this operation over the whole imaging region generates the image consequently. Besides, in both transmission and reception, the amplitudes of the signals associated with the active elements can be adjusted to reduce the side lobe levels, which is known as apodization operation [168].

2.3.3 System Descriptions

The resolution of an imaging system describes its ability to resolve two points separated by a certain distance, within which they could not be separated. The highest resolution theoretically achievable by a standard transducer is the wave diffraction limit.

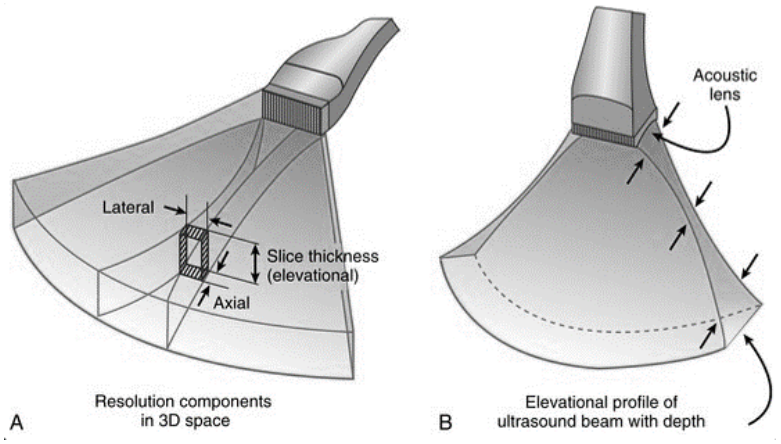


Figure 2.11: Spatial resolution components, axial, lateral and elevational resolution in 3D US imaging, referenced from [169].

Axial Resolution

Axial describes the depth direction in ultrasound imaging, resolution along this direction is defined as:

$$axial\ resolution = \frac{SPL}{2} = \frac{N_c\lambda}{2} \tag{2.3.1}$$

where SPL means the spatial pulse length, N_c means the number of cycles of the pulse, and λ means the wavelength of the pulse, which is determined by the transmission frequency. Therefore, higher axial resolution can be achieved by either increasing frequency, at a cost of higher attenuation and thus less penetration depth [170] or reducing the pulse cycles.

Lateral Resolution

Lateral resolution describes the resolution in the horizontal direction that is parallel to the alignment direction of the element array. It is determined by the beam width at the focal depth, which varies according to the geometry and the transmission frequency [171].

$$lateral\ resolution = -6dB\ beam\ diameter\ (BD) = 1.02\ \frac{Fc}{fD} \tag{2.3.2}$$

where F means the focal depth, c means the sound velocity, f means the operating frequency, and D means the active aperture diameter. The more elements used for a focus, the larger the

aperture, and the better lateral resolution can be achieved at this depth.

Elevational Resolution

The elevational resolution describes the thickness of the imaging plane, its definition is similar to the lateral resolution except that D is the element height. It also depends on the existence of an acoustic lens or not.

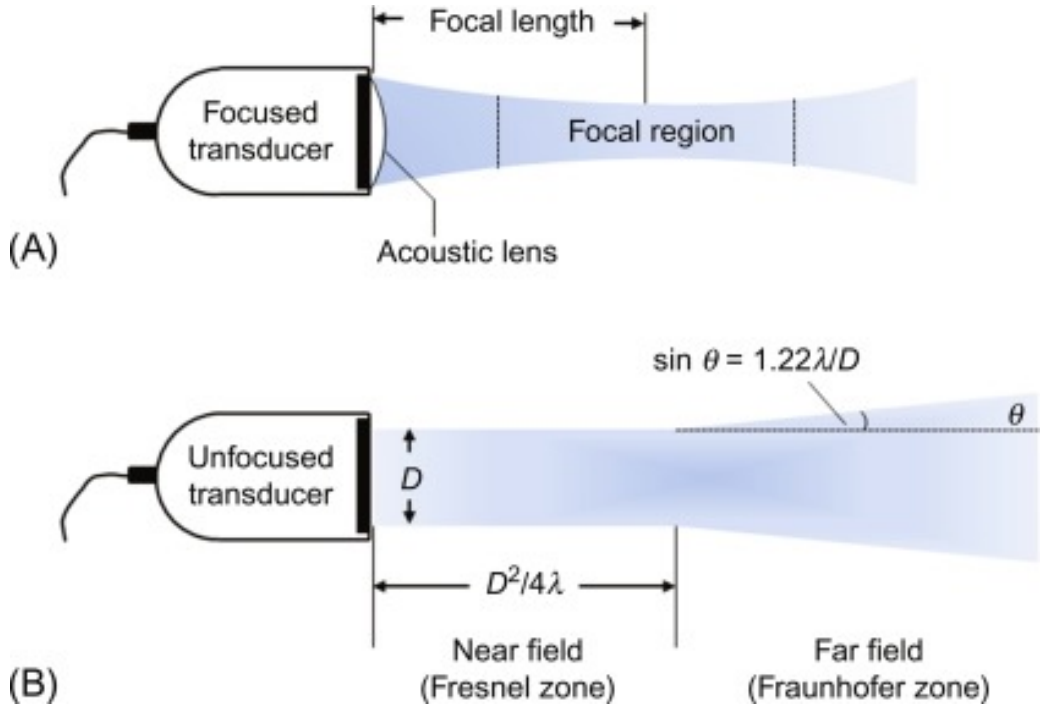


Figure 2.12: Different beam patterns with an (a) focused and (b) unfocused front face transducer, referenced from [172].

As shown in Fig 2.12(a), a fixed focus can be generated using an acoustic lens in front of the elements, increasing the energy focused around the focal point, producing a longer focal length and thus improving the imaging SNR within this area. Without an acoustic lens, an unfocused transducer generates two distinct wave field regions, the near field (Fresnel zone) and the far field (Fraunhofer zone). The complex constructive and destructive patterns of the wave field near the transducer make the end of the near field the natural focus of the unfocused transducer, where the highest energy among the whole wavefield occurs here [172]. The length of the near field is defined as:

$$near\ field\ length = \frac{D^2}{4\lambda} \tag{2.3.3}$$

where D indicates the diameter of the transducer aperture, and λ indicates the wavelength of the pulse. Whereas in the far field, the wave field diverges gradually and the beam diameter is no longer a constant, which introduces another descriptor, divergence angle, that is defined as:

$$divergence\ angle\ = \frac{70\lambda}{D} \tag{2.3.4}$$

which indicates that with a higher operating frequency, the divergence level decreases, enabling better imaging quality in this region. Due to the complex interference patterns near the transducer and the divergence nature of the wave field in the far field, the elevational resolution can become really poor in these regions, especially considering the volume averaging effect of the acoustic signals within the imaging volume [173].

For a focused array probe, an acoustic lens can help reduce the side lobes along the elevational direction, it also changes the near field length as desired. However, it produces a larger divergence angle in the far field compared to an unfocused transducer [174], causing more inhomogeneity along the elevational resolution and thus more inconsistency of the imaging quality along depths.

Temporal Resolution

Temporal resolution is described by Frame Rate (FR), which means the number of images acquired per second with a unit of Hertz (Hz). It represents the ability of the US imaging system to distinguish movements that occur between contiguous frames. It can be calculated as

$$frame\ rate\ = \frac{c}{2DN} = \frac{PRF}{N} \tag{2.3.5}$$

where c means the sound velocity, D means the imaging depth and N means the number of transmission/reception pairs per frame.

Temporal resolution can be improved by decreasing the imaging depth and reducing the number of transmission/reception pairs. It is proportional to PRF by a factor of N.

Point Spread Function (PSF)

The point spread function describes the response of the imaging system to a point target. It describes the blurring degree of the imaging system to a point scatterer in the final image. Due to this spreading of a point target, two scatters that stay within the diffraction limit cannot be discriminated. Assuming the imaging system is linear and the point spread function is shift-invariant, then the image I of a point scatterer can be characterized as the convolution of the point source, modeled by a Dirac Delta function δ, the PSF modeled as H, which can be decomposed into three corresponding components, axial H_z, lateral H_x, elevational H_y, respectively. This can be described by the formula below:

$$I = H_x H_y H_z \otimes \delta \tag{2.3.6}$$

For a linear system, H_z can be modeled as the linear amplification of the excitation signal $p(t)$ by the scatter with an amplitude coefficient of C.

$$H_z = Cp(t) = Csin(2\pi f_0 t) \tag{2.3.7}$$

As H_y would be the same as H_x for a matrix array probe with square elements, only H_x is discussed as an example.

Table 2.1: Simulation Parameters for different diffraction patterns

f_0 /Hz	f_s /Hz	λ /m	W /m	S /m	N (Fraunhofer)	N (Fresnel)
7.7e6	100e6	200e-6	200e-6	300e-6	3	2

In the near field, according to Fresnel approximation, for a slit between two elements, H_x, can be modelled as [175]

$$H_x = E(x,z) = \int_{(W-S)/2}^{(S-W)/2} e^{ik/2z(x-x')^2} \tag{2.3.8}$$

with $S-W$ as the size of the element kerf (slit), and E as the wave's amplitude at a distance z to the aperture. Fig 2.13 shows the Fresnel diffraction pattern along the lateral direction at different depth in the near field $z = 0.005, 0.05, 0.5\lambda$, with the simulation parameters in Table

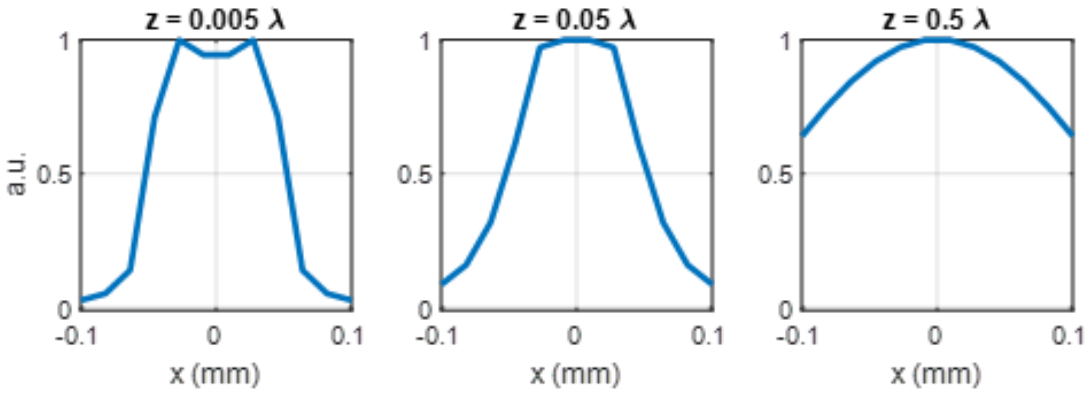


Figure 2.13: Fresnel diffraction pattern in the near field at different depth z, λ indicates wavelength, x means the lateral direction.

2.1. The diffraction pattern varies significantly as depth changes in the near field. Similarly, in the elevational direction, as the PSF of a 2D imaging system is not simply a slice of the 3D PSF, but an average of slices within the elevational beam width, the PSF also varies along this direction at different imaging depths in 2D US imaging, especially in the near field. Therefore, it is always preferred to image in the far field for more uniformity of the PSF.

In the far field, according to the Fraunhofer approximation, H_x can be approximated by the Fourier transform of the aperture function $AP(x)$ [176] that can be defined as :

$$\begin{aligned} AP(x) &= \sum_{n=0}^{N-1} rect\left[\frac{x - nS}{W}\right] \\ &= rect(\frac{x}{W}) \otimes \sum_{n=0}^{N-1} \delta(x - nS) \end{aligned} \tag{2.3.9}$$

$$H_x = \hat{f}[AP(x)] = \hat{f}[rect(\frac{x}{W})]\hat{f}[\sum_{n=0}^{N-1} \delta(x - nS)] \tag{2.3.10}$$

with W as the element width, S as element pitch, N as element number, and $rect(x/W)$ as the rectangular element function defined as

$$rect(x/W) = \begin{cases} 0, & |x| > W/2 \\ 1/2, & |x| = W/2 \\ 1, & |x| < W/2 \end{cases} \tag{2.3.11}$$

Fig 2.14 shows the (a) time domain signals and (b) their Fourier transforms in the frequency

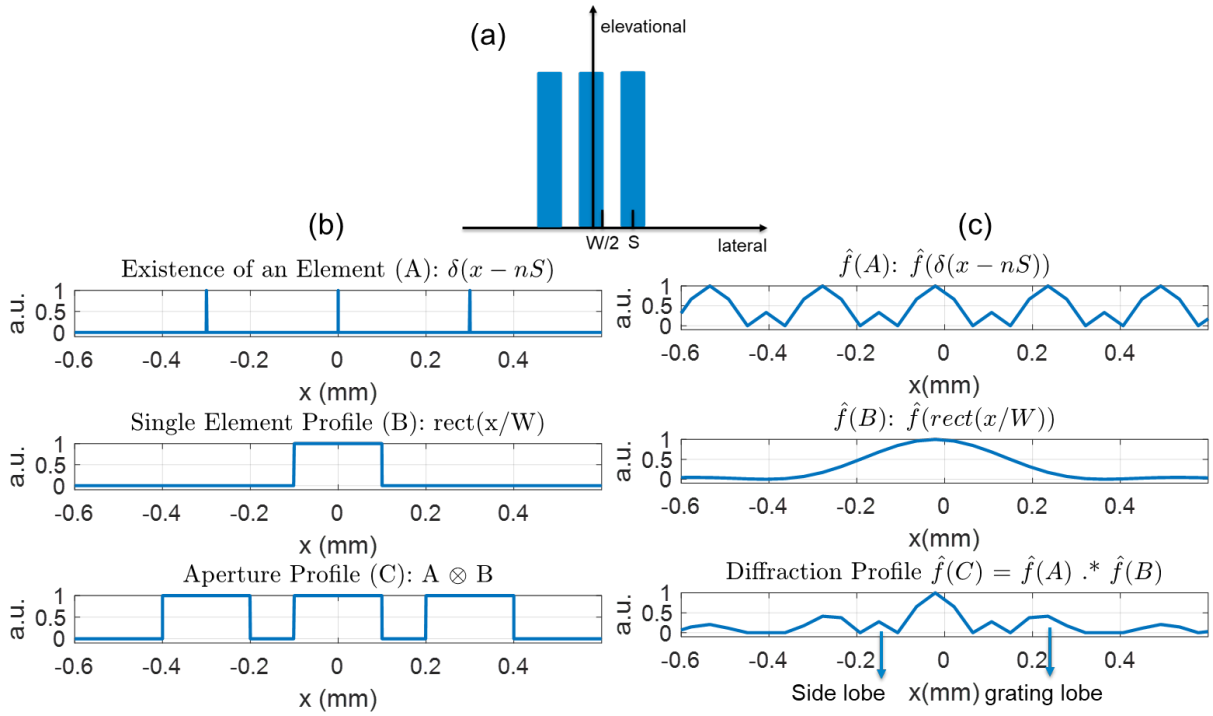


Figure 2.14: (a)The cross-section of the transducer aperture that contains 3 elements, w means element width, s means element pitch. (b) aperture profile and (c) their diffraction profile under Fraunhofer approximation in the far field, simulated with parameters in Table 2.1.

domain with simulation parameters in Table 2.1. Local maxima of the *sinc*() function introduce side lobes and the periodic appearance of excitation pulses causes the generation of grating lobes.

2.4 Contrast-Enhanced Ultrafast Imaging

2.4.1 Contrast Agent

The introduction of contrast agents, most commonly, microbubbles to US imaging has enabled the quantization of blood flow of the vasculature [177, 178]. A microbubble typically consists of a gas core stabilized by a biocompatible shell-like protein, lipid, or polymer [179]. Fig 2.15 shows the composition of a SonoVue microbubble that encapsulates the sulphur hexafluoride

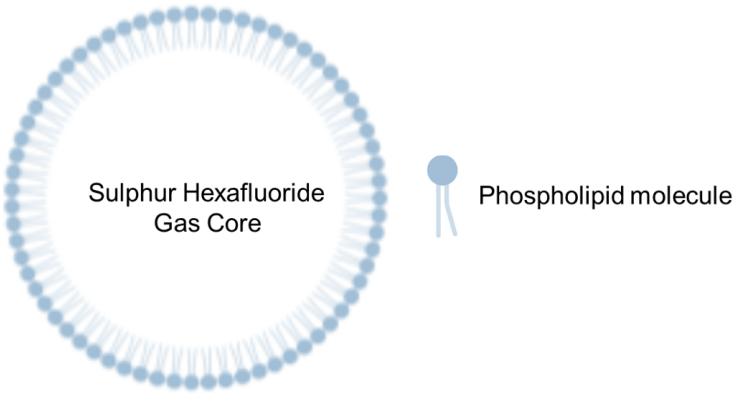


Figure 2.15: Composition of a SonoVue microbubble that encapsulates the sulphur hexafluoride (SF_6) gas core with a phospholipid monolayer.

(SF_6) gas core with a phospholipid monolayer shell [180]. Once the bubble is excited by the ultrasound pulse, it expands and compresses, emitting ultrasound echoes that are much stronger than that of similar-sized blood cells and the surrounding tissue, thus enhancing the contrast. Several microbubbles have been commercialized using different components like Sonovue (Bracco Imaging S.p.A.), Sonozoid (Amersham Health Inc.), Definity (Bristol-Myers Squibb) and Optison (Amersham Health Inc.), etc [181].

To better understand the asymmetric oscillating behavior of microbubbles, many gas models incorporating the effect of a lipid monolayer coat were proposed and one of them is modelled as follows [182]:

$$\rho_l \left(R\ddot{R} + \frac{3}{2}\dot{R}^2 \right) = \left[P_0 + \frac{2\sigma(R_0)}{R_0} \right] \left(\frac{R}{R_0} \right)^{-3\kappa} (1 - \frac{3\kappa}{c}\dot{R}) - P_0 - \frac{2\sigma(R)}{R} - \frac{4\mu\dot{R}}{R} - \frac{4\kappa_s\dot{R}}{R^2} - P_{ac}(t) \tag{2.4.1}$$

with ρ_l as the density of surrounding liquid, R as the bubble radius, R_0 as the equilibrium radius of the bubble, $\sigma(R)$ as the effective surface tension, μ as the surrounding liquid viscosity, κ as the polytropic gas exponent, κ_s as the surface viscosity of the monolayer, $P_{ac}(t)$ as the acoustic pressure, P_0 as the ambient pressure, $\sigma(R)$ can be expressed as:

$$\sigma(R) = \begin{cases} 0 & if\ R \leq R_{buckling} \\ \chi \left(\frac{R^2}{R_{buckling}^2} - 1 \right) & if\ R_{buckling} \leq R \leq R_{break-up} \\ \sigma_{water} & if\ ruptured\ and\ R \geq R_{ruptured} \end{cases} \tag{2.4.2}$$

with χ indicates the elastic compression modulus of the monolayer.

Solving the ODE above generates the bubble radii along time and its first derivative $\dot{R}$ and second derivative $\ddot{R}$, thus the pressure at a distance d from the bubble can be calculated as [183, 184]:

$$P = \frac{\rho_l}{d}(R^2\ddot{R} + 2R\dot{R}^2) - (\frac{R}{d})^4(\frac{\rho_l \dot{R}^2}{2}) \tag{2.4.3}$$

With low acoustic excitation powers, microbubbles are more likely to undergo symmetrical oscillations, emitting linear responses that have the same frequency component as the excitation pulse. As the acoustic power increases, asymmetrical oscillations happen more frequently. This is because the gas core inside resists compression more than expansion, causing the microbubble to expand with a larger phase than that of the compression [185]. As a result, non-linear signals that have many frequency components are emitted, including multiples of the excitation pulse frequency, which are known as subharmonics and harmonics. If the acoustic power keeps increasing, microbubbles will rupture and dissolve.

Another ultrasound metric, Mechanical index (MI), was also introduced to indicate microbubbles' resistance to the excitation power and the potential cavitation effects that microbubbles may cause in the human body, which is defined as [186]:

$$MI = \frac{P_N}{\sqrt{f_c}} \tag{2.4.4}$$

where P_N is the peak negative acoustic pressure in a unit of MPa, and fc is the centre frequency of the transmitted pulse in a unit of MHz. The current FDA-approved maximum MI in diagnostic imaging is 1.9 [187].

Fig 2.16 shows the plot of the excitation signal and its linear response at a lower mechanical index (MI) and non-linear response at a higher MI. It shows that the spectrum of the linear response and the excitation pulse almost overlapped. Whereas that of the non-linear response spreads over the whole spectrum and has multi-peaks around the harmonic frequencies. Responses were generated using an ultrasound simulator BUFF [188] that incorporates

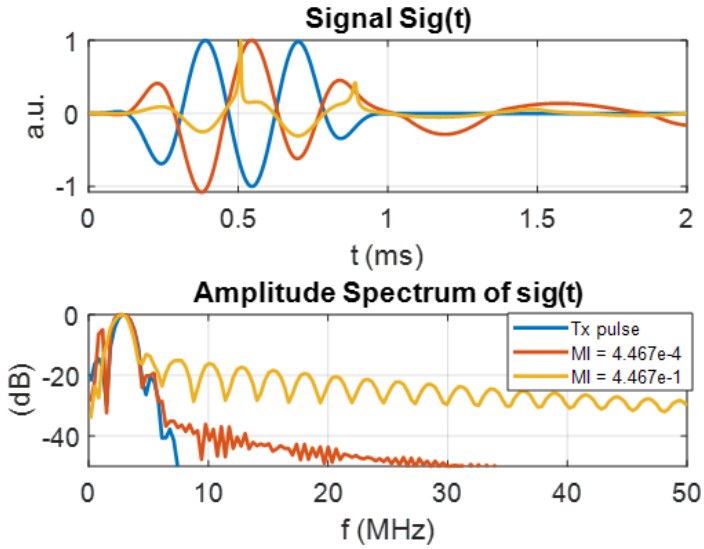


Figure 2.16: Excitation signal and its responses at different levels of MI. The Y-axis in both figures are normalized.

the above-described microbubble model with an ultrasound impulse response simulator Field II [189].

Monodispersed MB

Table 2.2: Diameter Parameters of SonoVue

Products	Diameter (μm)	Conc. T. ($10^8 MB/ml$)	MB $>$ 10 μm ($10^8 MB/ml$)
Sonovue	1.92 $\pm$ 0.09	3.4 $\pm$ 0.5	0.022 $\pm$ 0.006

As microbubbles' response depends on their radius, the effect of the size distributions on the imaging performance has caused broad interest. Their size ranges from 1 to 10 μm. Table 2.2 shows the size distribution characteristics of SonoVue, referenced from [181], where Conc. T. indicates total concentration.

Compared to polydispersed MB that is used clinically, monodispersed MB has a narrower bubble size distribution and a narrower spectrum around its resonant frequency [190], and higher correlated responses [191] that may help improve the post-processing filtering performance. Besides, under non-linear oscillations, it is reported to have up to two orders of magnitude more in sensitivity per microbubble and even more for harmonics [192], which has also been verified *in vivo* [193]. Furthermore, it is also demonstrated that with the same concentration, monodis-

persed microbubbles with larger diameters can increase the SR imaging sensitivity *in vivo* [194]. The investigation of monodisperse microbubbles' effect on SR imaging will be discussed further in the fifth chapter.

Table 2.3: Simulation Parameters for bubble response.

f_0 / MHz	bandwidth / MHz	Pulse Cycle	MI	$R_1/\mu m$	$R_2/\mu m$
1.59	5.00	2.00	0.055	2.95	1.75

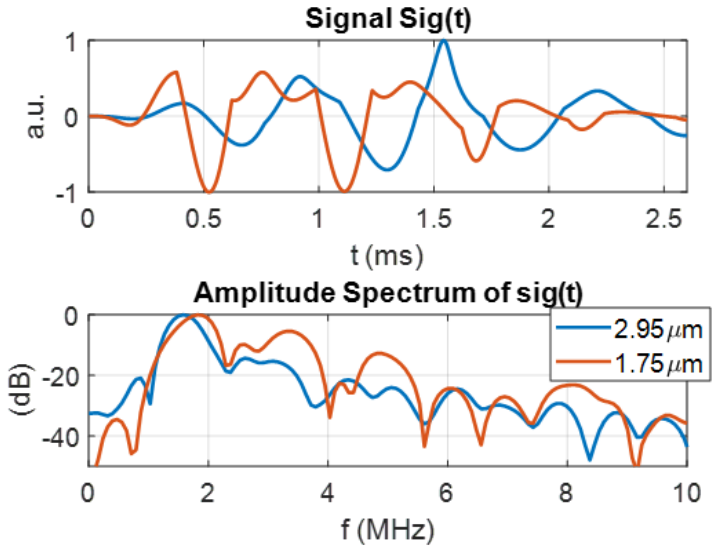


Figure 2.17: Sonovue bubble response's dependence on the radius.

Fig 2.17 shows the dependence of a Sonovue bubble response on its radius, with the simulation parameters in Table 2.3. When transmitting a two-cycle excitation pulse at the theoretical resonant frequency of bubble R_1 (2.95μm), bubble R_2 (1.75μm) has a more non-linear response than the resonant bubble R_1, corresponding to the stronger harmonics components shown in the spectrum.

2.4.2 Contrast Enhanced Ultrasound Imaging

Benefiting from the sensitivity and response characteristics of microbubbles, contrast-enhanced ultrasound imaging developed very fast in the past decades. It has been widely applied clinically in hepatic imaging to detect focal liver lesions [195], cardiac imaging to assess the systolic

function of the left ventricle [196] and perfusion function of the myocardium [122]. To utilize the non-linear response of contrast agents and help separate signals from tissue and contrast agents, harmonic imaging and multi-pulse imaging techniques like pulse inversion (PI) [197, 198], amplitude modulation (AM) [199], the combination of them, pulse inversion and amplitude modulation (PIAM) [200], and coded pulses [201, 202, 203, 204] are developed and employed on clinical machines.

Harmonic Imaging

In ultrasound imaging, harmonics are generated from tissue [205] and contrast agents [206]. As the transmitted pulse propagates, the frequency component changes, and harmonics appear due to nonlinear propagation of the transmitted pulse. Although its instant energy is smaller than the fundamental component, harmonic energy accumulates as it propagates [207, 208]. On the reception, the back-scattered harmonic component can be bandpass filtered and used to reconstruct images with higher resolution.

Under low mechanical index transmission, tissue is more likely to undergo linear response and thus generate little harmonics component. Whereas microbubble contrast agents can generate strong harmonic echo signals at acoustic pressure as low as tens of KPa [209], which offers an opportunity to detect contrast agent-specific signals. At high mechanical index transmission, tissue generates stronger harmonic components. Thus, tissue harmonic imaging is used to improve the imaging quality of tissue, especially at deeper depths when a lower transmit frequency is transmitted to attain adequate depth penetration.

Harmonic imaging also brings the benefit of autofocusing as harmonics are more likely to be generated at the centre of the beam where the pressure is the highest [207]. However, harmonic imaging is subject to the higher attenuation of harmonics and the limited bandwidth of the transducer. Besides, due to practical material constraints, transmitted pulses are usually not narrowband enough so that the transmit pulse also contains some harmonic energy, contaminating the harmonic signals that should only come from the imaging medium ideally. To alleviate this problem, multi-pulse sequences like pulse inversion can be utilized to extract the harmonic signals even when there is an overlap between the transmitted frequency and the

harmonic frequency of the echoes.

Multi-Pulse Sequence

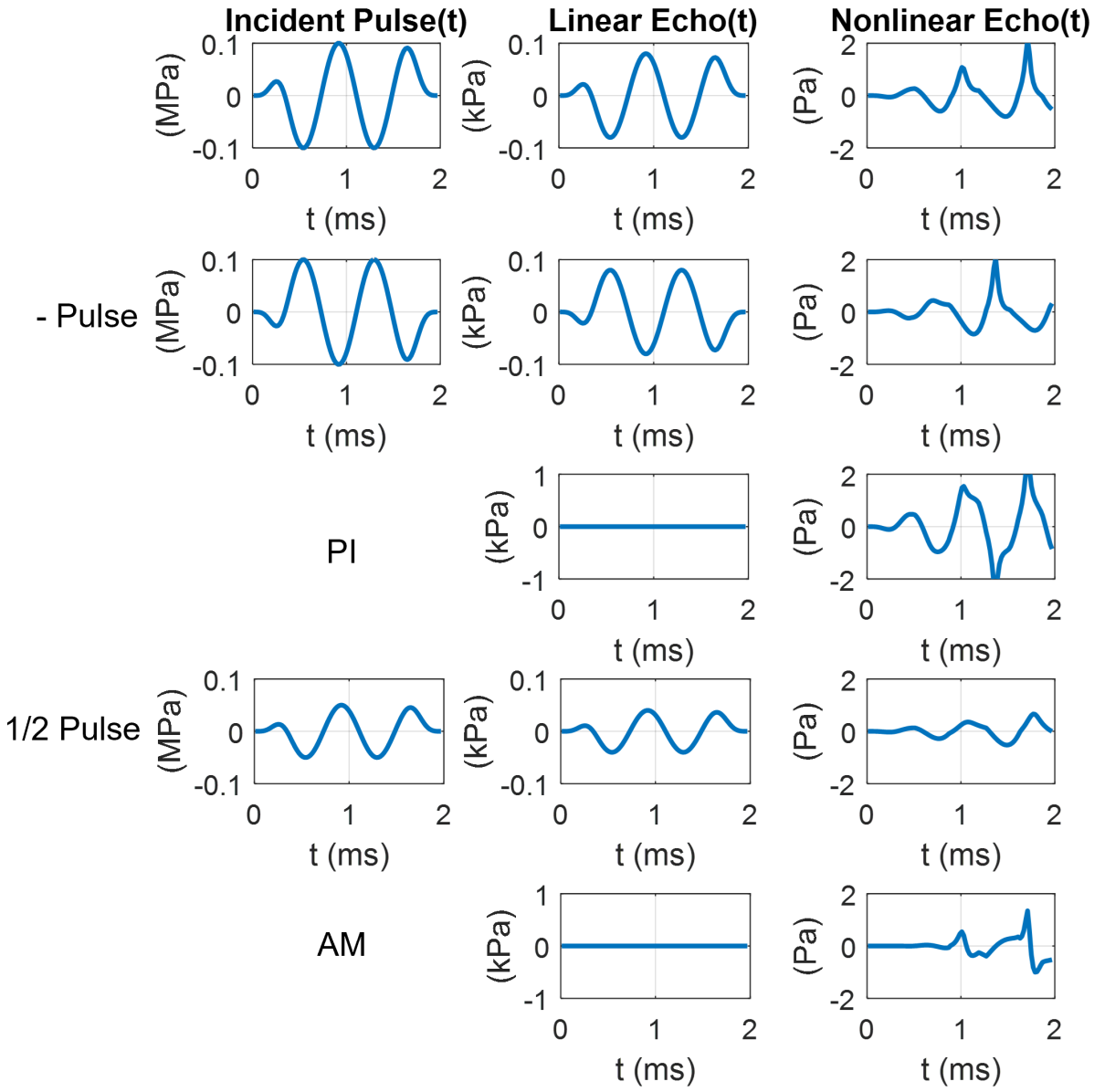


Figure 2.18: PI and AM sequences.

In PI, a two-pulse transmit sequence is used. After transmitting the first pulse and receiving the echoes, the second pulse with an inverse polarity of the first pulse is transmitted. Assuming the linearity of tissue response and non-linearity of contrast agents, tissue and contrast agent signals can be separated by summing the two sets of received signals together. As shown in Fig 2.18, linear signals cancel out completely, whereas nonlinear echoes only cancel out odd-order

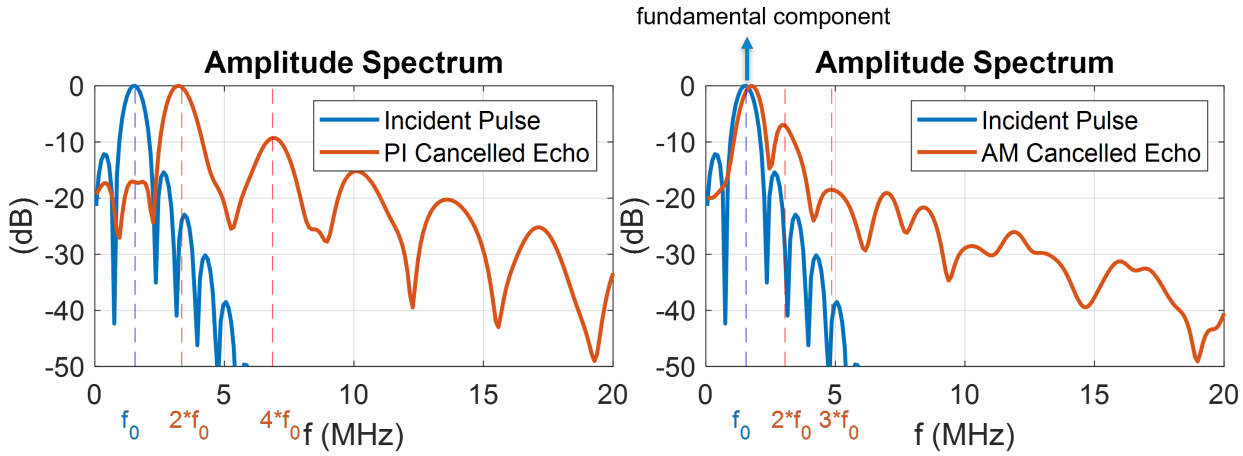


Figure 2.19: Spectrum of PI and AM response.

harmonics of the transmitted signal, with the even-order harmonic signals left (Fig 2.19). Similar to PI, a two-pulse transmit sequence is also employed in AM, with the second pulse replicating the first pulse but half of the magnitude. As contrast agents are sensitive to the incident power, different responses are generated. Assuming tissue emits linear signals in the majority, after subtracting the doubled magnitude echoes of the second pulse from that of the first pulse, linear signals cancel out, and both even and odd order of harmonics are preserved. Thus, the fundamental component (the first order of harmonics) is also preserved. This is advantageous as lower frequency component attenuates less and their reception will be less constrained by the transducer bandwidth.

As a combination of PI and AM, PIAM modulates both the amplitude and phase of the second pulse to achieve a higher SNR level [200]. By increasing the number of pulse repetitions, contrast pulse sequence (CPS) is also developed to improve the sensitivity [204]. Besides, more advanced methods like Golay coded sequences transmit multiple pulses continuously in one transmission event. This can help deliver more energy and thus improve the contrast agent sensitivity at a low level of SNR [210, 202], although it may be more subject to the motion artifact than transmitting multiple pulses intermittently.

2.4.3 Ultrafast Ultrasound Imaging

In conventional medical ultrasound imaging, the view-of-interest was scanned line by line. As shown in Fig 2.20, only one element or a small group of adjacent elements are excited at one time, and independent time delays are applied to form an electronic focus. In conventional ultrasound imaging, a subset of elements is sequentially used to focus on a certain depth, and beamforming is performed line-by-line, then sweeping along the lateral direction generates the final image (left of Fig.2.20). However, the image quality is limited to the focus area and gradually degrades outside. This can be improved by employing several transmit focal depths, then the final image recombines these partial images at different depths, at the cost of reduced frame rate [211]. Whereas in ultrafast ultrasound imaging,he whole array of elements is excited together, a wide field-of-view (plane or diverging) beam is transmitted, followed by digital parallel beamforming, enabling the final ultrasonic image to be reconstructed from a single transmission (right of Fig. 2.20). Thanks to the reduced amount of transmission events needed for one image reconstruction, the frame rate was improved from 50 frames/second to 5000 frames/second [212]. Ultrafast ultrasound was demonstrated feasible using analog parallel-processing devices [213] in the 1970s. However, it was only demonstrated in clinics [212] in the 2010s thanks to the development of the graphical processing unit (GPU) to make real-time image reconstruction feasible.

However, spreading out power among the elements decreases the image contrast, and the increased effective lateral aperture size degrades the lateral resolution. To overcome this problem, coherent plane-wave compounding [216] was proposed. In this method, several plane waves with different angles are transmitted and the beamformed images of these transmissions are summed coherently, which results in a synthetic focusing in transmission (Fig 2.21). This technique enables faster acquisition frame rates for high-velocity flow imaging, higher sensitivity for low-velocity flow applications, and reduced variance by 14 times compared to conventional focused methods[217].

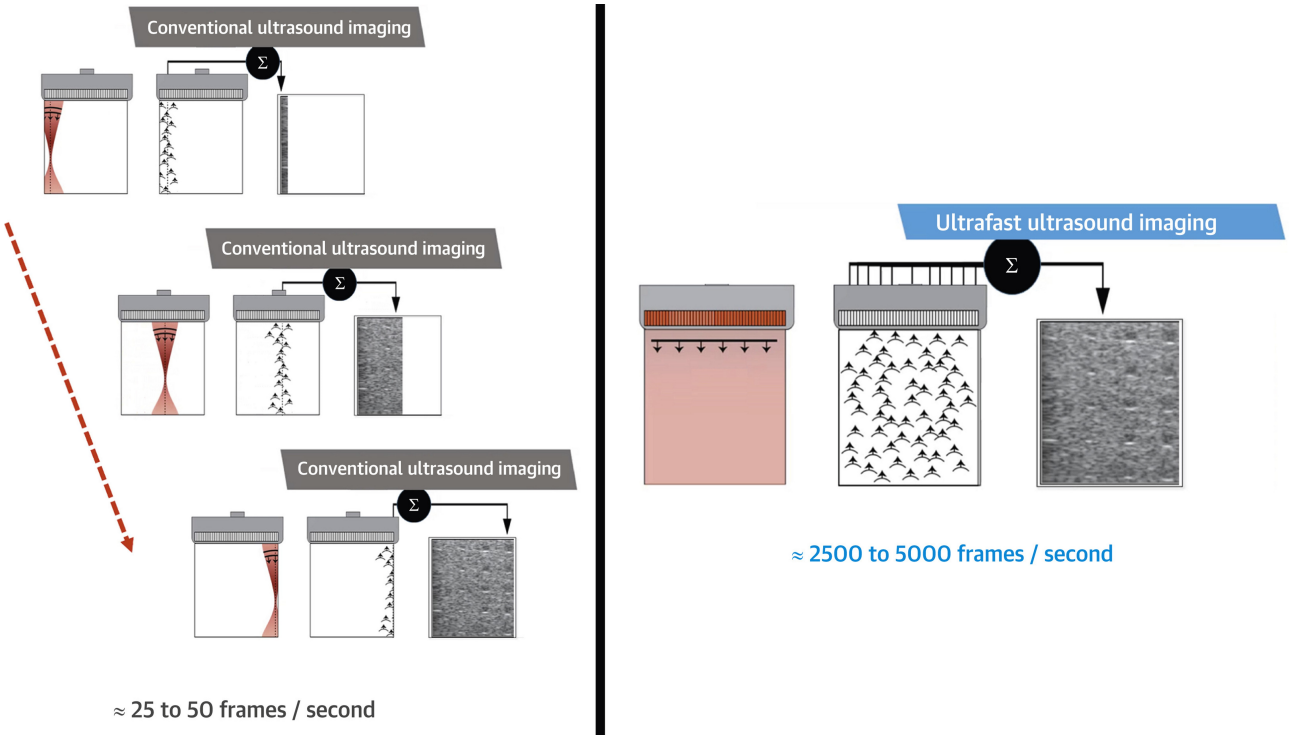


Figure 2.20: Conventional and Ultrafast Ultrasound Imaging, referenced from [214].

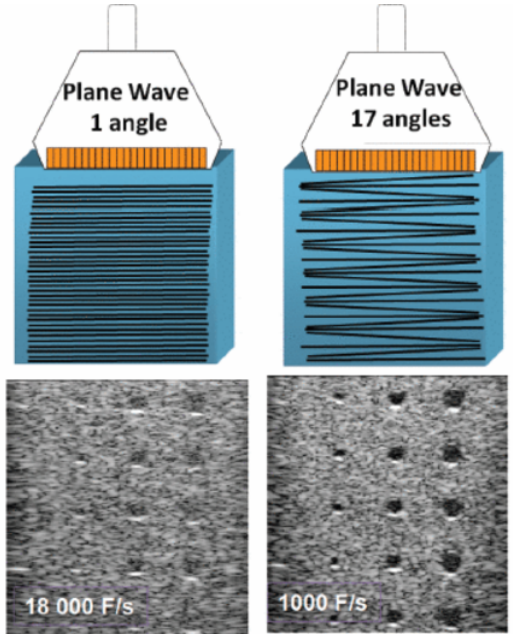


Figure 2.21: Plane-wave imaging with (left) and without (right) compounding, referenced from [215].

2.4.4 Clutter Filtering

In clinics, ultrasound signals come from tissue and blood flow. To extract blood/contrast agent signals from higher-power tissue signals, post-processing methods like clutter filtering are nec-

essary. In conventional ultrasound imaging, three classes of temporal filters are mainly used as the clutter filtering method, including finite impulse response (FIR), infinite impulse response (IIR), and regression filters [218, 219, 220, 221]. All of them are operated along the temporal domain and are based on the assumption that tissues are relatively stationary or slowly moving, whereas blood flow is fast, contributing to different components on the velocity spectra.

FIR filter requires a high number of temporary sampling points to guarantee the performance. However, due to the low frame rate of conventional ultrasound imaging, less than the optimized number of samples are available. IIR filter can alleviate this problem but would introduce the transient response that affects the filtering performance. Different from the impulse response filters, regression filters fit the signals with a curve using the least square regression, assuming that the signal volatility comes from blood flow exclusively [221]. However, tissue motion and comparable slow blood flow pose challenges to their performance.

To solve this problem, eigen-based clutter filtering methods are developed to consider the spatial characteristics of clutter signals. Assuming that tissue signals have higher spatial coherence, it relies on statistical tools to find a set of eigenvectors that represents the clutter space [222, 223] and reconstruct the flow signals using the rest of the eigenvectors.

Since the ultrafast ultrasound technique improved temporal resolution, singular value decomposition (SVD) was proposed to utilize the spatiotemporal characteristic of clutter and blood flow signals and improve the flow sensitivity significantly [224, 225]. In this method, the 2D-t or 3D-t signal is first realigned to a casorati matrix, which is then decomposed into:

$$S = U\Delta V' \tag{2.4.5}$$

where Δ is a diagonal matrix with the diagonal element being the descending sorted eigenvalue. The eigenvalue represents the weight of its corresponding singular vectors contributing to the total energy of the signal. U and V are the eigenvector matrices that contain the spatial and temporal vector basis, respectively.

Considering the higher coherence and stronger energy of tissue, singular vectors of the tissue subspace correspond to higher eigenvalues, which is the lower rank of values in Δ. Whereas random noise contributes the least to the signal energy and corresponds to the highest rank

of eigenvalues. The eigenvalues and eigenvectors in between, then correspond to blood flow signals. Therefore, by choosing a subset of the eigen value and the corresponding eigenvectors, signals from different subspaces can be reconstructed via

$$s_k(x, z, t) = \sum_{k=i}^{j} \lambda_k u_k {v_k}' \tag{2.4.6}$$

SVD has been widely accepted in the field of ultrasound imaging when characterising the blood flow, paving the way for the application of super-resolution ultrasound imaging where extraction of contrast agent signals out of the tissue signals is the prerequisite. It has been shown to have higher localization precision at a higher frequency ($>$ 6 MHz) [184] in SRUS compared to the CEUS technique like PI, at a cost of computational cost. Another limitation of this filtering method is that it assumes the noise and undesired tissue signals are identical across the whole imaging region, which contradicts the reality that both the noise and signal are spatially varying, especially *in vivo*. To solve this issue, researchers tried to separate the RF data into different partially overlapped local segments and choose the threshold locally. This method improves the small vessel flow sensitivity compared to the global SVD but increases the computational cost further [226]. To reduce the computational cost of this filtering operation and achieve real-time processing as PI, researchers tried to either reduce the temporal ensembles or use randomized spatial downsampling methods [227]. Furthermore, to obtain optimal performance, researchers tried to automate the threshold selection process and reduce the computational cost associated with the automation [225, 228]. In summary, this filter is now widely employed in flow-related research and is being actively improved in this field. It is used in all the super-resolution data processing in the later chapters.

2.5 Super Resolution Ultrasound Imaging

2.5.1 2D Super Resolution Ultrasound

Super-Resolution ultrasound has been demonstrated to be able to overcome the wave diffraction limit and visualize microvessels [56, 229, 230, 57, 9, 226, 231, 232] by localizing the spatially isolated microbubble or vaporized nanodroplet [233, 234, 235, 236] signals. It has been investigated widely preclinically [237] on the human brain [25], lymph node [238], breast [10, 9], lower limb [239] and vasa vasorum on the human carotid artery [240].

The majority of the above-mentioned research is completed in 2D SRUS. However, the actual three-dimensional (3D) microstructures cannot be inferred only from a single or few 2D sections. The 2D slices showing tumor tissues in Fig 2.3(a-b) deliver quite limited information about the abnormal density, tortuosity and proliferation behaviour of the whole 3D tumor structure within the 494 x 370 x 200 μm box, compared to the 3D results in Fig 2.3(c-d) and the normal tissue section in Fig 2.2. It is reasonable to expect a similar problem would happen to 2D super-resolution ultrasound imaging, which can also reveal brain microvasculature at this scale, with a resolution high up to 6.5 μm [241]. Consequently, 3D super-resolution ultrasound technique is desired to visualize the 3D microvasculature.

2.5.2 3D Super Resolution Ultrasound

Thanks to the development of both transducer technology and computer hardware, and advances in computation methods, 3D SRUS has attracted increasing research interests. With 3D SRUS, not only the full complex 3D microstructure can be unveiled, but the tissue motion along all directions can be better corrected. This can improve the tracking performance of the contrast agents, especially contrast agents that travel in-and-out of the traditional central imaging plane.

Earlier versions of 3D SRUS involved scanning a 1D probe along the elevational axis to gather several 2D slices of images [57, 242, 243]. However, only two of the three spatial directions can

be super-resolved using the mechanical scanning approach. It also deteriorates the temporal resolution. To achieve SR in all three spatial dimensions, two orthogonal clinical transducers were utilized and 3D imaging was achieved at the overlapped area at the focus [244]. Besides, researchers also introduced multiple rows of parallel elements and tried to localize the elevation positions by fitting parabolas [245] along the elevational direction. Customized transducers, such as a hemispherical transcranial array, were also utilized to see the spiral structure of an ex vivo skull [24], at a cost of high fabrication cost. A row-column-addressed (RCA) array, as an alternative, has been demonstrated to be capable of producing 3D SR images with significantly fewer acquisition channels and a bigger field-of-view (FOV) compared to the full matrix array probe [163].

Full 2D matrix array probe applications have also been studied [25, 26, 27, 17], but the required hardware is complex and expensive. By lowering the number of acquisition channels from 1024 to 512 while sacrificing temporal resolution, multiplexed 2D matrix array [246, 247] was utilized to mitigate the issue. A sparse 2D array with elements following a density-tapered 2D spiral pattern [248] has also been employed to generate 3D SR images [249], to get around the issues of high channel count and huge data volume, albeit with worse initial image quality. Researchers also tried to improve the transmit sequences to minimize the number of transmit and receive combinations at little cost of SNR [250].

However, there are still issues with the clinical application of the 3D SRUS imaging technology due to the volume of data. For most papers cited above, it takes huge computational and hardware costs to generate a high-saturation 3D SRUS image. As claimed in [250], 100,000 volumes acquired within several minutes can take 245 GB of memory. And even using a powerful CPU with 12 cores (Intel Core i9 @2.9 GHz 12 cores, 128 GB RAM @2133 MHz), it takes 3 hours of parallel computing to process the data. Also in [25], 15 mins of volumes were acquired, taking 5h to beamforming on a GPU, and taking 4h to finish the SVD filtering processing on a breathtaking 32-core 3 GHz processor, without disclosing the motion correction computational cost, which usually takes longer than all the above-mentioned processing step.

Besides, slow imaging speed is another bottleneck for this technique's clinical employment. As the suitable concentration of contrast agent needs to be lower than clinical dose to make it

easier to spatially isolate these MBs, a long acquisition time is necessary to generate a produce a complete image of the microvessel [237]. Researchers have attempted to use sparsity-based algorithms [21] to lower the acquisition time to only tens of milliseconds and deep-learning tools with structural priors to only 160 ms for image reconstruction in 2D SRUS [23]. However, in 3D SRUS, the required computational cost for filtering and memory for training 3D volumes will also rise. These studies also ignore the non-linear properties of microbubbles that may introduce various spectral components and asymmetrical patterns to the PSF, which may affect the performance of these methods in practice.

Therefore, the expensive computational cost and long acquisition time is impeding the implementation of such a technique on existing clinical equipment. Solutions need to be proposed to address the aforementioned problems: the compromise between long acquisition time and the saturation of a complete image especially in 2D, the compromise between expensive computational costs and volumetric visualization in 3D, and the underutilization of the nonlinear property of MBs and nonlinear imaging sequence to improve the MB detection sensitivity and thus the acquisition time in 2D/3D.

2.6 Thesis aims and impact

2.6.1 Research objectives

With the question of how can we promote the clinical translation of the SRUS imaging technique, this thesis aims to investigate:

1. A projection SRUS technique that uses a novel probe model to detect information pertaining to a volume with a similar fabrication and computational cost as conventional 2D SRUS in simulation, *in vitro* and *in vivo*.

2. An extension of the method in 1. with different probe models to further improve the projection performance.

3. If monodisperse MB can improve the detection sensitivity during the SRUS processing compared to the commonly used polydispersed MBs in simulation and *in vitro*.

2.6.2 Scientific Contribution

Journal

B. Wang et al., "Broad Elevation Projection Super-Resolution Ultrasound (BEP-SRUS) Imaging with a 1D Unfocused Linear Array," in IEEE Transactions on Ultrasonics, Ferroelectrics, and Frequency Control, doi: 10.1109/TUFFC.2023.3343992.

J. Yan, **B. Wang** et al., "Fast 3D Super-Resolution Ultrasound With Adaptive Weight-Based Beamforming," in IEEE Transactions on Biomedical Engineering, vol. 70, no. 9, pp. 2752-2761, Sept. 2023, doi: 10.1109/TBME.2023.3263369.

(Under Review) M. Lerendegui, K. Riemer, **B. Wang**, . Dunsby, M.X. Tang, "BUbble Flow Field: a Simulation Framework for Evaluating Ultrasound Localization Microscopy Algorithms", ArXiv, 2022.

Riemer, Kai PhD; Tan, Qingyuan MSc; Morse, Sophie PhD; Bau, Luca PhD; Toulemonde, Matthieu PhD; Yan, Jipeng PhD; Zhu, Jingwen MSc; **Wang, Bingxue** MSc; Taylor, Laura MSc; Lerendegui, Marcelo MSc; Wu, Qiang PhD; Stride, Eleanor PhD; Dunsby, Christopher PhD; Weinberg, Peter D. PhD; Tang, Meng-Xing PhD. 3D Acoustic Wave Sparsely Activated Localization Microscopy With Phase Change Contrast Agents. Investigative Radiology ():10.1097/RLI.0000000000001033, November 20, 2023. DOI: 10.1097/RLI.0000000000001033

Conference

B. Wang, K. Riemer, M. Toulemonde, J. Broughton-Venner, X. Zhou and M. -X. Tang, "Volumetric Super-Resolution Ultrasound with a 1D array probe: a simulation study," 2021 IEEE International Ultrasonics Symposium (IUS), Xi'an, China, 2021, pp. 1-3,
doi: 10.1109/IUS52206.2021.9593553.

B. Wang, J. Yan, K. Riemer, M. Toulemonde, J. Hansen-Shearer and M. -X. Tang, "Comparison of localization methods for 3D Super-Resolution Ultrasound Imaging," 2022 IEEE International Ultrasonics Symposium (IUS), Venice, Italy, 2022, pp. 1-3,
doi: 10.1109/IUS54386.2022.9957144.

G. Zhang, **B. Wang**, A. Shah, J. Bamber, and M. -X. Tang, "Contrast-Enhanced Photoacoustic Imaging of Low-boiling-point Phase-Change Nanodroplets," 2019 IEEE International Ultrasonics Symposium (IUS), Glasgow, UK, 2019, pp. 2271-2274, doi: 10.1109/ULTSYM.2019.8925633.

G. Zhang, **B. Wang**, A. Stanziola, A. Shah, J. Bamber and M. -X. Tang, "High Signal-to-Noise Ratio Contrast-Enhanced Photoacoustic Imaging using Acoustic Sub-Aperture Processing and Spatiotemporal Filtering," 2019 IEEE International Ultrasonics Symposium (IUS), Glasgow, UK, 2019, pp. 494-497, doi: 10.1109/ULTSYM.2019.8926149.

Chapter 3

Projection SRUS Imaging

3.1 INTRODUCTION

In the UK's clinical radiology, the most commonly used diagnostic imaging modality is X-ray projectional radiography [251]. Compared with full 3D X-Ray Computerized Tomography (CT), X-ray projectional radiography has much simpler hardware and lower cost, while still containing information pertaining to a broad 3D volume through condensing the 3D volume into a 2D projection image.

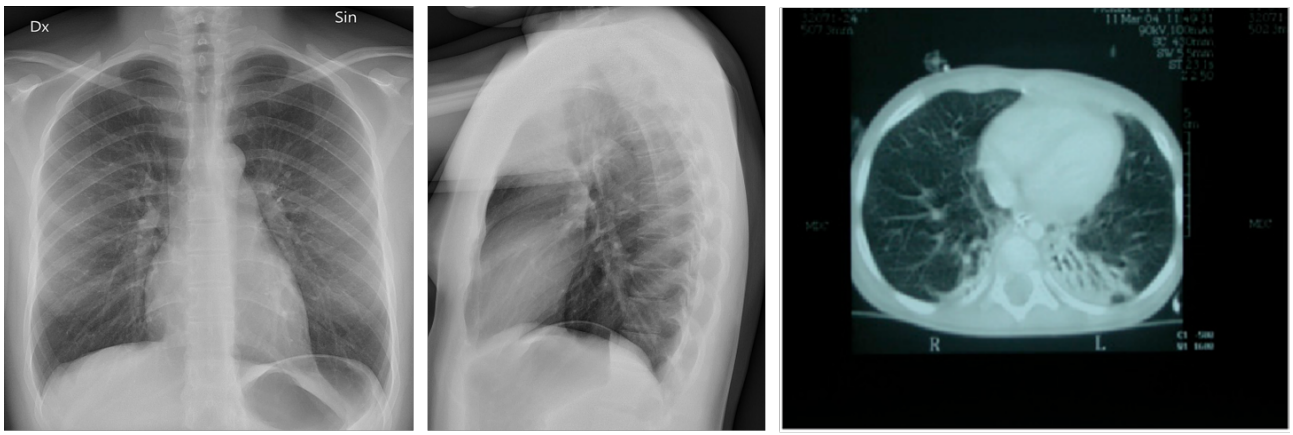


Figure 3.1: A (a) normal posteroanterior (PA) and (b) lateral chest radiograph. (c) A single slice image from a chest CT scan.

This study takes inspiration from X-Ray projectional radiography to investigate a potential alternative solution for generating information pertaining to a broad volume in SRUS. It aims to demonstrate the feasibility of broad elevation projection SR (BEP-SR) imaging in capturing volumetric information using a 1D unfocused transducer array that has the same scale of hardware and computational cost as conventional 2D SRUS. First, a proof-of-concept of BEP-SR is shown with a microvessel phantom in simulation, followed by experimental *in vitro* and *in vivo* results acquired by a 1D unfocused linear array simulated from a 2D matrix array probe. The results were compared with the traditional 1D focused linear array results simulated from the same 2D matrix array probe and 2D matrix array results. The effect of the microvasculature complexity and microbubble concentrations on BEP-SR's performance was also studied.

3.2 METHOD

3.2.1 Transducers

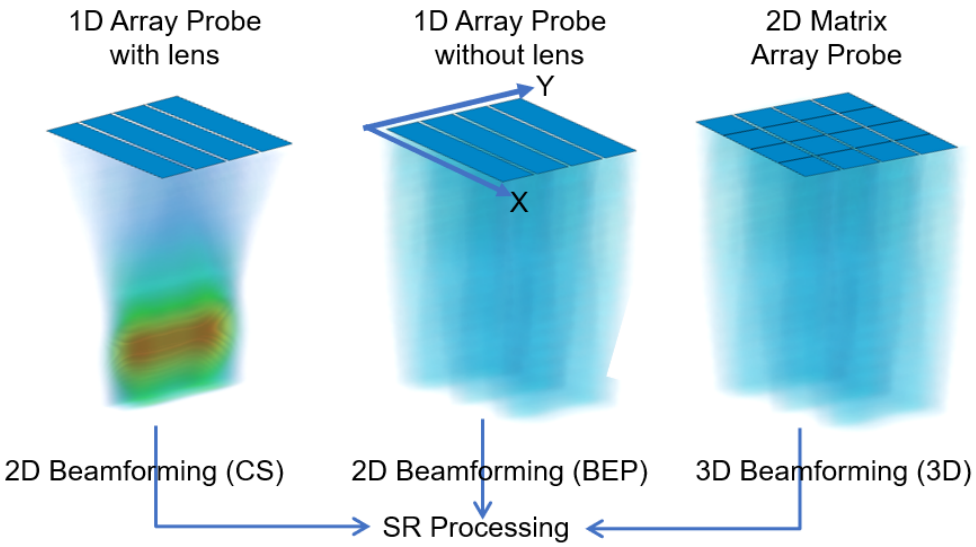


Figure 3.2: Transducer and three imaging schemes. The diagram of the 32*32 matrix array transducer is shown on the right. Central Slice (CS) of the 3D beam formed volume (only receive focused); BEP imaging through plane wave transmission and echoes received and summed along the elevational direction; 3D imaging through plane wave transmission and echo reception by all 32x32 transducer elements. The elevational direction (Y) is switched with the lateral (X) direction regarding the focus, where the elements are continuous and can focus better, eliminating the effect of the blank rows on the acoustic field.

To evaluate the proposed BEP-SR, the performance of several probes of the same aperture size both laterally and elevationally was investigated. 1) an elevational focused 1D array for conventional 2D imaging; 2) an elevationally unfocused 1D array for BEP-SR imaging; 3) a 2D matrix array probe for conventional full 3D imaging as a gold standard comparison. To compare the three probes fairly and remove the effect of variation between different data acquisitions, a 2D matrix array probe, and zero angle plane waves were used for data acquisition, and then data for the 1D array probes with and without a focusing lens were synthesized using data from this 2D matrix array. The 2D probe used was the multiplexing matrix array probe (Vermon, Tours, France) with 1024 elements, a central frequency of 7.8 MHz, and an aperture size of 9.6 mm x 10.2 mm, which has four sub-apertures separated by three empty rows. It is worth mentioning that throughout this investigation, the focus is formed along the lateral direction (X) to focus better using the continuous elements along this direction and eliminate the effect of the blank rows on the pressure field evenness along the other direction. Single zero-angle plane waves were transmitted using all the 32*32 elements simultaneously at 7.8 MHz. The received radio frequency (RF) data was processed in three different ways, one method to synthesize data for the elevationally focused linear array, one method to synthesize data for the elevationally unfocused linear array, and finally a method for conventional full 3D imaging (Fig 3.2):

1) To synthesize the data for an elevationally focused 1D array, the central slice image was taken out of the beamformed conventional 3D B-Mode image, which has a receive focus in beamforming. This method is hereafter referred to as Central Slice (CS).

2) To synthesize the data for an elevationally unfocused 1D array for BEP-SR imaging, the RF data acquired by the 2D array probe was summed along the elevational direction (X), taking the 32x32 channels of the original 2D probe and reducing it to 32x1.

3) The conventional 3D Delay and Sum (DAS) algorithm was implemented using all 32x32 elements.

Table 3.1: Simulation Parameters

Parameter name	**Value**
Centre frequency	7.8 MHz
Transmit frequency	7.8 MHz
Speed of Sound	1540 m/s
Wavelength	197 μm
Element width	0.275 mm
Element kerf	0.025 mm
Element number(matrix)	32*32 (1024)
Element number(1D)	32*1 (32)
Aperture size	9.6 (x) *10.2 (y) mm
Sampling frequency	31.24 MHz
Pulse	2-cycles, Hann-weighted
Apodization	Tukey(0.5)
Elevational Focus Depth	20 mm

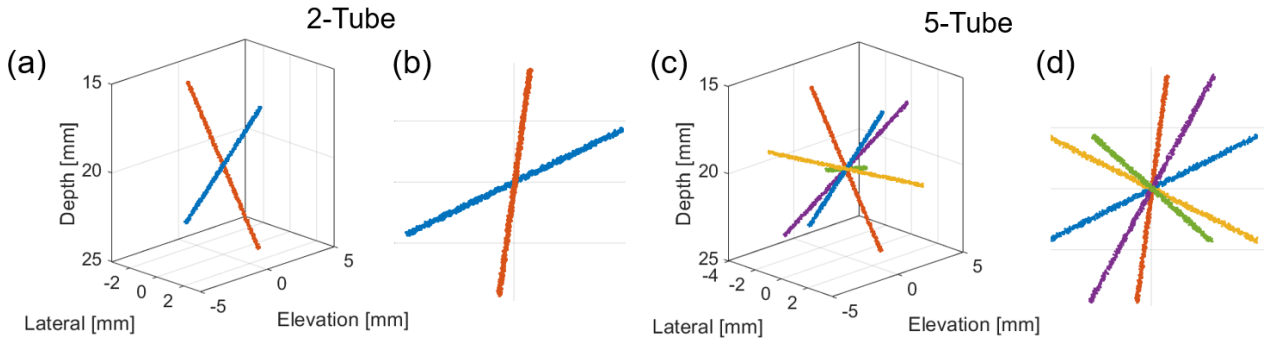


Figure 3.3: Ground truth of the cross-tube simulation phantoms. (a) and (c) show the 3D view of the 2-tube and 5-tube phantom, (b) and (d) show the projection views along X.

3.2.2 Simulation

To validate that these methods of synthesizing 1D array data using a 2D matrix probe are equivalent to using a true 1D array, simulations were performed using Field II [252] with probe parameters shown in Table 3.1. Two different probes with the same aperture size were simulated, one 1D linear array probe with an elevational focus, one 1D linear array probe without

an elevational focus, and one matrix array probe, which has three blank rows between each sub-aperture when it is manufactured. Apodization on transmit was applied laterally but not elevationally.

Microbubbles were simulated as linear point scatterers. In these simulations, only one linear scatterer was present at each frame and was initially placed at (x=0, z=20) mm and moved along the elevational direction with a one-wavelength step size (y=-5:0.2:5 mm). Images were generated using each of the three imaging methods described previously using data recorded from the simulated 2D array, as well as with conventional 2D beamforming methods using data generated for the simulated focused and unfocused linear arrays. The axial localization errors of the scatterers placed at a range of elevation positions were then compared.

A second set of simulations was also conducted to compare the image quality of the three transducers, to do this a micro-sized cross-tube phantom was simulated, and a 2-tube structure and a 5-tube structure (Fig. 3.3) were used to investigate the effect of the vascular complexity, with each of the tubes filled with 1000 scatterers randomly over time. The effect of the scatterer's concentration was also investigated by tuning the number of scatterers per tube per frame from 1 to 5, reducing the total number of frames from 1000 to 200 with the total number of scatterers fixed. For the cross-tube phantom simulation dataset, Gaussian white noise was added to achieve a 3 dB SNR in the RF channel data.

3.2.3 Simulation Evaluation

For the evaluation, the radial intensity profiles within two half-ring-shaped ROIs were measured. The radial profile along different angles within the half-circle ROIs that are 450 and 1050 µm away from the origin was calculated by averaging the pixel intensity with the 20 neighboring pixels along the radial direction.

The localization and tracking performance was evaluated quantitatively by calculating the precision and sensitivity for different methods, as stated in [188, 253], with a localization error tolerance level (searching radius) equal to 1/4 of the wavelength. The evaluation metrics are defined as below:

In localization:

- True Positive (TP): If the localized position is close to the ground truth location.
- False Negative (FN): A ground truth event without any localized events.
- False Positive (FP): A localized event has no pairing ground truth event.

In tracking, only true positive localizations are considered, across two consecutive frames:

- True Positive (TP): The associated ground truths of two paired localizations have the same bubble ID.
- False Negative (FN): A bubble pair in ground truth is not associated with a linked & localized pair of bubbles.
- False Positive (FP): A linked & localized pair of bubbles is not associated with a bubble pair in ground truth.

The precision and recall are then calculated as

$$Precision = \frac{TP}{TP + FP}, Sensitivity/Recall = \frac{TP}{TP + FN} \tag{3.2.1}$$

3.2.4 *In vitro* Experiments

A series of *in vitro* experiments was then conducted to explore the experimental image quality of the BEP method. A 7.8MHz multiplexed matrix probe used in this study was driven by a Vantage 256 system (Verasonics Inc., Kirkland, WA, USA). This probe has no physical elevational focus, providing the flexibility to synthesize the data for the different types of 1D transducer arrays. To reduce the effect of motion between compounding transmissions and switching between different sub-apertures, the transmit sequence was kept as simple as

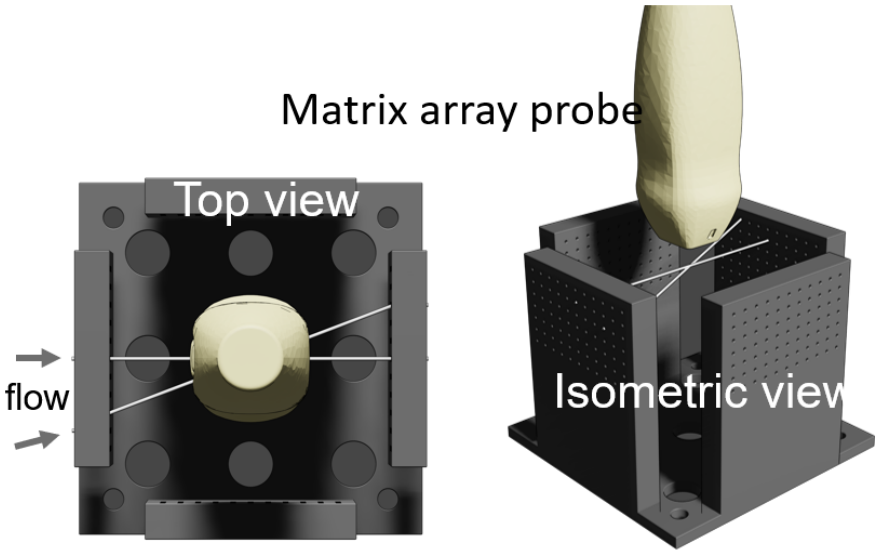


Figure 3.4: Top and isometric view of the experiment set-up. These two 200-micron microtubes were positioned using a grid of holes on the sidewalls, with an acoustic absorbing pad at the bottom of the phantom.

possible. Four sub-apertures were driven at the same time to send zero-angle plane waves, without any steering and compounding, and then each sub-aperture was used to receive the RF signal sequentially, which means that each frame of acquisition consists of four separate acquisitions. The mechanical index (MI) measured in the middle of the probe was 0.05. A total number of 1000 Frames of images were acquired with a frame rate of 500 Hz without any compounding. Two 200 µm ± 15 µm Hemophan cellulose tubes (Membrana, 3M, Wuppertal, Germany) with a wall thickness of 8 ± 1 µm were crossed at a depth of 16 mm, where the edge waves caused by the dead rows between sub-apertures diminish below -14 dB [254]. A probe holder was 3D-printed to help align the probe with the phantom. One tube was kept in a central slice of the 3D imaging volume as much as possible, while the other one was tilted and spanned across the 3D space, as shown in Fig. 3.4. Microbubbles (MBs) were made in-house according to the method stated in [255], and the MB solution was diluted 5000 times, resulting in a concentration of 106 per ml. Then the diluted suspension was injected into the tubes with a constant flow rate of 100 µl/min using a syringe pump (Harvard Apparatus, Holliston, MA, USA), which equals to an average flow speed of 50 mm/s. Volumes were composed of 51 × 101 × 103 voxels with 100 µm in all three spatial directions.

3.2.5 *In vivo* Experiments

To explore the BEP method in an *in vivo* setting rabbit kidneys were imaged. The experiment was authorized by the Animal Welfare and Ethical Review Body of Imperial College London and followed the Animals (Scientific Procedures) Act 1986 (No.P15180DF2; Date: 16th, March 2017). A specific-pathogen-free New Zealand White rabbit (male, HS-DIF strain, age 13 weeks, weight 2.4 kg, Envigo, UK) was sedated with acepromazine (0.5 mg/kg, i.m.) and anesthetized with medetomidine (Domitor, 0.25 mL/kg, i.m.) and ketamine (Narketan, 0.15 mL/kg, i.m.). A bolus of 0.1 ml MBs made in-house was injected into the rabbit. Imaging was performed on its left kidney after it was shaved. The same imaging sequence as the *in vitro* experiment was used to collect 1500 frames of images with a frame rate of 500 Hz.

3.2.6 Post-Processing

For the experimental datasets, RF data from four sub-apertures were combined and beam formed to reconstruct a single 3D volumetric image using the 3D DAS algorithm. Then SVD filtering [256, 257, 258] was applied to the beam formed data to remove the strong reflections from the tube walls *in vitro* and tissue signals *in vivo*. For the *in vitro* dataset, the SVD threshold was chosen as the turning point of the singular value curve [258], by cutting the first singular values, while for the *in vivo* dataset, it was chosen by cutting off frequency components below 5 Hz. The BEP datasets of the simulation and *in vitro* experiment were generated by summing the RF data along the X direction as indicated in Fig.3.2, and the focused array image was generated by taking the central slice from the 3D BF image along the X direction, both the dataset *in vitro* followed by the same method of SVD filtering processing. For the *in vivo* experiment, because of the diverging-shaped characteristic of the kidney microvasculature, projection imaging was performed along Y instead as more structures can be seen in the final imaging results.

Once the MB-only datasets were acquired, an initial noise threshold was applied to remove the noise, and then normalized cross-correlation (NCC) was performed between the PSF template that was generated by simulating a single scatter at (x=0, y=0, z=20) mm and the MB-

only image. Correlation coefficients below 0.55 were discarded and local maxima detection was performed to isolate MBs. Then a small patch (5*5 for 2D imaging and 5*5*5 for 3D imaging) around each maxima was non-linearly interpolated to translate the coefficient map to the high-resolution level, on which the maximum pixel was localized. The final localization image was plotted by accumulating these points and smoothed using a Gaussian kernel, whose size accounts for the localization uncertainty due to the existence of noise [259]. 2D Kalman tracking [6, 260, 261] was used to track and calculate the velocities. For the 3D datasets, only two out of three coordinates of the localized positions were used to generate the projected velocity maps of 3D as a reference.

3.3 RESULTS

3.3.1 Simulation

Single Scatter

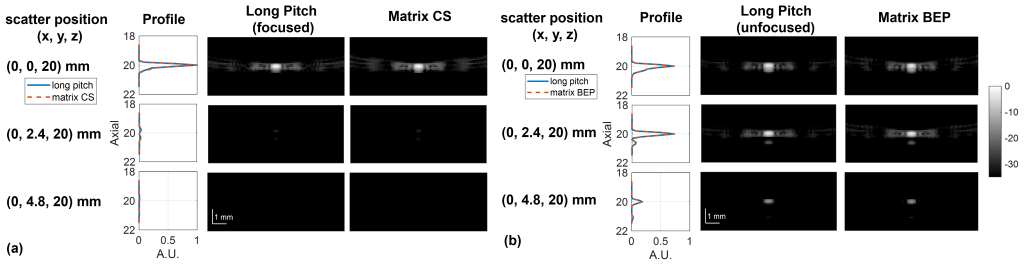


Figure 3.5: Comparisons of long pitch 1D array probe (a) with lens and (b) without lens with the matrix array probe results, including the intensity profile along the axial direction when the single scatter is placed at y=0 (first row), y=2.4 (second row) and y=4.8 mm (third row) respectively, and corresponding beamformed images. The bar indicates a length of 1mm. Supplementary material shows localization results between the long-pitch 1D unfocused and focused linear array with the matrix approximation.

Fig. 3.5(a) compares the simulation results of the focused 1D linear array probe with the matrix array probe when the single scatterer in each frame is placed at different elevational positions, the x, y, and z indicate the lateral, elevation, and depth, respectively, in the cartesian coordinate. The images were normalized by the maximum intensity and then log compressed.

Looking at the RF data, the intensity profile along the axial direction, and the beamformed images, the focused long pitch and CS methods show little difference, validating that the matrix array probe can be used to synthesize data for the focused 1D array.

Fig. 3.5(b) compares the simulation results of the unfocused 1D linear array probe with the matrix array probe when the single scatterer in each frame is placed at different elevational positions. The images were normalized by the maximum intensity and then log compressed. Looking at the intensity profile along the axial direction and the beamformed images, the unfocused long pitch and BEP methods show little difference, validating that the matrix array probe can be used to synthesize data for the unfocused 1D array. Stronger grating lobes in the matrix array results are likely caused by the dead rows between different sub-apertures within the matrix array probe.

Fig. 3.6 compares images of the single scatterers all generated using the data recorded on

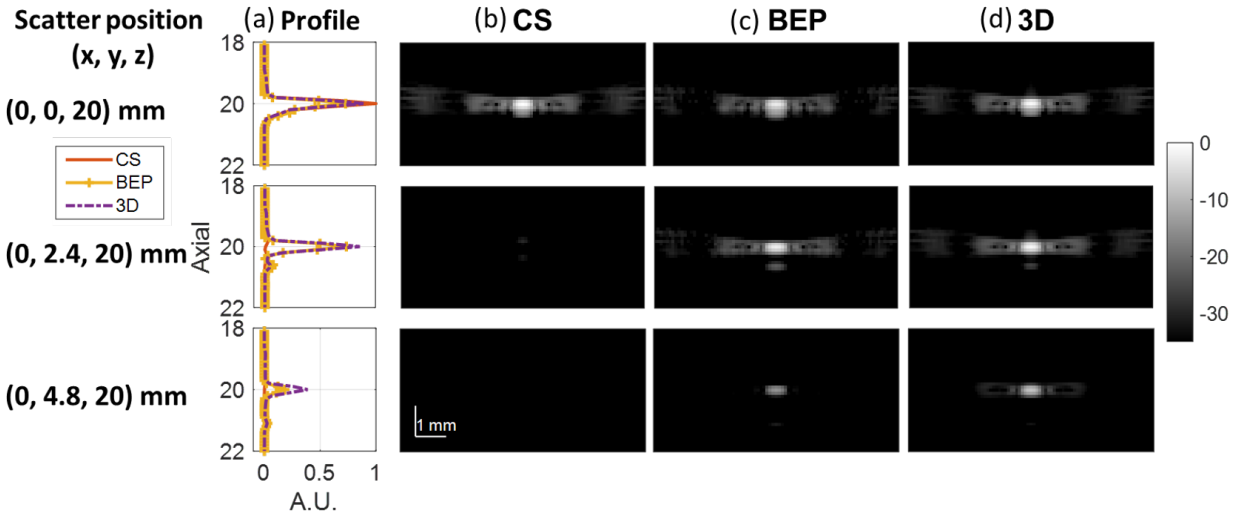


Figure 3.6: (a) The intensity profile along the axial direction when the single scatter is placed at y=0 (first row), y= 2.4 (second row), and y=4.8 mm (third row) respectively. (b) shows the central slice (CS) of the beamformed 3D image; (c) shows the image of the projection method; (d) shows the MIP image of the 3D beamformed image along the projection direction. The bar indicates a length of 1mm.

the simulated 2D array, which was then used to synthesize the focused and unfocused linear arrays, in the same way as will be done in the experiments. Both the 3D and BEP methods can detect the scatterers across a wide elevational range, while the focused method cannot. Specifically, Fig. 3.6(b) shows that an elevational focus omits scatterers that are not within the central imaging plane. In the BEP method, the scatterer is visible even if it is placed at

the boundary of the imaging volume (y=4.8 mm). The last column is the maximum intensity projection (MIP) image of the 3D volume. It shows that BEP is comparable to the 3D method in capturing the scatterers within the 3D volume. Fig. 3.6(a) shows the axial intensity profiles for different datasets. It shows that only BEP and 3D methods can detect off-center plane scatterers, although the amplitude of the signal varies significantly depending on the location of the scatterer.

Fig. 3.7(a) shows the peak intensity of the PSF when a single scatterer is placed at x = 0,

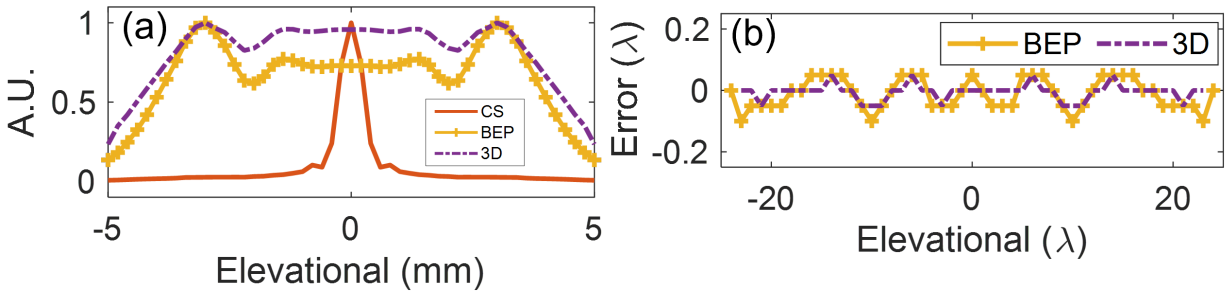


Figure 3.7: (a) Imaging sensitivity along the direction for the four imaging methods. (b) Axial localization errors when moving the single scatterer along X.

z = 20 mm but at different elevational positions. The peak intensity profile decreases sharply when the scatterer is slightly out-of-plane in the CS method, while the BEP and 3D methods have similar elevational coverage, thanks to the removal of the elevational focus, expanding the sonification range of BEP along this direction to a similar level as that of the 3D imaging. When the scatterer reaches the edge, the 3D method performs slightly better than BEP in preserving the intensities at the side. Fig. 3.7(b) shows the axial localization error in wavelengths of the post-processing results for the BEP and 3D SR imaging methods. The lateral localization errors are all close to zero for these three methods and were not shown. The axial localization errors for the CS method are also not shown in this figure, as any scatterer beyond the central region cannot be detected as their intensities fall below the initial noise threshold. The axial localization error of the BEP method is slightly larger than the 3D method and is fluctuating around zero as the scatterer position moves along X, though the error never exceeds 0.1 λ.

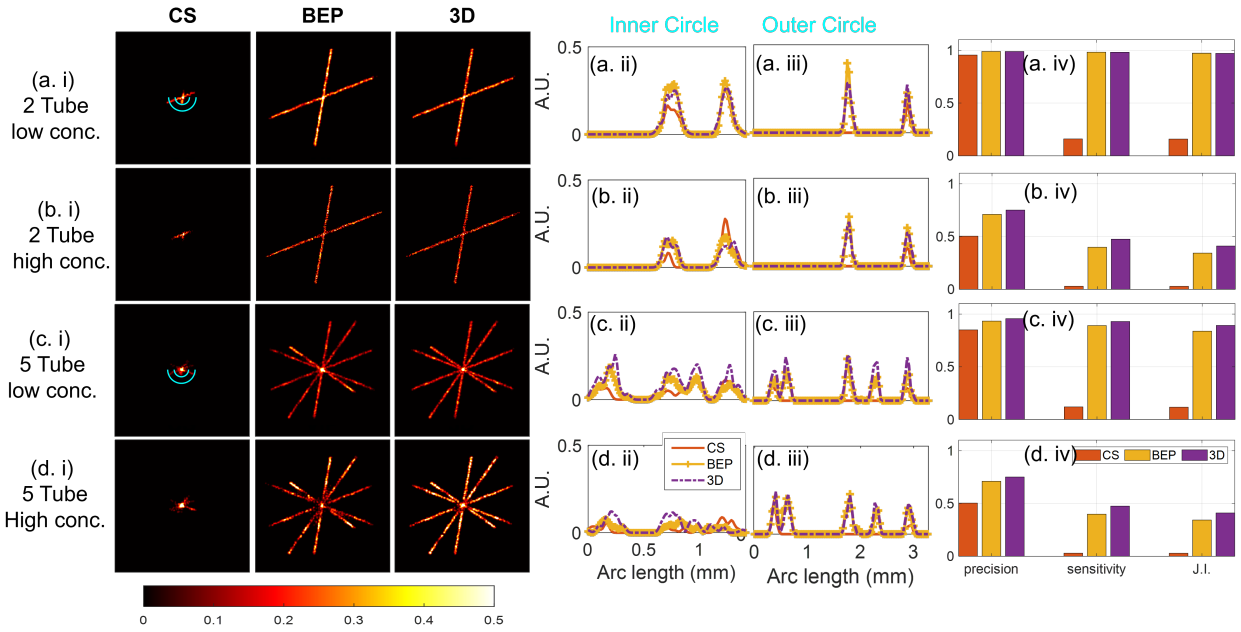


Figure 3.8: Localization images of the (a.i) - (b.i) 2-tube and (c.i) - (d.i) 5-tube phantom, with lower scatter concentration (low conc.) and higher scatter concentration (high conc.), produced by using the three methods: Central Slice (CS), projection, and the MIP of 3D along X. (a.ii) – (d.iii): Radial intensity of the SR images along the cyan half rings, which are (a.ii) – (d.ii) 450 and (a.iii) – (d.iii) 1050 µm away from the origin. The radial profile was measured by averaging the neighboring 20 pixels. (a.iv) – (d.iv) Evaluation Parameters of precision, sensitivity, and Jaccard Index (J.I.)

Cross-Tube Phantom

Fig. 3.8 shows the localization images of the matrix array probe results for the 2-tube and 5-tube phantoms with different scatterer concentrations. Localization results were also generated using the long-pitch 1D unfocused and focused linear array, these images have been placed in the supplementary material. Fig. 3.8 (a.i) and (c.i) show the results of low scatterer concentration when each frame has 1 scatterer per microtube, i.e. there are 2 and 5 scatterers present at each frame in total in the 2-tube and 5-tube phantoms, respectively. With the ground truth shown in Fig. 3.3. The CS method can only image the central part of the phantom, the third column shows the maximum intensity projection (MIP) of the 3D localization results on the same imaging plane as the other three imaging methods. The structural information captured by BEP-SR is comparable to the 3D SR method. As the scatterer concentration increases in Fig. 3.8 (b.i) and (d.i), where each frame has 5 scatterers per microtube, it is shown that the majority of the microtube structures are missing in the CS method, while

most of them are visible in the BEP and MIP of the 3D results. It means that when both the structure complexity and scatterer density increased, both the BEP and MIP of the 3D methods witnessed an image deterioration, shown as a dark central region where the microtubes get closer. When the scatterer concentration is very high, all the imaging methods fail to resolve the center of the structure. In Fig. 3.8 (d.ii), the intensity curve of the BEP-SR method shows a more prominent intensity reduction than the 3D SR curve compared to the low concentration simulation results in Fig. 3.8 (b.ii). This indicates that the BEP-SR method is more vulnerable to higher bubble concentrations and complex micro-vessel structures. This may also potentially cause more inaccurate tracking when the sparsity requirement is not satisfied, as spatially separate scatterers are more likely to overlap along the projection plane and cause localization errors and tracking confusion. In Fig. 3.8 (a.iv) – (d.iv), the sensitivity of the BEP method saw a considerate increase compared to the CS method and is close to the 3D method, notwithstanding the scatterer concentration and structure complexity, although an abrupt drop in the sensitivity and Jaccard Index as the scatterer concentration increased can be noticed. In Fig. 3.8 (d.i), when the scatterer concentration is very high, all the imaging methods fail to resolve the center of the structure.

3.3.2 *In vitro* Experiments

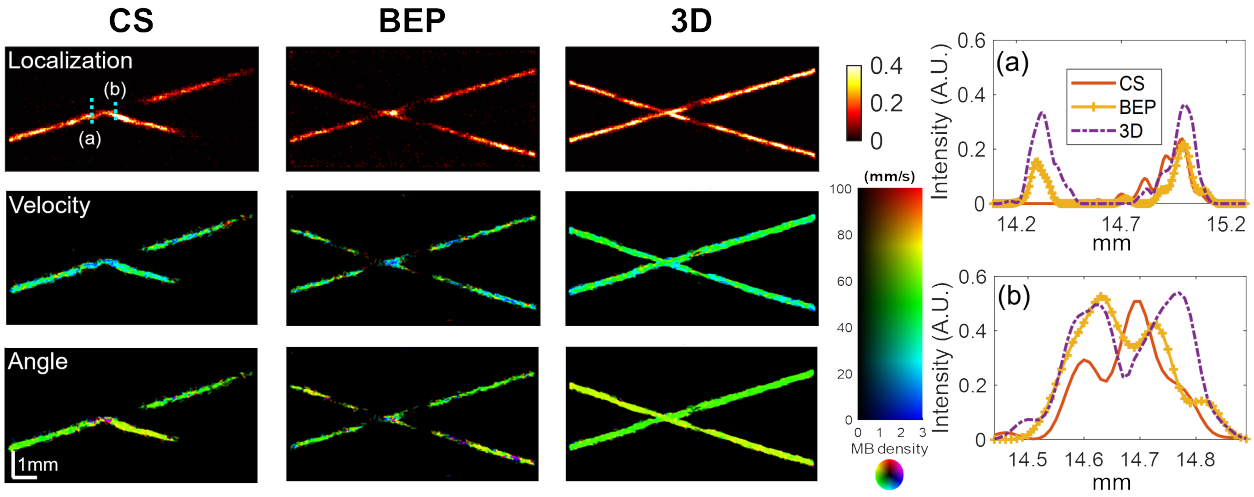


Figure 3.9: *In vitro* localization, tracking velocity results with center slice image (CS), projection images (BEP), and MIP image of the 3D volume along the x direction. Intensity profile along the (a) left and (b) right dashed cyan lines indicated in the CS image.

Fig. 3.9 shows the localization, velocity and flow direction images of different imaging methods with the microvascular flow phantom shown in Fig. 3.9. The localization images are self-normalized for each imaging method. Therefore, the color describes the relative brightness. More specifically, the brighter 3D localization results indicate a more uniform localization performance of the 3D imaging technique. The similar structure shown in the localization and velocity image of the BEP image shows its ability to not only localize, but also track microbubbles that travel in-and-out of the plane, and the calculated velocity is very close to the experimental set-up, of 50mm/s. In the CS imaging method, only parts of the 3D tube phantom can be seen, whereas the localization image of the BEP method shows a similar structure as the MIP of the 3D result, at a cost of less resolving ability, which is confirmed by the intensity profile along the dashed cyan lines. In Fig. 3.4(a), BEP and 3D imaging resolve the profile of two peaks coming from the in-plane and out-of-plane tubes, respectively. In contrast, CS can only detect the profile of the in-plane tube. Whereas in Fig. 3.4(b), same as the other two imaging methods, CS can detect the profile of the out-of-plane tube that stays closer to the center imaging area. Besides, the two peaks resolved by BEP are closer than that of the 3D that serves as the reference, which indicates the inferior ability of BEP in resolving two close tubes or objects in higher concentration areas.

3.3.3 *In vivo* Experiments

Fig. 3.10 shows the localization and tracking images of the left rabbit kidney using different imaging methods. In the CS image, a limited number of microbubbles can be detected and localized, whereas the localization image of the BEP method shows a much denser network of microvessels. The results show that the BEP method has similar elevational coverage to the MIP image of the 3D acquisition, although with a degraded level of detail. This is likely due to the overlapping signals in the projection direction within the complex microvasculature obscuring each other and impacting the localization. The dashed lines show locations that demonstrate the particular advantage of the BEP method. When the vessel network stretches out from the central imaging plane, it can no longer be reconstructed with the CS method. The BEP method,

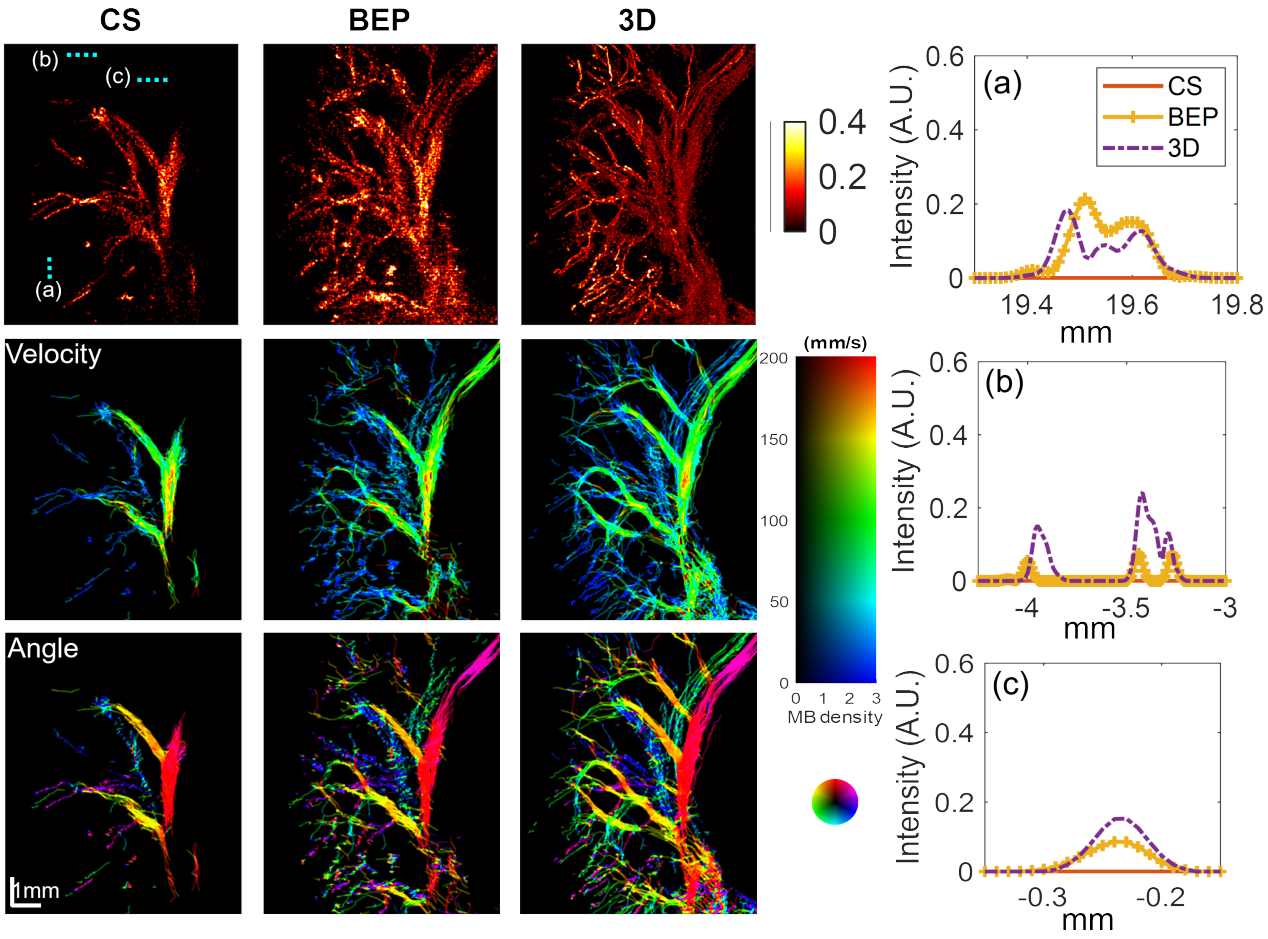


Figure 3.10: *In vivo* localization, velocity amplitude, and velocity angle maps of the central slice, BEP, and MIP of the 3D imaging methods along the y direction. (a)- (c) Intensity profile of the localization image along the dashed cyan lines as indicated in the localization images.

on the other hand, successfully captured and tracked the out-of-plane microvasculature. This is further confirmed by the 3D result and the intensity profile in Fig. 3.10(a)-(c), where the intensity profile of the CS method is flat, and both the BEP and 3D methods see peak profiles.

3.4 DISCUSSION

Inspired by clinical X-ray projectional radiography, this study demonstrates that it is feasible to obtain micro-vessel information over a large volume with a low computation cost using projection super-resolution ultrasound. In this proof-of-concept study, we have demonstrated in both simulation and experiments that BEP-SR can visualize both vascular structures and 2D flow velocity within a 3D volume, the majority of which are not visible using a classic 1D

linear array that has an elevational focus. Such an approach could significantly expand the field of view of SRUS in the third dimension without any additional hardware cost and data transfer/processing cost compared to the conventional 2D imaging method.

Table 3.2 shows the comparison of the different imaging methods when processing one *in vivo* dataset. Compared with the 3D imaging method, the BEP method only needs 32 channels of RF data, a 32-fold decrease in transducer complexity, 10 times less beamforming time, 140 times less memory space, and 360 times less SVD processing time. This simplicity will facilitate the clinical translation of BEP-SR.

Table 3.2: Computational Cost

	CS/BEP	**3D**
Channel Number	32	1024
Image Size	131*81*1500	131*81*91*1500
(100 μm isotropic pixel/voxel)	(z, x, frame)	(z, x, y, frame)
Memory Size	127.3 MB	18.2 GB
Beamforming time (on NVIDIA TITAN Xp)	2 mins	25 mins
SVD processing time (on 128GB RAM)	20 seconds	2 hours

BEP-SR would be ideal for imaging tissues when contrast enhanced ultrasound signals are sparse. When we consider that BEP-SR condenses multiple planes' tracks into one projection image, to reduce overlapping in localization and crossed tracks in tracking processing, a lower concentration of contrast agents than is commonly used in conventional 2D SRUS may be preferred. Therefore, for tissue with denser vasculature, more compromise between bubble concentration and acquisition time is needed to ensure the bubble signals are well separated to ensure localization and tracking performance. On the other hand, the proposed method offers a framework where a balance can be achieved between bubble concentration (and hence acquisition time) and volume coverage. Even in cases where long acquisition time is not practical, BEP-SR can still produce localization maps of vascular structure but within a larger volume and can be highly valuable themselves. Furthermore, the systematic localization errors shown in Fig. 3.7(b) may also cause some differences in the vascular structures between the BEP-SR

and the MIP image of full 3D SRUS results.

Compared to the BEP-SR approach, RCA probes can generate 3D SRUS images with an order of fewer elements compared to a full matrix array probe, while the BEP-SR approach can only generate 2D SRUS image that is the projection of a 3D volume along the elevational direction and does not have the elevational resolution. However, BEP-SR can benefit from the low computational cost by performing 2D beamforming, filtering, localization, and tracking compared to 3D (see Table 3.2), enabling real-time fast SR/ULM processing and still containing information pertaining to the whole volume. Additionally, while the RCA probe is dramatically less expensive and complex than a full matrix array to fabricate, simply taking the 1D arrays already in production and changing the focusing lens to a flat lens would facilitate faster translation.

Additionally, given that the typical clinical probe has an elevational pitch of just about 10 mm, it is worried that employing such a large elevational pitch for this method demonstration may overstate the volume expansion effect of BEP. However, the argument is that the proposed probe and the following BEP method are not constrained by modifying the lens of current 1D probes. Such an unfocused probe can be made from scratch with a large elevational pitch and utilized on the existing imaging devices specifically for SRUS imaging.

Similarly, a matrix probe is not a requirement for BEP-SR imaging. In this paper, a matrix array probe was used in both simulation and experiments for a fair comparison of the different synthesized probes. It is worth noting that the 2D matrix array, the 1D focused linear array, and the 1D unfocused array each have the same elevational size in both the simulations and experiments, as such the information captured by the 2D matrix array after summing the signals is a fair approximation of the 1D unfocused array. One potential concern of using a matrix array probe is that increased cross-talk caused by more channels and the multiplexing scheme may affect the results. But considering the main effect of cross-talk is the increased noise level that will degrade the imaging performance, with fewer channels and a lower cross-talk level, an actual 1D unfocused probe could potentially generate better BEP-SR results. Further study needs to verify this using such a probe.

It should be noted that even with the existing 1D array SRUS imaging, there is always a slice

thickness of the 2D images. Because of the inherent slice thickness of the existing 1D focused probe, 2D SRUS images already cover vessels in a volume. Researchers have utilized this property to infer the third-dimensional information of microbubbles in 2D imaging [262]. However, by using an unfocused lens in BEP-SR, such a field of view can be significantly expanded. In this study, our results suggest that the elevational thickness of the imaging volume was increased from about 2 wavelengths to several millimeters, representing an order of magnitude increase in the elevational coverage at the focal depth. It is also possible to use a diverging lens to further expand the field of view [263].

In BEP-SR, each single transducer element is long in the elevational direction, in Fig. 3.7(a), the imaging sensitivity of the BEP method is slightly reduced in the central imaging plane. This is likely due to the lack of apodization. Integrated apodization can help improve the sensitivity profile along the elevational direction, and can also help reduce the edge wave levels that can improve the axial localization shift, such as what has been applied previously to the RCA array probe [264].

The elevational size of the 1D transducer aperture determines the size of the BEP imaging volume being covered, but increasing the aperture size can compromise the localization performance in the near field. Depending on the scatterer's location, the backscattered signals will arrive at different parts of the long single element at different times. The coherence summation of the scattered signals along the single element could elongate the PSF, causing oscillating axial localization errors in BEP-SR. However, our results show that the maximum error along the axial direction using NCC is no more than 0.1 λ, which is still well below the diffraction limit. Furthermore, it is worth mentioning that this axial localization error will decrease as the imaging depth increases. This is due to the fact that elevational displacement from the imaging plane is incorrectly attributed as an axial displacement in 2D time of flight beamforming, as the increase in time of flight between the source and the element is incorrectly assumed to be due to a greater axial depth. For the same elevational displacement, the elevational angle between the source point and the imaging plane is lower at greater imaging depths, as such this axial displacement error will likewise be reduced at greater depth. This may be further addressed by alternative localization methods using sparsity-based method [265] or deconvolution [7, 261] if

the system PSF can be fully characterized.

The experiment transmission-reception sequence is different from the simulation where all 1024 elements received signals at the same time. However, with a pulse repetition frequency (PRF) at 2000 Hz and, a flow speed of 50 mm/s, the moving distance of bubbles within the switching time of sub-apertures is around 25 um, which is 1/8 of the wavelength, whereas the size (full-width half maximum) of a PSF using the DAS reconstruction method is about 20 times larger [266]. Therefore, we assume that the microbubbles are stationary within the switching time of sub-apertures, and the two methods would generate the same results.

Microbubble dynamics simulation [267] would be desirable to simulate MB's response properties but not essential in this proof-of-concept study as the aim of the study is to investigate the spatial coverage of the proposed BEP-SR imaging method, and the performance of the BEP method in velocity tracking was investigated experimentally. One concern is that the velocity is downscaled due to projection operation on a 3D velocity vector, which is a common issue for tracking in 2D due to the volume-averaging effect. In future work, it is possible to infer the direction vector by calculating how the image feature changes along one tracking path, which can be used to correct the projection bias on the speed calculation.

Furthermore, one challenge of the clinical translation of conventional 2D SR US is that the target position does not stay in the central imaging plane due to motion during the acquisition, with the BEP imaging method, a certain amount of volume will always be covered without significant motion, which can help to keep the target tissue in the view, and thus help with reproducibility. On the other hand, BEP-SR will be more vulnerable to motion as structures may have different motion displacements within a volume, causing different levels of blurriness in the projected image.

It should be noted that in the experimental results, the brightness of the microtube phantom varied significantly along the tube, which is likely caused by the non-uniform pressure field in this direction due to the existence of gaps between the four sub-apertures of the Vermon matrix transducer. This phenomenon is less apparent in the 3D result as the 3D cross-correlation localization algorithm with an order higher convolutional region may help to detect more weak signals than the 2D version.

3.5 CONCLUSION

In summary, this study demonstrates that BEP-SR can obtain micro-vasculature and flow velocity information over a large volume using a linear 1D array probe without an elevational focus lens. The technique requires significantly lower hardware and computing resources than the full 3D SRUS and is comparable to that required by a classical 2D imaging technique.

Acknowledgment

We would like to thank Dr. Jacob Broughton-Venner for the discussion and Mr. Qingyuan Tan for his help with the plot of the figures.

Statement of Contributions

Mengxing and Bingxue contributed to the concept of this study. Xiaowei helped with the field II simulation scripts, Matthieu helped with the Verasonics scripts, Kai helped with the in vitro and in vivo experiments, Jipeng Yan helped with the tracking algorithms. Cameron helped with the proofreading. Bingxue finished the simulation, in vitro and in vivo experiments, and the data analysis. All the people mentioned above contributed to the writing of this chapter.

Chapter 4

Multi Aperture Projection SRUS Imaging

4.1 INTRODUCTION

According to the official report released in 2021 by the NHS England [105], X-ray projectional radiography is the most widely utilized diagnostic imaging modality in the UK's clinical radiology, which was performed two times more than X-Ray Computerized Tomography (CT). Compared to CT, X-ray projectional radiography uses simpler hardware and lower computational cost, while still condensing information within a 3D volume into a 2D projection image. Inspired by this efficient imaging modality and its significant clinical application value, BEP-SR was previously proposed to condense information within a volume into a projection image using a linear probe without an acoustic lens, while using the super-resolution technique to mitigate the problem caused by deteriorated elevational resolution, with a significant decrease in channel numbers and computational cost. However, this BEPSR technique requires more sparse contrast agent signals than conventional 2D SRUS since the projection operation requires avoiding signals overlapping along the elevational direction onto the projection plane. Especially when the proposed 1D unfocused linear array has a long element height and thus a huge projection volume along this direction, signals are more likely to overlap.

Compared to a 1D array probe, a 1.75D array probe has a few more rows of elements and thus reduced element height for each row along the elevational direction. An elevational focused 1.75D array has been used in previous studies to improve the CNR by correcting the two-dimensional aberrations [268], narrowing the elevation beamwidth, and thus improving the contrast of the image [160]. An unfocused 1.75D array probe has also been used as an alternative to a 2D matrix probe and can perform three-dimensional ultrasound and photoacoustic imaging [269], but the 1280 channel number is even higher than a 32x32 matrix array probe. A two-row unfocused 1.75D array has been used in [2] to calculate the elevational position of scatterers, in this study, a 1.75D array with four parallel rows of elements was used to increase the volume coverage without the need of mechanically moving the probe three times, together with the concept of projection SRUS using each row of elements.

This study investigated the feasibility of using a 1.75D array probe to perform multi-aperture projection SRUS to improve the imaging performance and the reliance on more sparsity of scatterers of the projection SRUS method. A microvessel network in simulation is used to show the proof-of-concept of MAP-SR, which compared the traditional 1D focused linear array, previously proposed 1D unfocused linear array and 2D matrix array results with different scatter concentrations, followed by experimental *in vitro* and *ex vivo* results.

4.2 METHOD

4.2.1 Transducers

To evaluate the proposed MAP-SR, four probes of the same aperture size were investigated, including 1) a 2D matrix array probe; 2) an elevational unfocused 1.75D array; 3) an elevational unfocused 1D array; 4) an elevational focused 1D array. To investigate these four probes, a 2D matrix array aperture was used at first and then data from the other probes were synthesized using data from this 2D matrix array.

First of all, a 2D multiplexing matrix array probe (Vermon, Tours, France) with 1024 elements, a central frequency of 7.8MHz, and an aperture size of 9.6 mm x 10.2 mm, with four sub-apertures

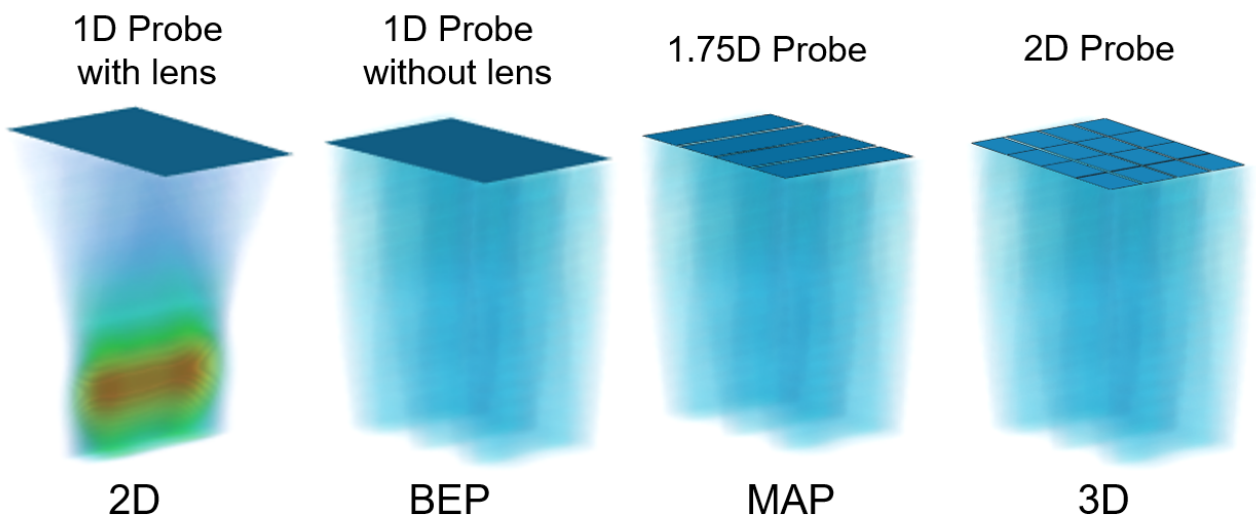


Figure 4.1: Transducer and four imaging schemes. The diagram of the 32*32 matrix array transducer is shown on the right. 2D imaging with an elevational focus synthesized by the central slice of the 3D beam formed volume (only receive focused); BEP imaging and MAP imaging through plane wave transmission and echoes received and summed along the elevational direction across the full aperture and one sub-aperture, respectively; 3D imaging through plane wave transmission and echo reception by all 32x32 transducer elements.

separated by three empty row lines as shown in Fig 4.1. Plane waves were transmitted using all the 32*32 elements simultaneously and the received radiofrequency (RF) data was beam formed using the 3D Delay and Sum (DAS) algorithm. Secondly, to simulate a 1.75D linear array with the same aperture size, the RF data acquired by the 2D array probe within each sub-aperture were summed along the elevational direction, effectively reducing the channel number from 32*32 to 32*4. Thirdly, the simulation of a 1D unfocused linear array, different from the 1.75D projection processing, RF data was summed along the whole elevation direction, resulting in a channel number of 32*1. Last, the simulation of a 1D focused linear array by taking the central slice beamformed image from the volumetric image, which approximation has been shown valid in the previous study. These four schemes were referred to as 3D, MAP (Multi-Aperture Projection), BEP (Broad Elevation Projection), and 2D (see Fig 4.1).

4.2.2 Simulation

The simulation was performed using BUFF [188] based on Field II [252] with probe parameters shown in Table 4.1. The flat aperture can be seen in Fig 4.1, where three dead rows exist

between each sub-aperture along the elevational direction for fabrication purposes. Microvessel networks following the fluid dynamics were generated for the simulation evaluation as shown in Fig 4.2. Simulations with low, medium (2*low) and high (2*medium) concentrations were repeated for comparison. 3dB noise was added to each group of simulations.

Table 4.1: Simulation Parameters

Parameter name	**Value**
Centre frequency	7.8 MHz
Transmit frequency	7.8 MHz
Speed of Sound	1540 m/s
Wavelength	197 μm
Element width	0.275 mm
Element kerf	0.025 mm
Element number	32*32 (1024)
Aperture size	9.6 (x) *10.2 (y) mm
Sampling frequency	31.24 MHz
Pulse	2-cycles, Hann-weighted
Apodization	Tukey(0.5)
Elevational Focus Depth	20 mm

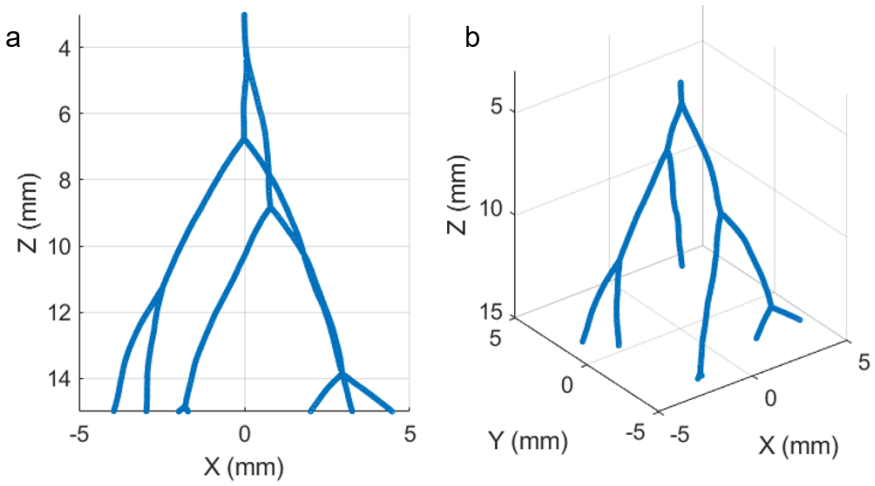


Figure 4.2: (a) Projection and (b) 3D view of the microvessel flow phantom placed around 10mm for simulation.

4.2.3 *In vitro* Experiments

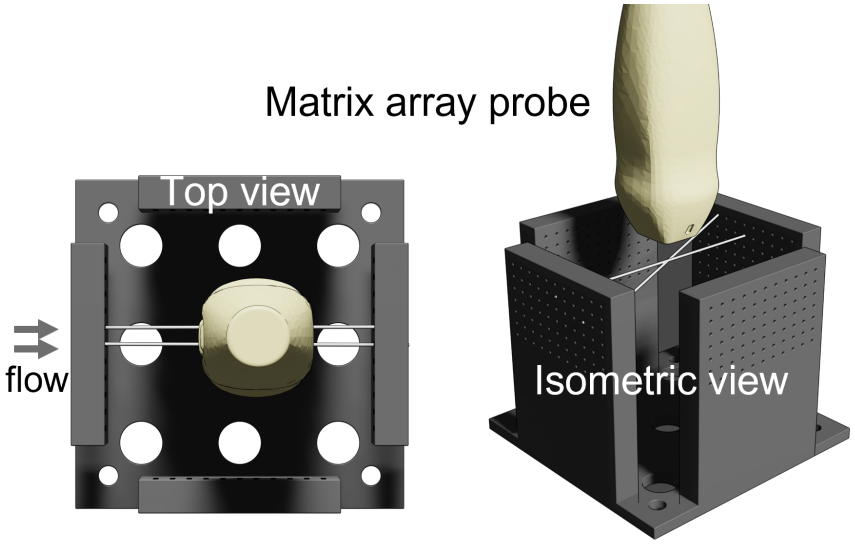


Figure 4.3: Top (a) and isometric (b) view of the experiment set-up. Microtubes were positioned in parallel with the help of a grid of holes on the sidewalls, with an acoustic absorbing pad at the bottom of the phantom.

The 7.8MHz multiplexed matrix probe was used in this study and was driven by a Vantage 256 system (Verasonics Inc., Kirkland, WA, USA). This probe has no physical elevational focus, providing the flexibility to simulate different types of arrays. Plane wave without steering was used to reduce the motion effect between transmissions and switching between different sub-apertures. Then each sub-aperture was used to receive the RF signal sequentially, meaning that each acquisition frame consists of four separate acquisitions.

A total number of 1000 Frames of images were acquired with a frame rate of 500 Hz. Two 200 μm $\pm$ 15 μm Hemophan cellulose tubes (Membrana, 3M, Wuppertal, Germany) with a wall thickness of 8 $\pm$ 1 μm were centered at around a depth of 16 mm in parallel, without crossing. A probe holder was 3D-printed to help align the probe with the phantom, as shown in Fig 4.3. Microbubbles(MBs) were made in-house according to the method stated in [270], and the MB solution was diluted 5000 times, resulting in a concentration of 10^6 per ml. Then the diluted suspension was injected into the tubes with a constant flow rate of 100 ul/min using a syringe pump (Harvard Apparatus, Holliston, MA, USA), which equals an average flow speed of 50 mm/s. Each volume of the frame is composed of 51 $\times$ 101 $\times$ 103 voxels with 100 μm in all three spatial directions.

4.2.4 *Ex vivo* Experiments

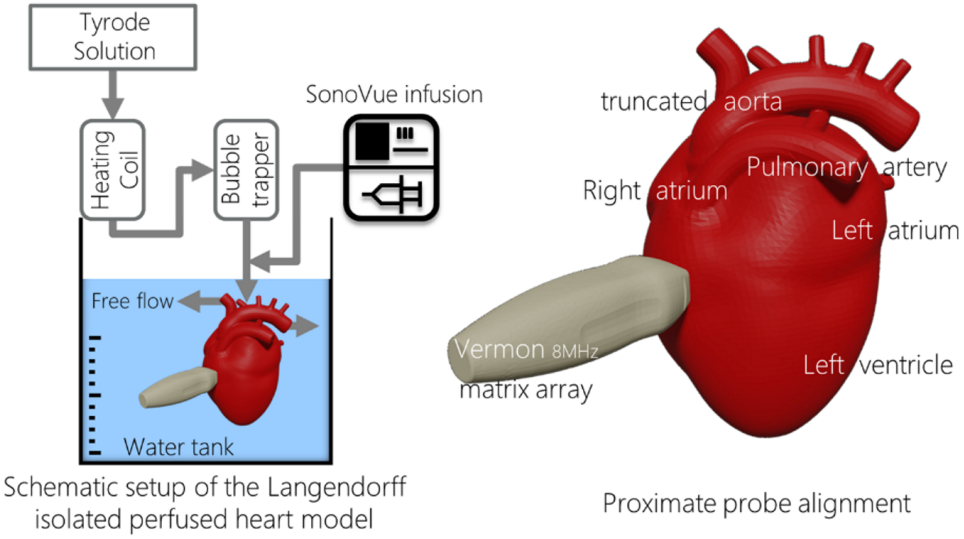


Figure 4.4: *Ex vivo* porcine heart experimental setup.

For the ex vivo experiment, a porcine heart was explanted from a white female pig (65-75 kg) aged 4-5 months, which was retrieved under anesthesia utilizing a human donor heart retrieval procedure [271]. The experiment was authorized by the Royal Veterinary College Animal and Ethical Review Board and carried out in compliance with ethical standards (European Commission 2010, Animal Welfare Act 2006, and Welfare for Farm Animals (England) Regulations 2007), as shown in Fig 4.4. MB was infused into the heart using a syringe pump (Harvard Apparatus, Holliston, MA, USA) at a rate of 5 ml/min. The same imaging sequence as the *in vitro* experiment was used to collect 2500 frames of images at a frame rate of 500 Hz.

4.2.5 Post-Processing

For the 3D reference, RF data from four sub-apertures were combined and beam formed to reconstruct a single 3D volumetric image using the 3D DAS algorithm. Then SVD filtering [256] was applied to the beam formed data to remove the strong reflections from the tube walls and tissue signals, where the SVD threshold was chosen by removing the first singular vector *in vitro*, and the frequency component below 10 Hz *ex vivo*, respectively [258]. The 2D dataset was

generated by taking the central slice out of the 3D beamformed volume and 2D processing was performed. The BEP dataset was generated by summing the RF data along one direction and 2D beamforming and processing were performed. The MAP dataset was generated by summing the RF data acquired separately along the same direction within each sub-aperture's area and 2D beamforming was performed, which is repeated four times using different sub-apertures. Then the same SVD filtering and threshold selection method was applied to generate the MB-only datasets. Before SR processing, a two-stage motion correction algorithm containing affine and non-rigid transform [239, 272, 273] was applied to *ex vivo* dataset to compensate for the diastole and contraction motion of the pig heart. For the SR processing, an initial threshold was applied to remove the noise and 2D cross-correlation and the Kalman filter was used for the localization and tracking for 2D, BEP, and MAP SR, and the corresponding 3D versions for 3DSR. To generate the image of the MAPSR result, tracked events from four sub-apertures were concatenated together to generate one localization and tracking image.

4.3 RESULTS

4.3.1 Simulation

Fig 4.5 a. shows the localization and tracking results of the microvessel phantom, with the white bar indicating 1mm. With a microvessel tree phantom (4.2), the conventional 2D SR can capture little segments of vessels that are close to the central imaging plane, whereas the BEP, MAP, and 3D methods can all capture out-of-plane vessel structures within a volume. Fig 4.5 b. shows the zoomed-in area labeled in the 3D localization images. In the upper row images, it is apparent that 3D successfully resolves the two close mainstream branches, while BEP and MAP are unable to do so due to the high microbubble concentration at the beginning. In the lower row images, when the tube branches are more well-distributed, MAP and 3D captured similar structures while BEP missed some segments. Fig 4.6 d. shows the line profile labeled in the 3D zoomed-in image above (Fig 4.6 c.). As the gold standard reference, 3DSR can successfully resolve two close microvessels with distances of no more than 0.1 mm at two different

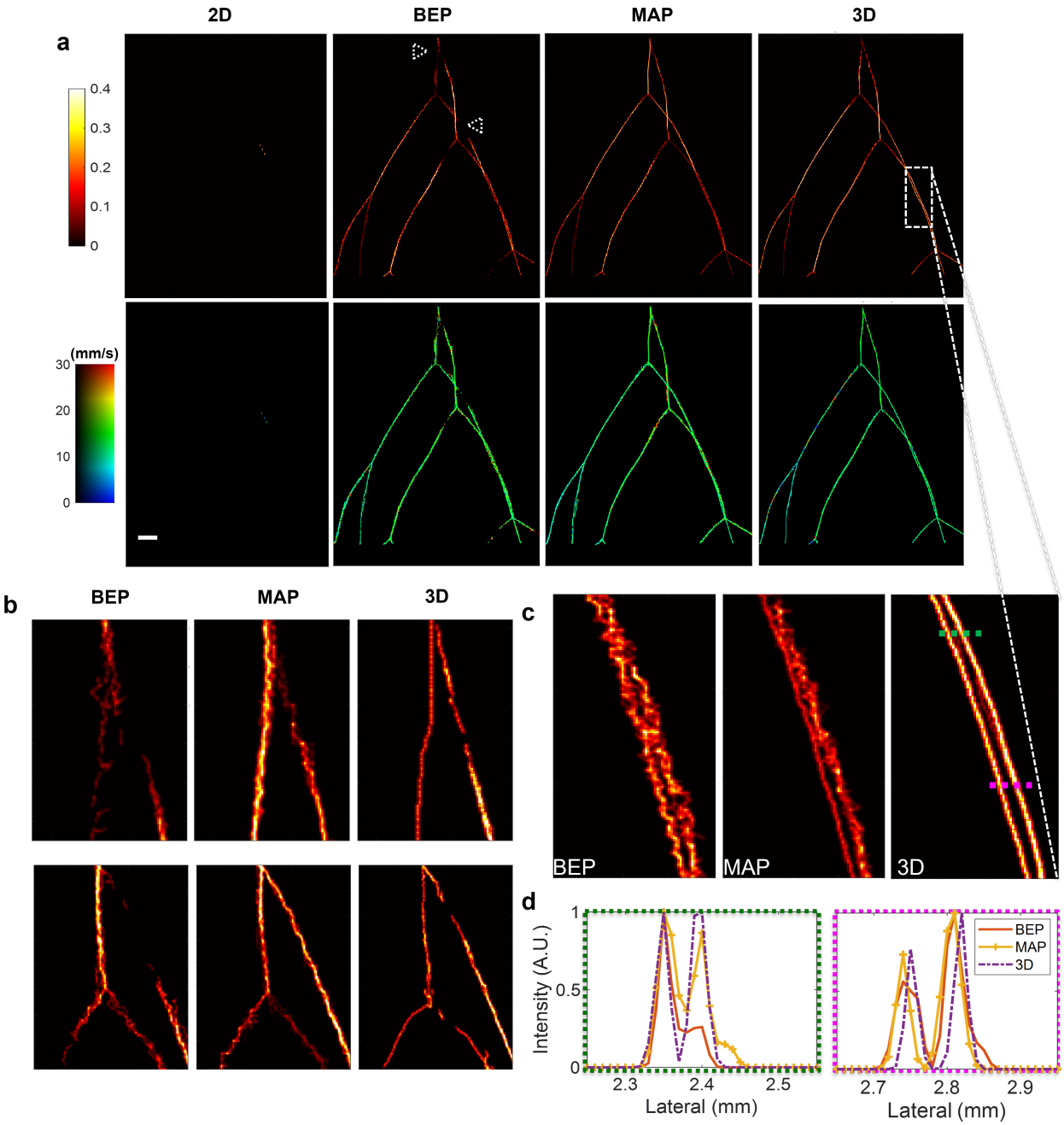


Figure 4.5: a. Simulation localization and tracking results using four different methods, MIP of 3D were plotted for the simplification of visualization. b. Zoomed in area localization images (upper rows: left triangle, lower row: right triangle)
. c. Line profile along the dashed lines in b. The white scale bar indicates a length of 1mm. In a., the conventional 2S SRUS results only show few scatterers and were not included in b. – d., whereas all the other three methods can reveal the structure of the 3D vessel network.

places. MAPSR can also achieve this at the cost of the imaging quality, as shown by the less smooth right tube compared to that of the 3D (right profile of Fig 4.6 d.). BEPSR was not able to resolve the two vessels when they were closer in the upper place, which is also verified by the left profile in Fig 4.6 d. Since standard 2DSR is unable to catch these segments, its

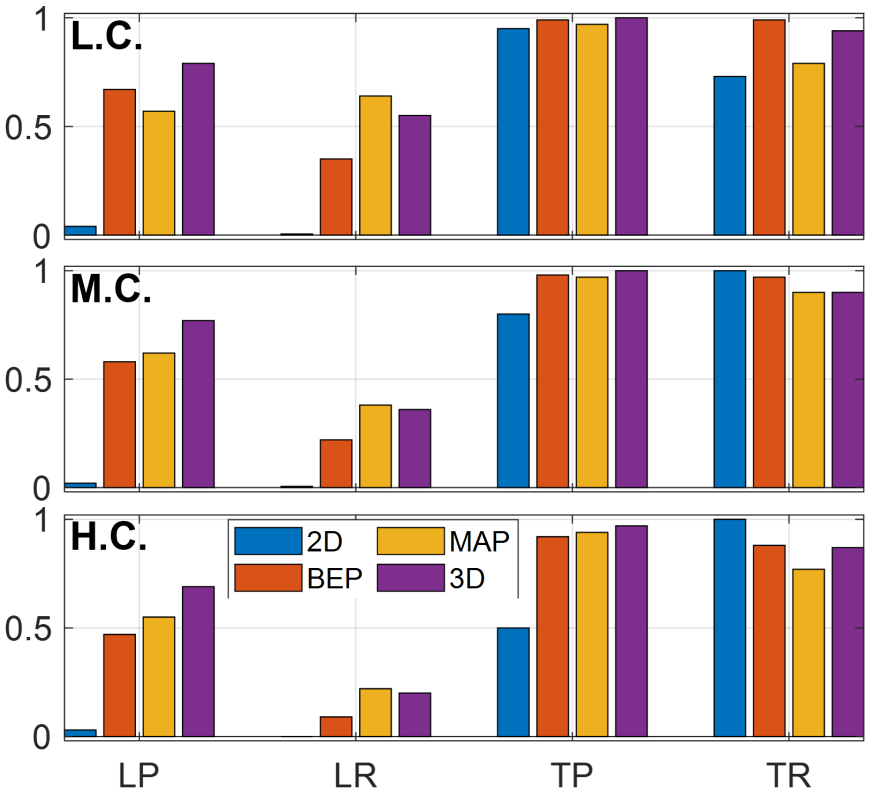


Figure 4.6: Evaluation results of localization and tracking performance in simulation with phantom centered at 10mm, with lower concentration (L.C.), medium concentration (M.C.), and higher concentration (H.C.). localization precision (LP), localization recall (LR), tracking precision (TP), and tracking recall(TR), with the searching radius equal to 1/4 wavelength.

results are not included and measured in 4.6 b.-d.

Fig 4.6 shows the evaluation results of the localization and tracking performance for each imaging method in simulation with three different concentrations. Regardless of concentration, 2D has the lowest localization precision (LP) out of these four imaging methods. By just removing the elevational focus, BEPSR can boost this number. At lower concentrations, BEPSR has higher LP than MAPSR, but as concentration increases, MAPSR has higher LP. The LP of 3D is the highest LP whatever the concentration. The localization recall (LR) of MAP remains the highest among the four imaging methods under different concentrations. MAPSR's LR is higher than that of the 3DSR maybe because the same 1/4 wavelength localization error tolerance is more stringent to the distance calculation in 3D coordinates in 3DSR, causing less true positive localization. The LR of BEP, MAP, and 3D all see a decreased trend as concentration increases. The LR of 2D is very close to zero regardless of the concentration, as it fails to detect and localize the signals distributed in the volume. The tracking precision (TP) of BEPSR,

MAPSR, and 3DSR is comparable and shows similar change as concentration increases. In all these concentration scenarios, the tracking recall (TR) of MAPSR is lower than BEPSR, this is likely caused by the existence of the dead rows within the multiplex matrix probe. Scatterers flowing into this region may not be able to be captured by MAPSR, causing the continuous track to lose certain segments within it, breaking into pieces of short tracks and reducing the tracking precision.

4.3.2 *In vitro* Experiments

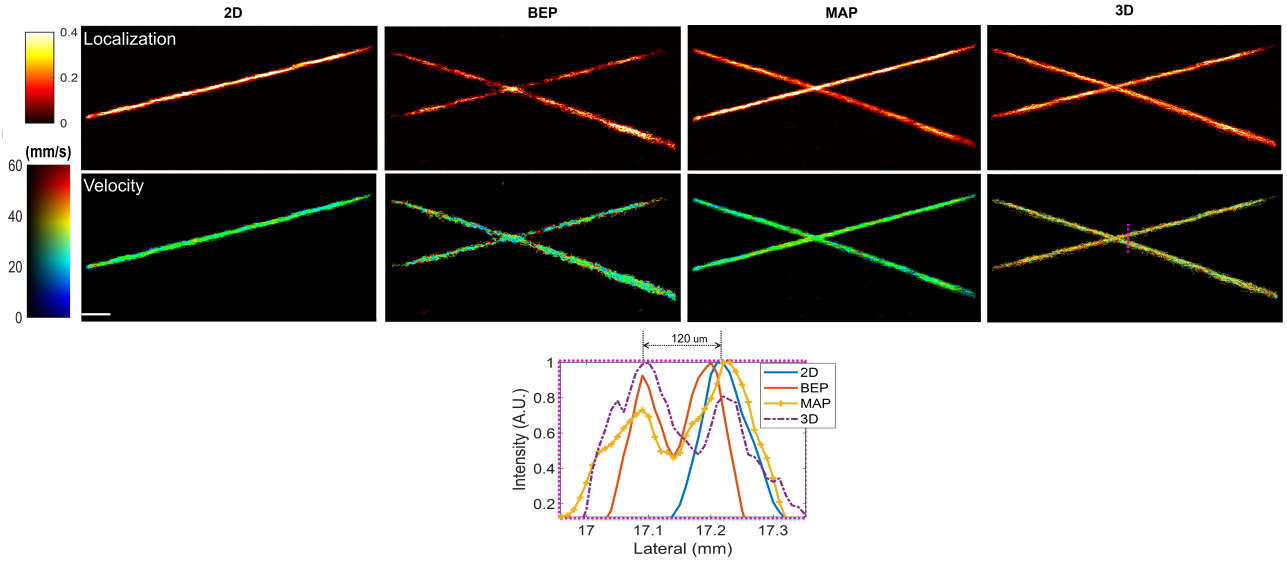


Figure 4.7: *In vitro* localization and tracking results using four different methods, MIP of 3D were plotted for visualization simplification. The bottom figure shows the line profile measured along the dashed line indicated in the 3D tracking image above.

Fig 4.7 shows the localization and tracking results of the cross-tube phantom. The line profile figure shows the intensity measurement result along the dashed line indicated in the 3D tracking image. With a 3D tube phantom containing one tube in approximately 2D and 3D space, respectively, the conventional 2D SR shows limited information capturing ability. It can only visualize one tube after manually selecting one single slice with the most microbubble signals out of the 3D volume. Whereas the BEP, MAP, and 3D SR methods can all capture these two tubes' information within the volume. This can also be confirmed by the line profile where the 2D intensity curve shows only one peak. In contrast, all the other three methods resolve the profile from these two tubes near the crossing point, with a distance of 120 μm. And the tube

looks smoother and thinner from the left to the right, as more elevational apertures are used for imaging. The mean velocities for 2D, BEP, MAP, and 3D are 31.9, 39.7, 38.5, and 41.5 mm/s, respectively. BEPSR and MAPSR generate similar flow velocity as both tubes were placed in two parallel off-center imaging planes as much as possible, spanning little along the elevational direction. This is slightly smaller than the 3DSR results, as also shown by the reddish colors on the velocity map.

4.3.3 *Ex vivo* Experiments

Fig 4.8 a. shows the localization and tracking results of the porcine heart, the conventional 2D SR can only capture few vessel segments due to the complex 3D structure of the heart model, whereas the BEP, MAP, and 3D methods can capture more information within the same imaging volume. A large vessel is visible in the upper right corner of the localization images of both MAP and 3D, but BEP is unable to fully visualize it. This is probably because the high concentration of bubbles in this big vessel area increases the overlapping signals along the projection direction and leads to more rejection of localization events. Fig 4.8 b. shows the zoomed-in images of the patches chosen above. Vessel details are gradually enriched from the left to the right. The 2D results provide limited vessel information in both places. It is noteworthy that BEP, MAP, and 3D have comparable tracking abilities regarding the velocity change caused by the split and convergence of this large vessel. As indicated by the upper right triangle, the two vessel branches exhibit a red-toned color, suggesting an increase in blood velocity after vessel splitting. A similar phenomenon can also be observed in the other places indicated by the small triangles on the BEP tracking results. The mean velocity for 2D, BEP, MAP, and 3D was 74.9, 59.3, 83.3 and 86.1 mm/s.

4.4 DISCUSSION

SRUS/ULM with volumetric information is valuable but existing techniques using matrix array transducers face significant challenges in both the matrix array fabrication complexity and

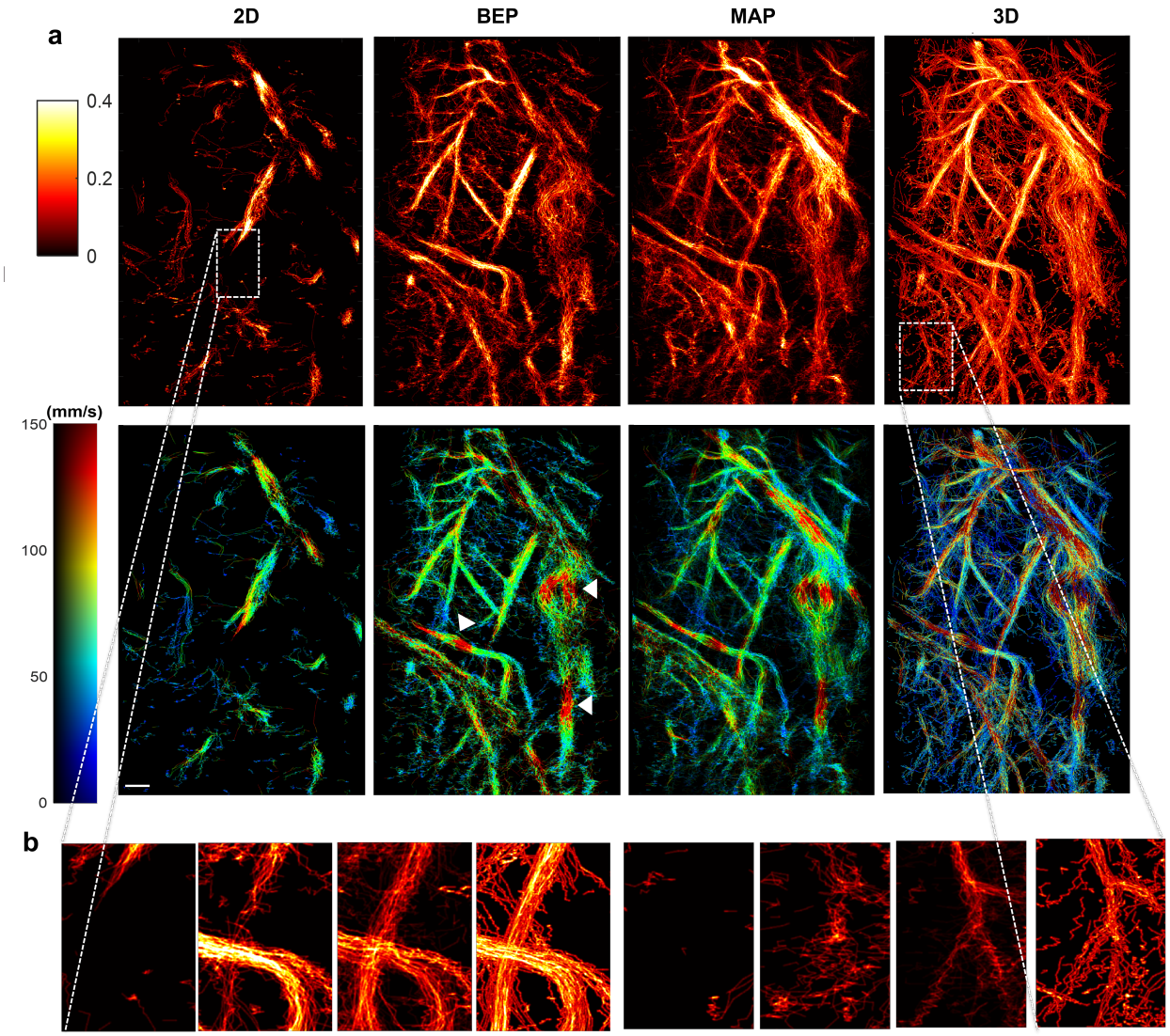


Figure 4.8: a. *Ex vivo* localization and tracking results using four different methods, MIP of 3D were plotted for visualization simplification. The scale bar indicates a length of 1mm. b. Zoomed in regions of 2D, BEPSR, MAPSR, and the MIP of 3D SR results, respectively, from left to right.

capability in data transfer and processing. Inspired by clinical X-ray radiography, in this proof-of-concept study, we have demonstrated in both simulation and experiments that with only few times higher numbers of channels and computational cost, MAP-SR using a 1.75D array and performing the BEP SRUS using four rows of elements in parallel can generate the projection SR images with higher imaging quality and higher tolerance of scatter concentration. The zoomed-in image and the profile image in Fig 4.5 show that when two vessels are separate in space but close to each other after projecting to the conventional XZ imaging plane, without a sparse concentration, BEPSR fails to resolve them in some places, while MAPSR's performance

is comparable to that of 3D.

Both the TP ($Precision = \frac{TruePositive}{TruePositive+FalsePositive}$) and TR ($Recall = \frac{TruePositive}{TruePositive+FalseNegative}$) for the 2DSR results are volatile as the tracking results were evaluated using only few correctly localized scatterers. This low number of true positive localization events will also affect the tracking performance. Because the tracking algorithm incorporating the graph-based assignment method only has few tracking pairs to enumerate and minimize the total cost, it thus cannot achieve optimal performance. The TR for BEPSR is higher than MAPSR, this is likely caused by the existence of the dead rows within the multiplex matrix probe. However, it is worth mentioning that this is not inherited from the method proposed. The dead row effect can be removed by using an actual 1.75D array that doesn't have any large dead row zones.

It is worth noting that the 2DSR image in Fig 4.7 was generated using a slice of the 3D beamformed volumes that corresponded to one tube's position, rather than the central slice of the volumes that contain zero localized scatterers and generated one black image. This emphasizes the benefit of both BEP and MAP SR methods in improving the dependence on the alignment of the conventional 1D probe's imaging plane with the targeting tissue slice for clinical research that needs repeatability. Compared to the BEPSR image, the MAPSR image looks smoother and more continuous as the BEP method projects more noise into one image, where the noise was not perfectly incoherent due to the bandwidth limitation, in addition to the increased cross-talk noise of the matrix probe. The mean velocity of BEP and MAP different from that of the 3D also indicate that both the projection SR methods will underestimate the velocity. But it is also possible to infer the third-dimensional velocity information in 2D imaging and correct the underestimation [262]. Further study can also be investigated using this method to correct velocity for the proposed projection SR methods.

In Fig 4.8, same as the processing in simulation results, the 2DSR image was generated using the central slice of the 3D volumes. The phenomenon that only segments of porcine vessels are visualized in 2DSR also helps emphasize the challenges of using a conventional 1D probe to do SRUS research that needs repeatability, e.g. cardiac research where the microvasculature is comparably complex. Compared to BEPSR, another benefit of MAPSR is that the underestimation of flow velocity (83.3 mm/s) is smaller as the projection volume decreases, which is

Table 4.2: Computational Cost

	2D/BEP	**MAP**	**3D**
Image Size	281*121*2500	281*121*2500*4	281*121*123*2500
Data Size	0.81GB	3.26 GB	83.64GB
Saving Time	4s	16s	55min
SVD Processing	0.08h	0.37h	4.21h
Motion correction	0.84h	3.44h	32.61 h

quite close to the 3D tracking results (86.1 mm/s).

By comparison, 3DSR has the best imaging quality, but at a significant fabrication and computational cost that hinders its clinical translations. Table 4.2 shows the comparison of the computational cost of the different imaging methods when processing one *ex vivo* dataset. Due to the large size of the 3D data, both the SVD processing and motion correction have to run on a CPU (Intel(R) Xeon(R) CPU E5-2630 v3 @ 2.40GHz) and 128GB RAM. Although an advanced CPU can help accelerate the 3D processing, it can also make 2D processing faster, which already takes hundreds fewer times to save data, and dozens fewer times of memory for each step of processing before SR processing, which has the potential to make real-time SR application possible.

It is also worth mentioning that the 1.75D array used in this paper has four rows due to practical reasons. The benefit of this technique can also be brought by using just a two-row 1.75D array, further reducing the fabrication cost. Besides, the fitting method used in [2] can also be conducted to correct the velocity and generate a higher-quality projection image with the actual velocity map.

4.5 CONCLUSION

In summary, this study demonstrates that MAP-SR can generate super-resolution microscopy images that capture information on micro-vasculature within a volume using a 1.75D array probe without an elevational focus. The technique requires hardware and computing resources that are many folds less than the full 3D SRUS. The localization and tracking performance can be improved with slightly higher costs than the previously proposed BEPSR method which has

a similar cost as the classical 2D imaging technique.

Acknowledgment

We would like to thank Biao Huang for his help with the porcine data acquisitions.

Statement of Contributions

Mengxing and Bingxue contributed to the concept of this study. Marcelo helped with the field II simulation scripts, Matthieu helped with the Verasonics scripts and the experimental setup, Kai helped with the in vivo experiments, and Jipeng Yan helped with the tracking algorithms. Bingxue finished the simulation, in vitro and in vivo experiments, and the data analysis.

Chapter 5

SRUS using Monodispersed Microbubbles

5.1 Introduction

Microbubbles have been widely used in SRUS research thanks to their strong scattering properties and biocompatibility. The backscattered signals from microbubbles are much higher than that of red blood cells and individual microbubbles are detectable with ultrasound. In SRUS imaging, sparse distribution of the bubbles is preferred as individual microbubbles need to be detected, localized, and tracked over time. Therefore a long acquisition time is needed to accumulate the localisations and tracks to generate SR images revealing the complex microvessel structure [19].

To address this problem of long acquisition time, a sparsity-based algorithm [21] that is different from the conventional localization-tracking pair processing method was developed. This method exploits the statistically independent signals within a sparse microvasculature and can generate an SR image with only tens of milliseconds of acquisition. However, this method can only generate localization images without any flow information.

Research has also been conducted to improve the separation of contrast agents at higher concentrations, thus reducing the acquisition time. For example, an advanced filtering method was

proposed to filter MB with different velocities according to their spatiotemporal characteristics [20].

Deep-learning tools were also introduced to solve this problem in the image domain. For example, a convolutional neural network (CNN) was used to perform localization processing in higher concentrations [22]. This model can deduct the image feature of overlapped radiofrequency signals coming from close microbubbles. However, the model is not robust enough to perform better than the traditional localization method in low-density scenarios. Using a different strategy, another CNN was trained based on an optical mouse brain image [274]. It is demonstrated to recover the microvasculature at a higher resolution than the conventional localisation-tracking pair method in the high-density scenario. But reference images for training are not always available *in vivo* and both methods using CNN models cannot generate flow information. Therefore, how to work with data of different bubble concentrations, while still being able to generate flow velocity information is still being widely investigated.

Therefore, how to reduce the dependency of SRUS on sparsity, while still being accessible to the velocity information is still being widely investigated. All the research mentioned above is aimed at improving the separation of overlapped contrast agent signals during the post-processing step. In contrast, this study aims to investigate if microbubble signals can be better separated during the imaging stage by introducing monodispersed microbubbles.

Currently, commercialized ultrasound microbubbles are produced with a polydispersed size distribution [180]. However, monodispersed microbubbles with more uniform size distribution have been proven to have higher sensitivity than polydispersed ones *in vitro* [192] and *in vivo* [193], which were analyzed based on the average scattering power per bubble. One of the reasons is that the microbubble's resonant frequency depends on its diameter, the imaging system having a limited bandwidth is only sensitive to a limited range of bubble size.

It has been demonstrated that using a combined imaging strategy (switching between Bmode and contrast mode) within one acquisition may increase the localization efficiency and thus reduce the acquisition time needed to saturate the vasculature in SRUS images [275]. Similarly, it was also demonstrated that with the same concentration, monodispersed microbubbles with larger diameters can increase the SR imaging sensitivity [194]. However, both studies lacked

simulation validations and only conducted experiments using one US imaging system operating at one center frequency. Therefore, this chapter aims to use two different probes operating at different frequencies *in silico* and *in vitro* to investigate two hypotheses:

1. with control of the transmit pulse and sequence parameters, can different bubbles be selectively imaged according to their different sizes in experiments?

2. can the detection sensitivity be improved by utilizing the more uniformed mono-dispersed microbubbles in SRUS where spatially independent microbubbles need to be localized and tracked?

It is worth noting that there are different methods to produce monodispersed microbubbles. For example, researchers made monodispersed microbubbles using SonoVue/Lumason (Bracco Imaging S.p.A., Colleretto Giacosa, Italy) and then sorted the bubbles according to their sizes [192, 193]. Definity (Lantheus Medical Imaging, North Billerica, MA) was used directly in [275]. Homemade and size-selected monodispersed microbubbles were used to compare with commercial polydispersed microbubbles including Definity and Optison (GE Healthcare Bio-Sciences, Pittsburgh, PA) in [194]. In this study, size-sorted monodispersed and polydispersed microbubbles were provided by our industry partner.

5.2 Method

5.2.1 Simulation

To start the investigation, simulations were done in BUbble Flow Field (BUFF) [188] which incorporates the Marmottant lipid-coated microbubble model into the Field II simulation framework [188]. Simulations of a single bubble's response with different sizes are done and a tube phantom with different flowing microbubbles is conducted to perform SRUS imaging.

Bubble Response

To investigate the first hypothesis that different-sized microbubbles can be selectively excited using different pulses, bubble responses with different simulation parameters were first generated. Due to the limited choice of practically available monodispersed MBs, the largest and smallest sizes are 5.9 μm and 3.5 μm respectively.

Tube Phantom in Simulation and Evaluation

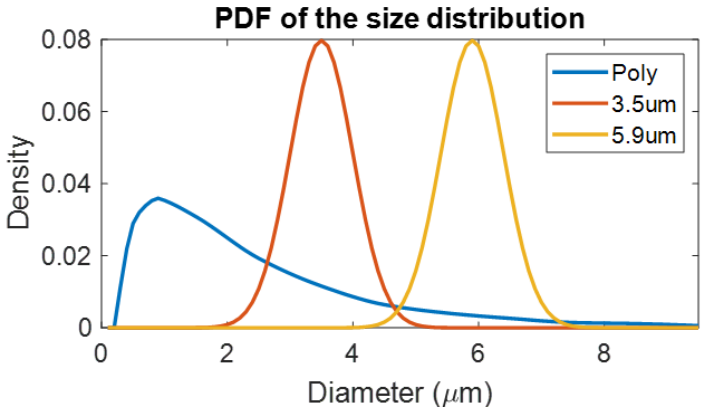


Figure 5.1: Size distributions of different microbubbles populations.

To investigate the second hypothesis that monodispersed microbubbles can help improve the detection sensitivity of SRUS imaging, two tubes crossed at the center were filled with flowing scatters. Scatterers are generated following the size distribution of different microbubbles according to the data provided by our industry collaborator, as shown in Fig 5.1. Both 2D imaging and 3D imaging simulation were tried using 1D array probes and a 2D array probe, respectively.

Polydispser MB and monodispersed MB with a mean size of 3.5μm and 5.9μm were used for tube phantom simulation. Considering their resonant frequencies, and the limited physical equipment available to us, one linear array probe L12-3v and one matrix probe Matrix1024-8MHz were chosen for simulation, which can be later compared to experiments. BMode imaging simulation was performed. Simulation parameters are shown in Table 5.1. Plane waves without any steering were used for the simulations. 3dB noise was added to each dataset. Delay and Sum (DAS) algorithm was used for image reconstruction. Once beamforming was done,

Table 5.1: Simulation parameters for tube phantom simulation.

Parameters	1D probe	2D Probe
Probe Name	L12-3v	Matrix1024
Bandwidth	[4.04, 11.04]MHz	[5.47, 10.15]MHz
f_0	3.7 MHz	7.8 MHz
Pulse Cycle	2	2
Receive Apodization	tukey(0.5)	None
MI	0.05	0.05
Frame Rate	500	500
Total frame	2000	2000
Max Velocity	25mm/s	25mm/s
Focusing/Steering	None	None

localization[276] and tracking [261] were performed, followed by the evaluation of the performance. 3.7 MHz was chosen as the transmit frequency when using the L12-3v probe as a compromise between the resonant frequency of the 3.5μm bubbles and the bandwidth limit of this probe.

For the post-processing, cross-correlation [276] was used for localization. First, Field II [189] was used to simulate a single scatter at (x =0, y =0, z = 20 mm) to create the reference point spread function (PSF) of the L12-3v probe and 7.8 MHz multiplexed matrix probe (Vermon, France). A noise threshold of 0.1 was chosen empirically with the image being normalized and its intensity ranges from 0 to 1. NCC between the PSF template and the images was carried out following intensity thresholding. Next, local maxima were identified on the correlation coefficient-thresholded images (0.3 was selected empirically). To save computational expenses, a 5*5*5 patch surrounding each maximum was extracted from the low-resolution correlation coefficient map. Spline interpolation was then used, and the maximum value inside each patch was localized. The same noise threshold and correlation coefficient threshold were applied across simulations using different monodispersed microbubbles.

Table 5.2: Post-processing parameters for tube phantom simulations.

Steps	Parameters	Number
localization	noise threshold	0.1 (image intensity between [0,1])
	correlation threshold	0.4
tracking	minimum length (frames)	2
evaluation	localization error tolerance	$\lambda/4$

Kalman filter was used for tracking processing [261], and two types of tracking algorithms were used, incorporating the power feature of the bubbles in the Kalman filter or not. The hypothesis is that more uniformed PSFs would have more similar power intensities among the consecutive frames, hence may improve the pairing performance. Without the power feature, the Kalman filter will only link bubbles according to their position information. Therefore, the power feature was included or not to see how the monodispersed microbubble's higher uniformity could affect the tracking performance in SRUS. The simulation and post-processing parameters can be seen in Table 5.2.

The evaluation was also done using the BUFF simulator, using metrics defined in [188], the localization error tolerance level defined as $\lambda/4$. Apart from the metric mentioned in Chapter 3.2.3, there are two additional two metrics used in this chapter: Localization error and Tracking error.

Localization error, which is the root mean square error (RMSE) of all the true positive localizations (N_{TP}), describes the average distance between the correctly localized events (TP) with the ground truth position (GT).

$$RMSE = \frac{\sum_{i \in TP} distance(TP_i, GT_i)}{N_{TP}} \tag{5.2.1}$$

Tracking error, this is calculated via the correct pair distance as bubbles that travel further away between two consecutive frames are harder to track, and achieving this indicates a better tracking performance. Therefore, a weighted Jaccard Index metric was introduced with the parameters being weighted by the distance of each pair.

$$\begin{aligned} J &= \frac{TP_d}{TP_d + FP_d + FN_d}, where \\ TP_d &= \sum_{i \in TP} distance(pair_i) \\ FP_d &= \sum_{i \in FP} distance(pair_i) \\ FN_d &= \sum_{i \in FN} distance(pair_i) \end{aligned} \tag{5.2.2}$$

A variation of this metric $J^* = 2J - 1$ was used to remap the range of this metric from $[0, 1]$ to $[-1, 1]$, where a negative value means the tracked pairs were mostly incorrect.

5.2.2 *In Vitro* Experiment

Experiments were also conducted to investigate if controlling the transmit pulse parameters, together with the spectral filtering techniques can selectively excite a certain size of bubbles. The hypothesis is that by selecting bubbles selectively, a higher concentration of bubbles with different size distributions can be separated within the field of view. In detail, with the help of the ultrafast ultrasound technique, pulse sequences can be switched quickly. Therefore, signals from different sizes of bubbles that are only sensitive to a specific pulse/sequence can be acquired within the same acquisition time window. This will help reduce the total acquisition time needed to generate a saturated SRUS image.

Table 5.3: Monodispersed microbubble parameters for *in vitro* experiment.

Parameters	Bubble 1	Bubble 2
Bubble Size /μm	3.5	5.9
Resonant frequency / MHz	3.2067	1.5915

Table 5.4: Physical probes parameters for *in vitro* experiment.

Parameters	Probe 1	Probe 2
Probe Name	L12-3v	P4-2
Bandwidth (6dB) /MHz	[4.03, 11.05]	[1.71, 3.73]
F0 /MHz	7.54	2.72
Tx /MHz	3.68	1.95

Similar to the tube phantom *in simulation*, a cross-tube phantom was also used *in vitro* filled with different-sized microbubbles with the maximum and minimum diameters shown in Table 5.3. Two ultrasound transducer probes were chosen to try to accommodate their resonant frequency bandwidths, see Table 5.4.

The P4-2 probe was used to transmit at MI = 0.1 and 1.95 MHz, which is the resonant frequency of the 3.5μm-sized bubble. Two tubes were filled with different-sized bubbles that had a mean diameter of 3.5μm and 5.9μm, respectively. Once a set of the acquisition was done, the tube was

flushed with water and filled with the other size of the bubble. This exchange aims to exclude the variation that may be brought by the flow resistance of the tubes themselves. Apart from B Mode imaging, PI and AM imaging were also performed.

The L12-3v probe was used to transmit at MI = 0.1 and 3.68 MHz, which is close to the resonant frequency of the 5.9μm-sized bubble. Bmode, PI, and AM sequences were performed. Besides, 5 MHz was also transmitted to see how different-sized bubbles react to a transmission frequency that is not close to their resonant frequencies. Thanks to the wider bandwidth of this probe, PI and AM sequences can also be performed at 5MHz to receive harmonics.

5.3 Result

5.3.1 Simulation

Bubble Response

Table 5.5: Bubble response simulation parameters with different **pulse cycles**.

Diameter/μm	Pulse Cycle	F0/MHz	MI	Bandwidth/MHz
5.9	2 4 6 8	1.59	0.055	5

Table 5.6: Bubble response simulation parameters with different **MIs and** f_0

Diameter/μm	Pulse Cycle	F0/MHz	MI	Bandwidth/MHz
5.9 4.8 3.5	2, 8	1.59, 3.21	0.0055, 0.055	5

Fig 5.2 shows a single 5.9μm bubble's response to different pulses with parameters in Table 5.5. Increasing the number of cycles can narrow down a microbubble's response spectrum around the resonant frequency but with little difference in harmonic components' magnitude.

Fig 5.3 and Fig 5.4 shows bubbles' response to different pulse cycles, excitation frequencies, and MIs with parameters in Table 5.6. It is observed that the oscillation behaviour of the bubbles and their harmonic generation are highly complex. As their oscillation includes different

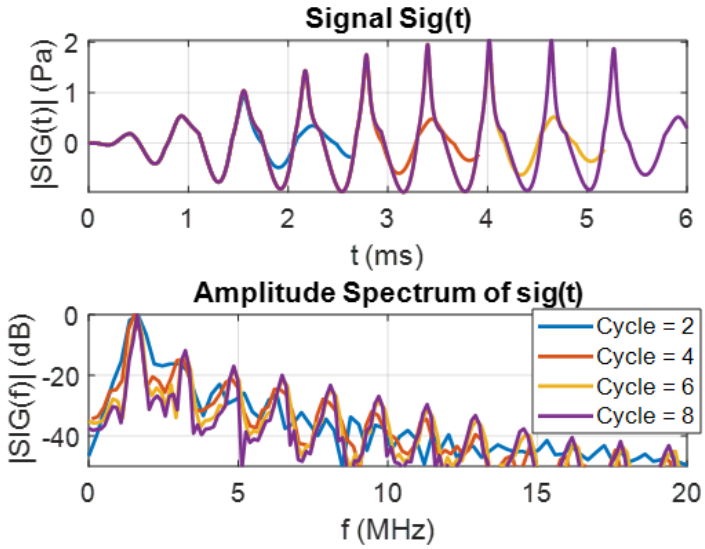


Figure 5.2: Bubble response to different pulse lengths

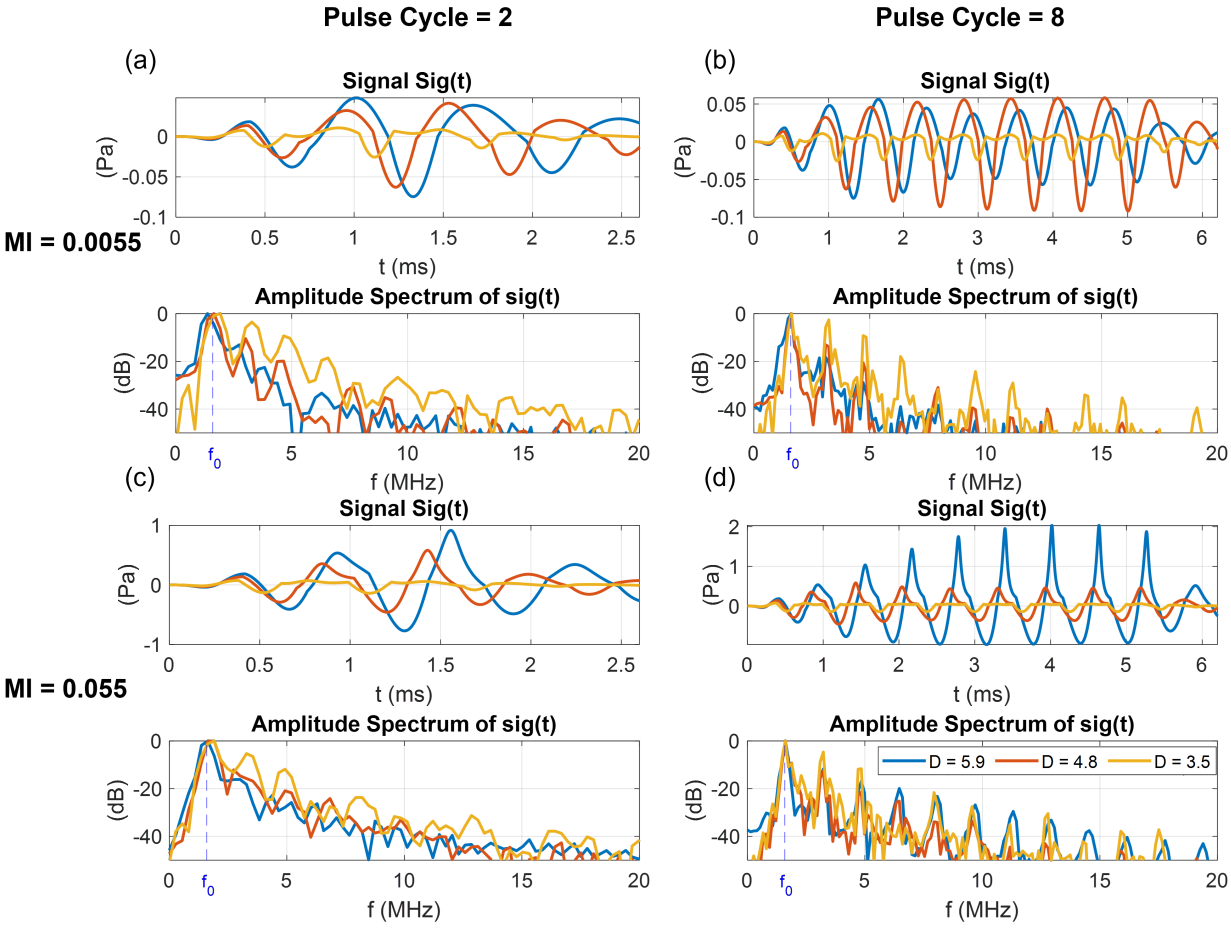


Figure 5.3: Bubble response to (a) (c) pulse cycle = 2 and (b) (d) (f) pulse cycle = 8 when MI = 0.005 (a-b) and 0.05(c-d), respectively. f_0 = 1.59MHz, the resonant frequency of the 5.9μm-sized bubble

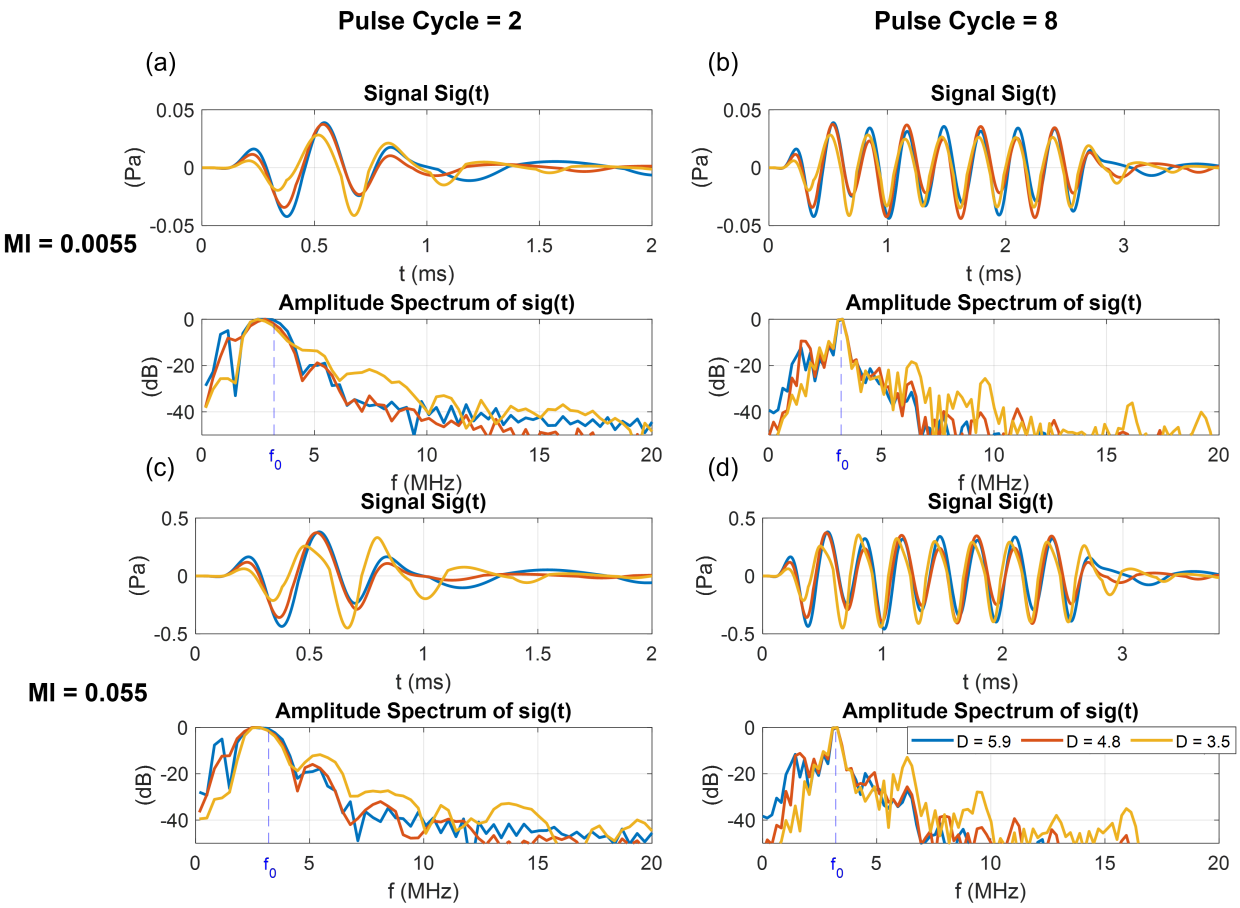


Figure 5.4: Bubble response to (a) (c) pulse cycle = 2 and (b) (d) (f) pulse cycle = 8 when MI = 0.005 (a-b) and 0.05 (c-d), respectively. f_0 = 3.21MHz, the resonant frequency of the 3.5μm-sized bubble

regimes including elastic oscillation, shell buckling and shell rupture, and where these regimes are and where the bubble lies in these buckling-elastic-rupture regimes all impact the acoustic signals we observe. The initial size of the bubble, and the ultrasound pulse parameters also impact in which regime(s) the bubble oscillates.

It shows that when the pulse cycle is short at 2, the 5.9μm-sized bubble at resonance generates stronger responses at both MIs, which mainly consist of the fundamental frequency component. This is likely because, at lower incident pressure, the resonant microbubbles undergo largely symmetric expansion and compression, and emit most signals with the same frequency as the incident pulse [277]. Whereas the 3.5μm-sized bubble off-resonance oscillates more asymmetrically and generates more nonlinear responses containing a higher percentage of harmonics. This may be due to the stronger nonlinear behaviour of such bubbles as simulated by the bubble dynamics model, the Marmottant model used for this simulation, where thresholds for

shell buckling and rupture depend on bubble size and pressure. When the larger bubble is at resonance, it is likely the oscillation is mostly in the "elastic" regime of the oscillation, which is more linear, while the off-resonance bubbles may be more in the "shell buckling" regime, which gives strong nonlinear harmonics relative to the fundamental signals.

The spectrum around the fundamental frequency narrows down as expected since a longer pulse has a narrower bandwidth. Under a higher MI and longer pulse length, larger bubbles ($5.9\mu m$) at resonance generate significantly stronger responses than bubbles that are off-resonance, and the proportion of the higher harmonics to the fundamental component is similar to other bubbles. This may be because, at a higher pressure and pulse length, the amplitude of the bubble oscillation increases and can go more into the nonlinear regime including both shell buckling and shell rupturing.

Fig 5.4 shows that larger bubbles generate stronger echoes than smaller bubbles when they are at resonance and off-resonance, respectively. While smaller-sized bubbles at resonance can generate a similar intensity of echoes as the larger bubbles that are off-resonance, regardless of the pulse cycle. It is also shown that the resonant $3.5\mu m$-sized bubble generates responses consisting of more harmonic components for both pulse lengths.

Tube Phantom in Simulation

L12-3v Probe

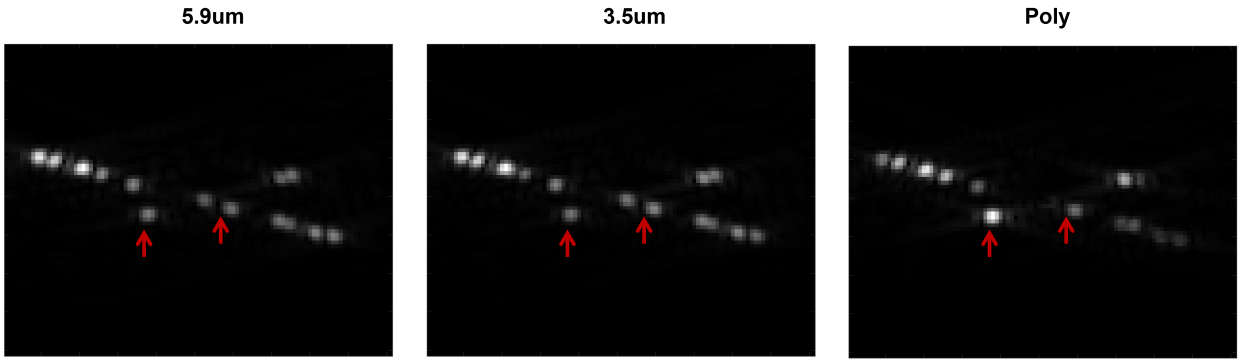


Figure 5.5: Single frame B-mode images with pulse cycle = 2 *in simulation*

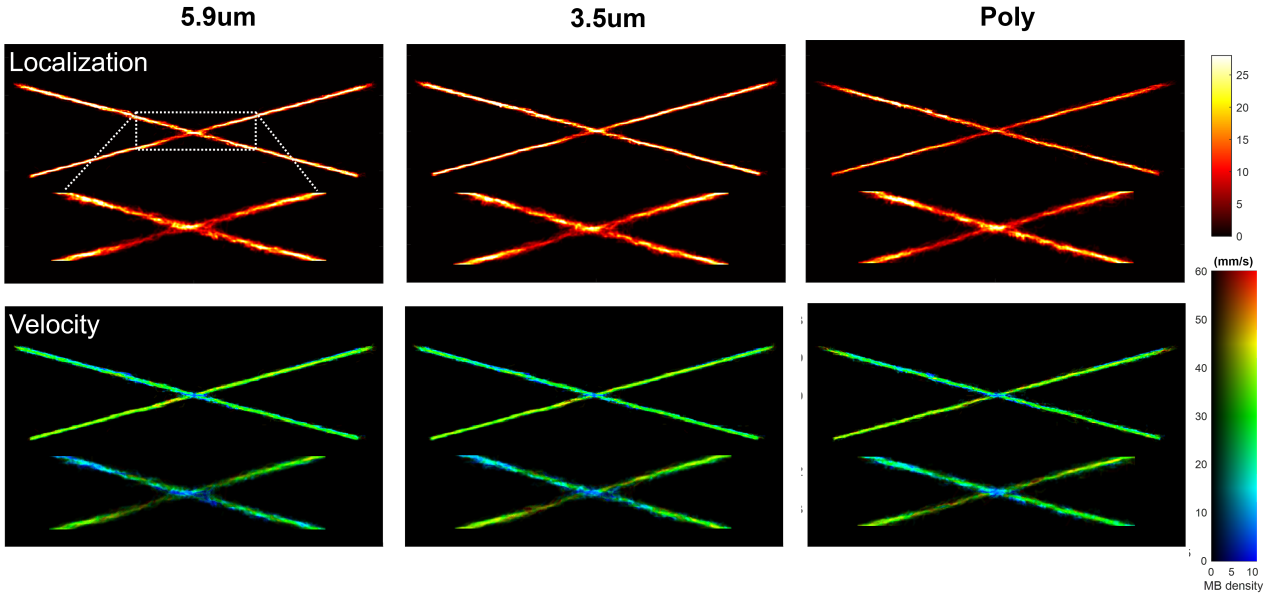


Figure 5.6: Localization and tracking results *in simulation* using L12-3v.

Table 5.7: Evaluation results for 2D tube phantom simulation using L12-3v.

Concentration	Step	Metrics	Tracking with Power			Tracking without Power		
			5.9μm	3.5μm	Poly	5.9μm	3.5μm	Poly
High	localization	Precision	0.98	0.98	0.98			
		Recall	0.59	0.59	**0.53**			
		Error (μm)	58.22	58.25	**54.13**	58.26	58.23	**54.14**
	tracking	Precision	0.91	0.92	0.93	0.91	0.92	0.93
		Recall	0.95	0.95	0.95	0.95	0.95	0.95
		Score	0.67	0.68	**0.72**	0.66	0.67	**0.71**
Low	localization	Precision	0.98	0.99	0.99			
		Recall	0.75	0.73	**0.71**			
		Error (μm)	75.44	48.55	**43.30**	75.42	48.55	**43.32**
	tracking	Precision	0.94	0.94	0.95	0.94	0.94	0.95
		Recall	0.95	0.96	0.96	0.94	0.96	0.95
		Score	0.73	0.76	**0.78**	0.72	0.76	**0.77**

Fig 5.5 shows the single frame Bmode image from three simulations using two sizes of monodispersed microbubbles and polydispersed microbubbles. The red arrow indicates the PSF variations among them, especially the similar-sized PSFs in the left two images, and the brighter and disappeared bubbles that appeared in the polydispersed dataset. The localization and tracking results can be seen in Fig 5.6. The zoomed-in image of the center crossing part is shown below each image.

The evaluation metrics are shown in Table 5.7 using metrics in equation 3.2.1 and 5.2.2. As the concentration decreased, the localization recall, localization error, tracking precision, and thus

the tracking score improved regardless of the size of the contrast agents. The polydispersed and larger MB has the lowest and highest localization recall, whatever the concentration is. This may be because the stronger response of the larger bubble increases the number of correctly localized events ($Recall = \frac{TruePositive}{TruePositive+FalseNegative}$). Whereas the darker bubble signals as shown in the single-frame image are less likely to be correctly localized, reducing the number of correctly localized events and thus the recall rate. The localization error of the larger MB dataset is the highest, this may be because the localization processing is performed using cross-correlation algorithms, where a linear scatterer's PSF was used as the template for the correlation performance. This may cause different levels of systematic shift during this localization process, and as the larger bubble has a larger PSF, this systematic shift is likely to be larger. The tracking performance of the polydispersed MB is the highest, which may be because the non-uniform PSFs help the graph-based tracking algorithm to differentiate and match these bubble pairs. Removing the power feature in the Kalman filter tracker has little negative impact on the tracking metrics.

Fig 5.7 shows the same frame of Bmode image as Fig 5.6 from three simulations when the pulse cycle is increased to 8, axial resolution decreased significantly. Due to the bad axial resolution, the super-resolution processing was not implemented as these bubbles are hard to isolate.

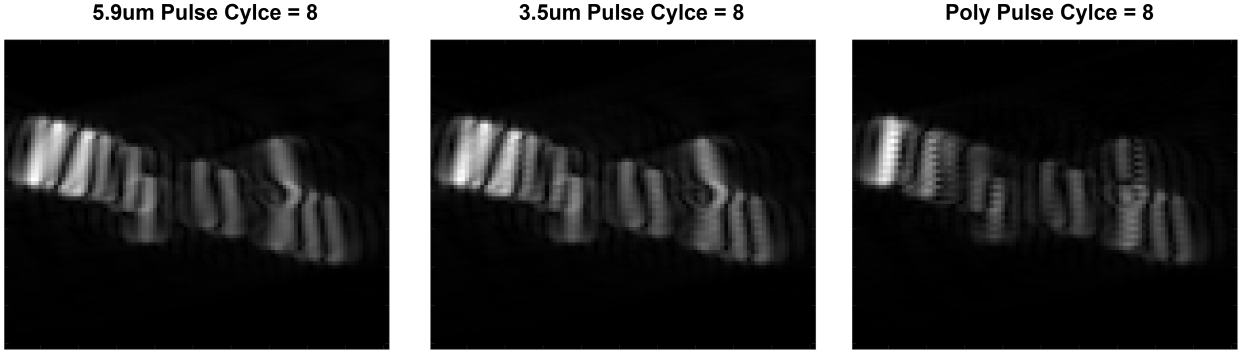


Figure 5.7: Single frame B-mode images with pulse cycle = 8 *in simulation*

Matrix Probe

Fig 5.8 shows the localization and tracking results using a 3D tube phantom. The zoomed-in image of the center crossing part is shown below each image. The evaluation metrics are shown

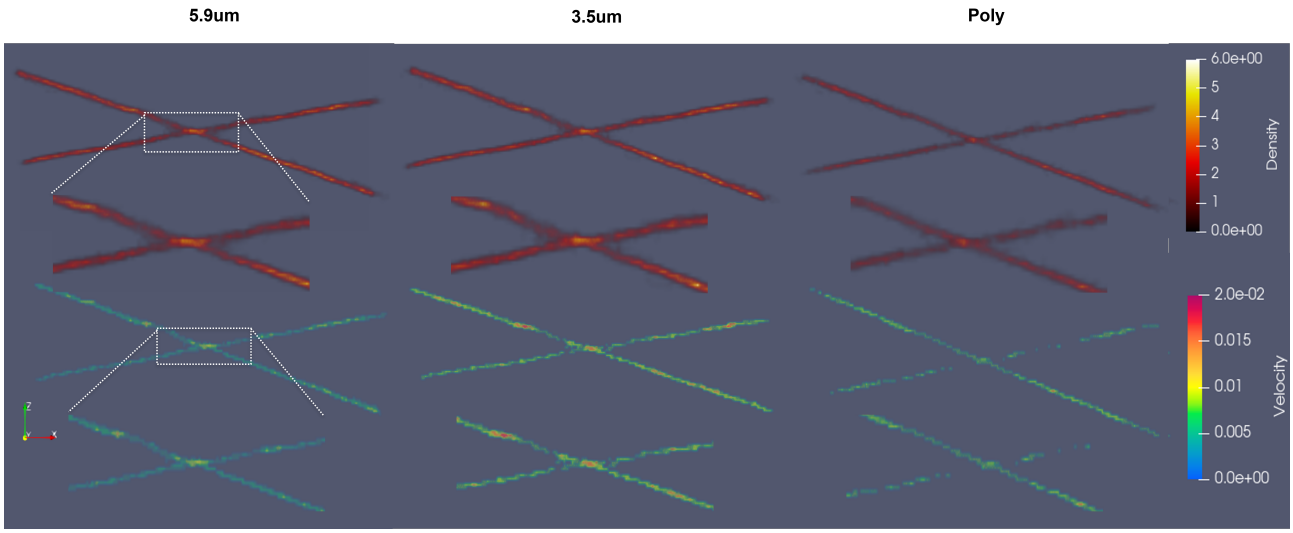


Figure 5.8: Localization and tracking results *in simulation* using Matrix probe.

Table 5.8: Evaluation results for 3D tube phantom simulation using Matrix1024-8MHz.

Concentration	Step	Metrics	Tracking with Power			Tracking without Power		
			5.9μm	3.5μm	Poly	5.9μm	3.5μm	Poly
High	localization	Precision	0.53	0.52	**0.63**			
		Recall	0.30	0.31	**0.24**			
		Error (μm)	27.27	27.40	26.28	41.90	38.01	
	tracking	Precision	0.98	0.98	0.98	0.98	0.98	0.98
		Recall	0.99	0.99	0.98	0.98	0.99	0.97
		Score	0.91	0.93	**0.90**	0.90	0.92	**0.89**
Low	localization	Precision	0.66	0.68	**0.73**			
		Recall	0.51	0.52	**0.43**			
		Error (μm)	23.26	23.24	22.92	33.88	33.51	31.48
	tracking	Precision	0.99	0.99	0.99	0.99	0.99	0.99
		Recall	0.99	0.99	0.99	0.99	0.98	0.98
		Score	0.95	0.94	**0.95**	**0.94**	0.93	**0.94**

in Table 5.8 using metrics in equation 3.2.1 and 5.2.2. Similar to the 2D results using the L12-3v probe, in the 3D simulation results using the matrix probe, polydispersed microbubbles have a lower localization recall rate while the smallest localization errors. The discontinuities in the lower right tracking images and the lower saturation of the localization image also correspond to the lower recall rate that may caused by less correctly localized events. The tracking scores are very close using three types of microbubbles, it seems that the polydispersed microbubble generates a higher tracking score at a lower concentration, and a lower tracking score at a higher concentration, but these numbers are very close. Removing the power feature in the Kalman tracker caused a slight decrease in the tracking score.

5.3.2 *In Vitro* Experiment

P4-2 Probe

Fig 5.9 shows the B-mode image of four consecutive acquisitions, which is the summation of 500 compounded frames after the mean subtraction to remove the tube wall reflections. Fig 5.10 and Fig 5.11 show the results of the PI and AM sequence, with the transmission frequency at 1.95MHz. Little difference can be seen from the results regarding the intensities of different sizes of monodispersed MBs.

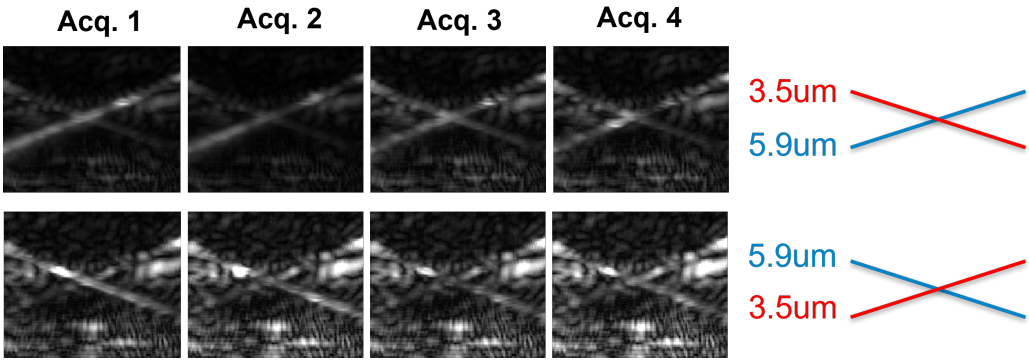


Figure 5.9: BMode image using P4-2 *in vitro*, summed 500 frames with mean subtraction

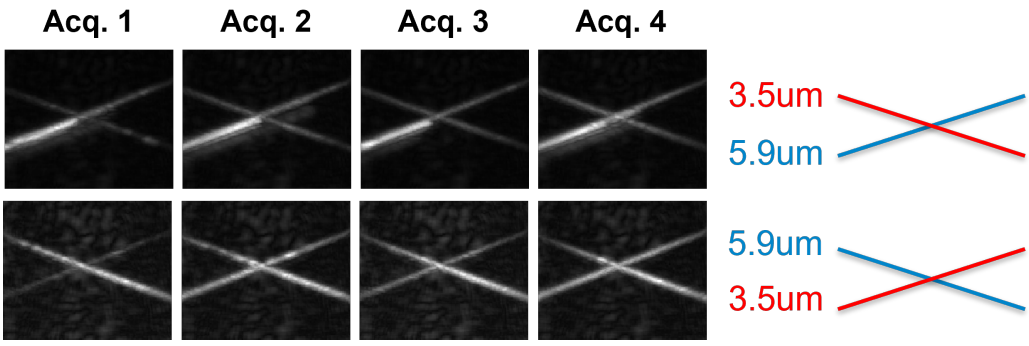


Figure 5.10: PI image using P4-2 *in vitro*, summed 500 frames

L12-3v Probe

Fig 5.12 shows the B-mode image of four consecutive acquisitions with two different transmission frequencies at 3.68MHz and 5MHz, which is the summation of 500 compounded frames after the mean subtraction to remove the tube wall reflections. Fig 5.13 and Fig 5.14 show the same

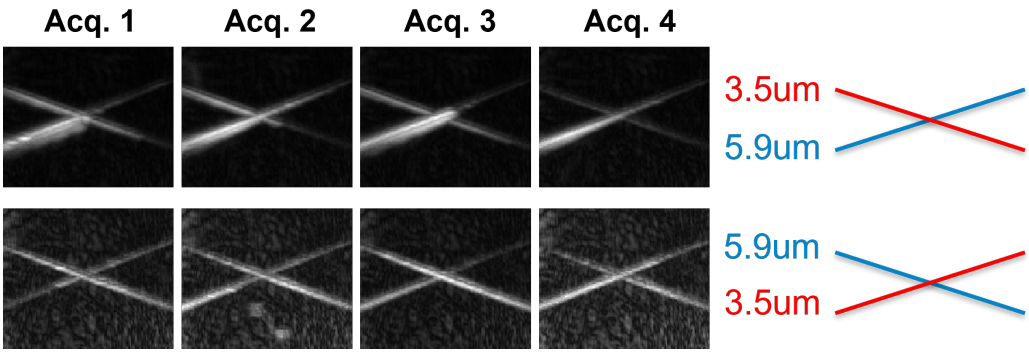


Figure 5.11: AM image using P4-2 *in vitro*, summed 500 frames

but the results of PI and AM sequence, respectively. Little difference can be seen regarding the intensities of different sizes of monodispersed MBs. PI images show weaker intensities than AM images due to the lack of fundamental signals.

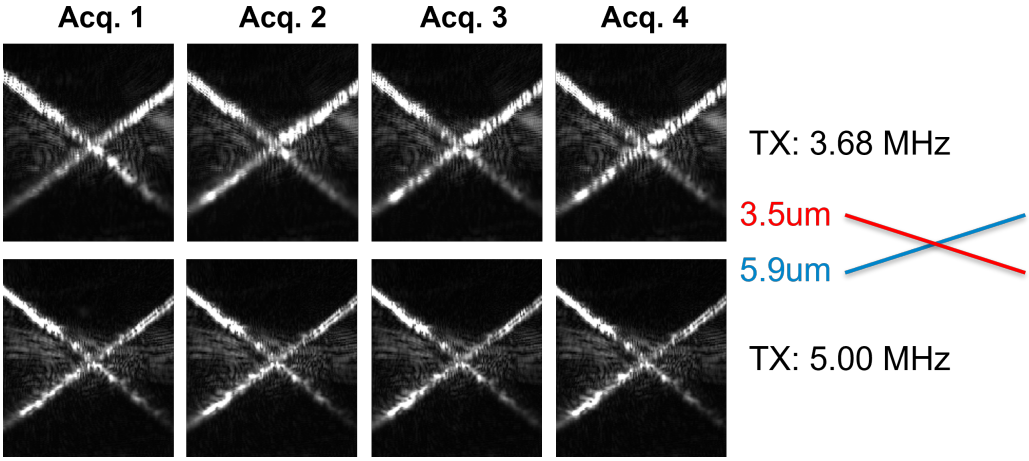


Figure 5.12: BMode image using L12-3v *in vitro*, summed 500 frames with mean subtraction

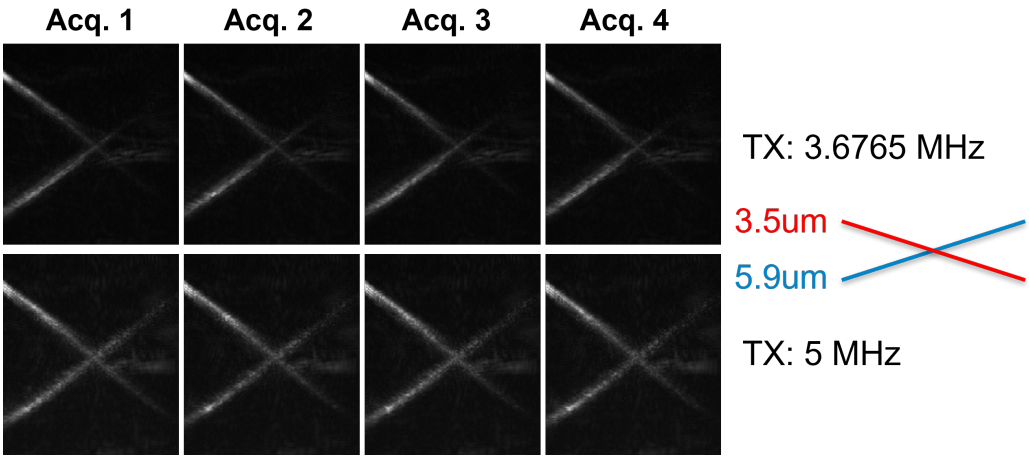


Figure 5.13: PI image using L12-3v *in vitro*, summed 500 frames

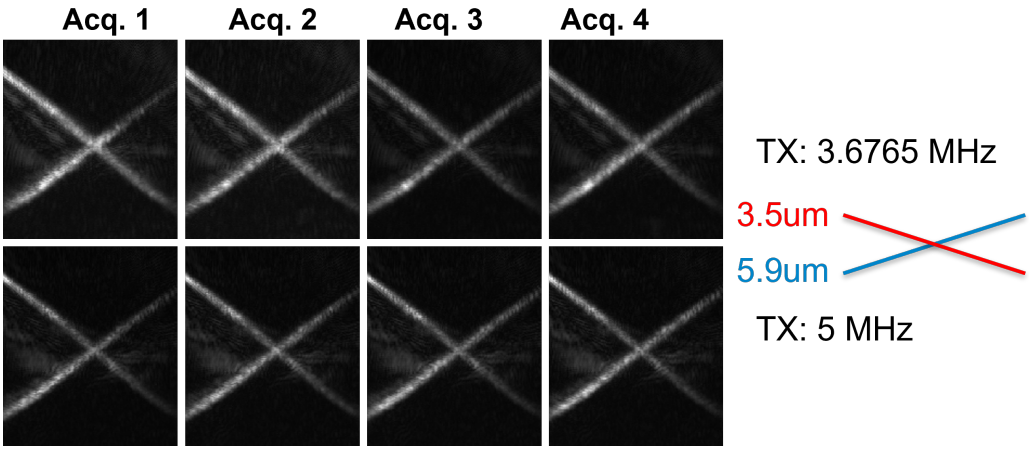


Figure 5.14: AM image using L12-3v *in vitro*, summed 500 frames

Matrix Probe

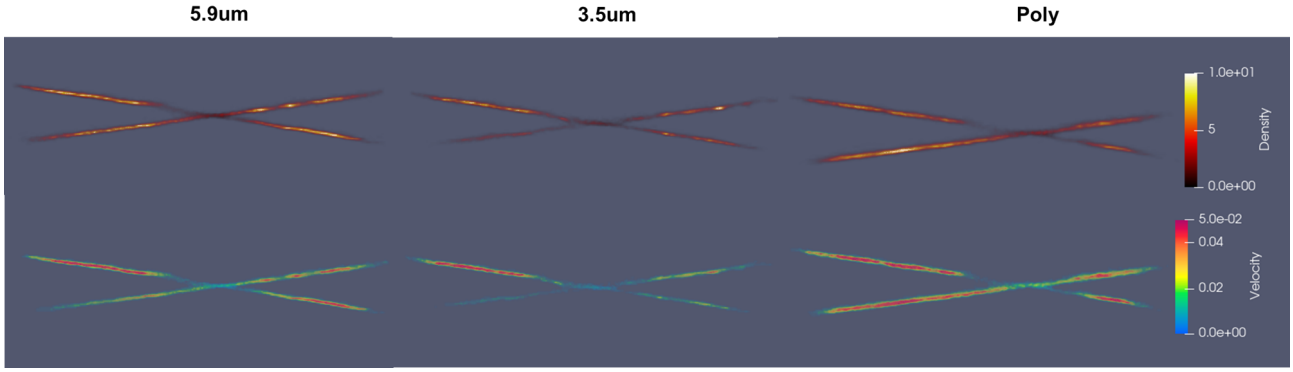


Figure 5.15: Localization and tracking results *in vitro* using matrix probe.

Fig 5.15 shows the localization and tracking results using a 3D tube phantom. The discontinuities in polydispersed microbubble images also correspond to the lower recall rate in simulation results.

5.4 Discussion

Fig 5.3 and Fig 5.4 indicate that under a moderate MI, the resonant larger bubble can emit higher intensity echoes, whether the pulse is short or long. This can be utilized to give prominence to signals from a certain-sized bubble during the imaging process. But when switching the excitation frequency to the resonant frequency of smaller sized bubbles, these smaller bubbles

will not generate stronger echoes than that of the off-resonance larger bubble, and therefore, it will not help in extracting different sized bubble signals relying on the echo intensity difference by switching the excitation frequencies.

The observation in Fig 5.6 corresponds to the conclusion drawn by [194] that larger-sized bubbles can help improve the detection sensitivity of SRUS *in vitro* and *in vivo*. The new simulation findings in this study are that this improved sensitivity may be explained by the increased localization recall rate of the larger bubble, which comes at the cost of larger localization errors and worse tracking performance. The larger localization error may be caused by their larger PSFs, and the uniform PSF may harm the tracking algorithm's performance that incorporates the graph-based optimization method.

The *in vitro* experimental results from Fig 5.9 to Fig 5.14 also show little different responses from two different-sized bubbles in reacting to different sequences or transmission frequencies, indicating that bubbles were not selectively excited. Some reasons may explain these little differences caused by the monodispersed microbubbles on 2D SRUS imaging *in vitro*.

Firstly, as mentioned above, for SR imaging purposes, a broadband transmission pulse is preferred to ensure a high axial resolution to help separate different UCA signals. The significant axial resolution decrease in Fig 5.7 compared to Fig 5.5 poses a challenge to the SRUS which requires UCA to be spatially separated. However, a narrower band excitation for a monodispersed microbubble would be preferred for specifically imaging a certain bubble size. Monodispersed bubbles have a narrower resonance frequency range, and if it matches with a narrow band excitation, more responses can be expected from these monodispered bubbles. As reported before, the control over the resonant microbubbles can be improved using a longer pulse to take advantage of their narrow band response. As reported before, the control over the resonant microbubbles can be improved using a longer pulse take advantage of their narrow band response. [192]. It is worth investigating how to use a longer pulse to enhance the control of monodispersed microbubbles while keeping the axial resolution.

Secondly, due to practical reasons, the bandwidth of the 1D probes, P4-2, L12-3v cannot cover the response spectrum of monodispersed microbubbles very well. Due to the manufacture limitations, the smallest monodispersed microbubble that can be manufactured is around $3.5\mu m$,

whose resonant frequency is 3.5MHz. However, a probe that has a bandwidth between 2-10 MHz is not available in this lab currently.

The other possible solution is to use smaller-sized monodisperse microbubbles. As reported, when using the nonlinear CPS imaging mode, bubbles smaller than $3.5\mu m$ have an advantage regarding the contrast-to-tissue ratio [275]. This may be because smaller bubbles have a higher percentage of non-linear components [192], which is also verified using the simulation results in Fig 5.3 and Fig 5.4. However, this higher non-linearity comes at the cost of lower response amplitude compared to larger MBs [275, 184], especially when the larger MB is at resonance, as shown in Fig 5.3 and Fig 5.4. This needs further investigation.

Besides, some studies also reported that larger-sized MBs always generate the best SRUS images compared to other selected sizes *in silico* [278], *in vitro* [194] and *in vivo* [279, 194] in BMode, and even under harmonic imaging mode [279], thanks to their stronger response. Therefore, whether the benefit of higher non-linearity of smaller MBs ($< 3\mu$m) will be canceled out by their weaker response still needs investigation.

Thirdly, the other possible reason is that the microbubble parameters used in the Marmonttant model [182], including the surrounding liquid density and liquid viscosity, the surface viscosity of the monolayer are different from that of practical bubbles, causing mismatches between the simulation and the experimental results.

Fig 5.8 and Table 5.8 indicate that in 3D SRUS imaging, polydispersed microbubble has a lower recall rate, but the gap between it and the best recall rate of the largest monodispersed MB is enlarged compared to the 2D SRUS results. This is also reflected by the *in silico* and *in vitro* images where tube images using polydispersed MBs have more discontinuities. However, this higher sensitivity of monodispersed MBs in 3D comes at the cost of lower localization precision in high-concentration scenarios, and slightly lower tracking score in low-concentration scenarios, according to the results *in silico*.

It is worth noting that in both 2D SRUS and 3D SRUS simulation results, the tracking performance using polydispersed MBs is better. This may be because the more homogenous PSFs of monodispersed MBs cause difficulties in the tracker pairing different similar-sized MBs. Whereas it is easier to pair different MBs with larger size differences as their signals differ more

from each other.

Another potential concern of using monodisperse microbubbles in imaging is the stability of their size distribution. Once injected into a physiological environment and undergoing varied pressure, how will the size distribution change or persist hasn't been investigated yet. This would also affect the expectation of its effect on SR performance *in vivo* using Bmode or contrast mode imaging.

5.5 Conclusion

This chapter compared the performance of monodispersed and polydispersed microbubbles *in simulation* and *in vitro* using linear array and matrix array probes. Results show that using monodispersed microbubbles can improve the localization recall rate in SRUS, at a cost of larger localization errors and tracking performance. Therefore, it is concluded that the monodispersed microbubble we used in these experiments doesn't have a significant advantage in reducing the acquisition time of SR US or improving the SR US performance based on the investigation above.

Statement of Contributions

Marcelo developed the BUFF simulation software, Kai contributed to the research proposal and investigation plan, and helped with the experimental setup. Bingxue implemented the simulation using BUFF, finished the experiments, and conducted the analysis.

Chapter 6

Conclusion

6.1 Summary of Thesis Achievements

This thesis proposed two projection SRUS imaging techniques using two types of probes to acquire information within a volume, using significantly less hardware and computational costs than 3D SRUS, which holds promise to improve the repeatability in clinical studies and therefore promote the clinical translation of the SRUS technique. The effects of monodispersed MBs on SRUS imaging performance were also investigated and it is concluded that no significant advantage can be achieved by using these specific monodispersed MBs and the probes available to us.

6.2 Future Work

As mentioned in Chapter 3, the work was done using a matrix array probe to synthesize different types of probes, including the proposed 1D unfocused array probe. It is also worth investigating the feasibility of using a row-column-addressed array probe that has long, orthogonal elements along both lateral directions for BEPSR. To perform projection imaging, instead of transmitting using columns/rows and receiving using rows/columns, only columns/rows can

be used for both transmission and reception without exchange. Enabling the RCA probe to be able to switch between 3D imaging and BEP imaging, where the previous process can be slow in real-time imaging due to the large image volume, while the latter can help to achieve SRUS in real-time with volumetric information.

All the work in Chapter 3 and Chapter 4 was done using the 2D matrix probe, which brought four disadvantages. Firstly, 1024 channels of data need to be transferred and processed, which slows down the data acquisition speed and the beamforming frame rate in real-time imaging. Secondly, to drive the matrix probe in full, four 256-channel ultrasound drivers e.g. Verasoinics systems are needed. Only one Verasonics system was used in this work and the matrix probe was driven in a multiplexing mode. This reduced the maximum imaging frame rate that can be achieved by four. Thirdly, the high level of cross-talk between different channels of this probe has increased the coherence level of noise signals, which increases the noise level after summing the signals and deteriorates the projection performance as a consequence. Last but not least, the dead rows between these sub-apertures of the matrix probe, necessary for the fabrication process, introduce uneven volume coverage and a heterogeneous pressure field within an imaging depth of 20mm, decreasing the imaging performance. Therefore, it is worth manufacturing a genuine 1D unfocused array probe by replacing the elevational focused lens with a flat lens of an existing 1D linear probe and investigating the feasibility of BEP-SR in real-time using this probe, hopefully with less data to process, faster imaging frame rate, higher signal-to-noise ratio, and more homogenous pressure field.

It is also worth manufacturing a 1.75D array probe to investigate how MAPSR will work in real-time and how the number of row elements of a 1.75D array probe would affect its performance. As mentioned in Chapter 4, it is hypothesized that even a two-row 1.75D array probe can help improve the projection imaging technique's dependence on contrast agents' sparsity, thanks to the reduced element height along the projection direction. Quantitative studies need to be done to investigate if the benefits of additional rows of elements and thus decreased element height are worth the cost of more hardware complexity and computational cost which includes multiple times more motion correction in the post-processing.

It would be worth thinking about potential clinical applications using these techniques. Both

the *in vivo* results in Chapter 3 and Chapter 4 using rabbit kidney and porcine heart, respectively, have broad branches that benefit the projection methods in addressing the volumetric information capturing ability. However, it was found difficult to process the full-view rabbit kidney dataset due to the high-density vessel networks, even using the MAPSR technique together with decreased contrast agent concentrations. Therefore, collaborating with clinicians and scoping the clinical application area would be significantly helpful. Breast tumors may be a good choice to start with, as the microvessels inside the volume have been realized to be usually torturous and sparse, according to the initial observation from another project within this group.

Apart from the perspective of clinical applications, further studies can be done to enhance the techniques by introducing other processing algorithms. For example, as mentioned in Chapter 3, one benefit of the proposed projection SR techniques is to track microbubbles in the lateral depth direction (2D coordinate) even when they also move in the elevational direction (3D coordinate). While the disadvantage of doing so is the underestimation of the speed, due to the lack of a full volumetric velocity vector. However, it is possible to calculate the direction vector component in the elevational direction from the gradient of microbubble power feature change along the same track. Regarding this problem, as seen in Fig 6.1, microbubble intensity change on the same track along consecutive frames may have two causes: Firstly, as aforementioned, the same microbubble moving along the elevational direction may have gradually decreased power feature along its track. Secondly, two bubbles that have different intensities that are de-

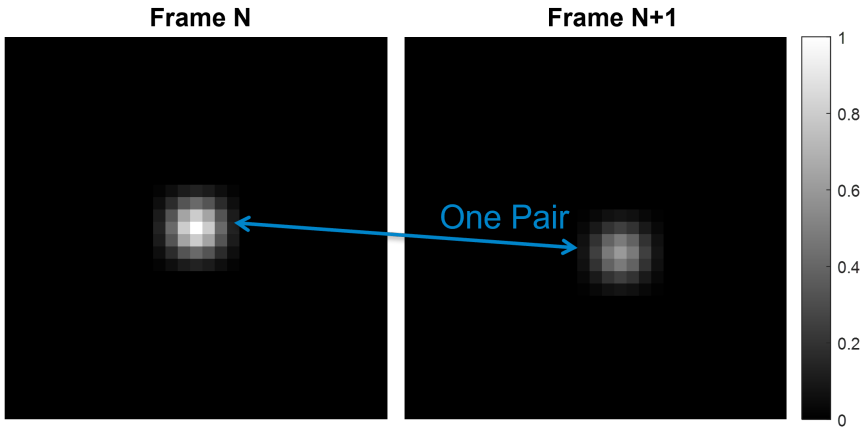


Figure 6.1: A pair of bubbles in two consecutive frames.

termined by their distinct response characteristics are paired incorrectly. This is more likely to happen when using polydispersed microbubbles that have large MB intensity variations, as seen in Fig 5.5. In contrast, using monodispersed MB with more uniform MB intensity distributions, as well as a motion model, may help exclude the second reason, where the intensity change is more likely caused by the out-of-plane motion, and consequently, help with the direction vector reconstruction. However, as discovered in Chapter 5, using monodispersed MB degrades the tracking algorithms' performance due to the homogenous MB PSFs. Therefore, whether using monodispersed MB can improve the direction vector reconstruction needs further study.
The other study that can also potentially enhance the projection SRUS technique is utilizing the edge wave information that causes the signal elongation along the axial direction due to the long height of the elements. The image feature of this edge wave information can be used to reconstruct the 3D and thus the elevational information. A trial investigation has been made using deep learning methods like convolutional neural networks (CNN) to reconstruct the 3D image from the projection image using the network provided by [280]. In Fig 6.2, the 3D image was reconstructed successfully using the projection X-ray image.

To adapt the network to our application objective, simulations were conducted using a 1D

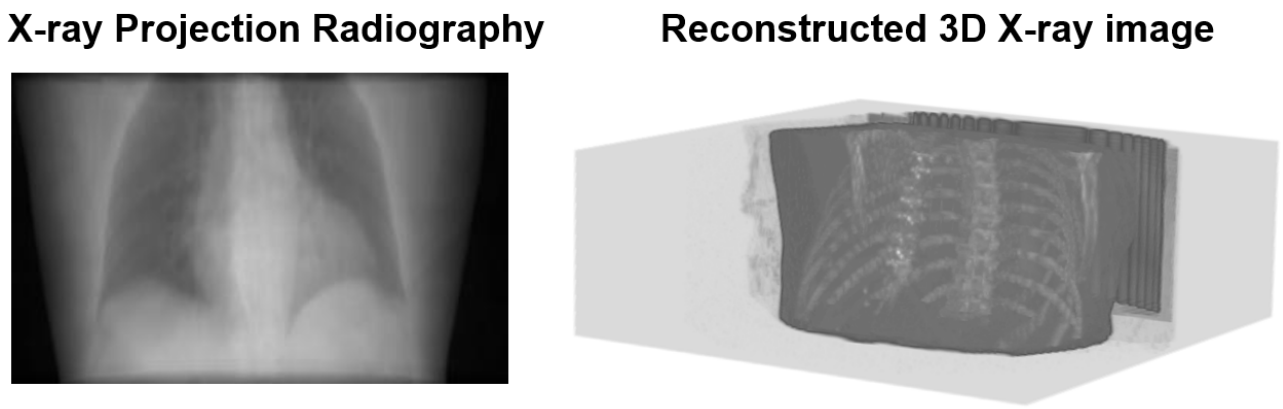


Figure 6.2: 3D reconstruction (right) using X-ray projection image (left) using networks and dataset provided by [280].

unfocused array probe, and 2D beamforming was performed to generate the projection images. Then the projection image was used as the input, and the reference 3D image was used as the output of the model. Using the same network architecture as [280] and trained 1000 epochs, the reconstructed 3D B-mode image can be generated from the projection B-mode image, as seen

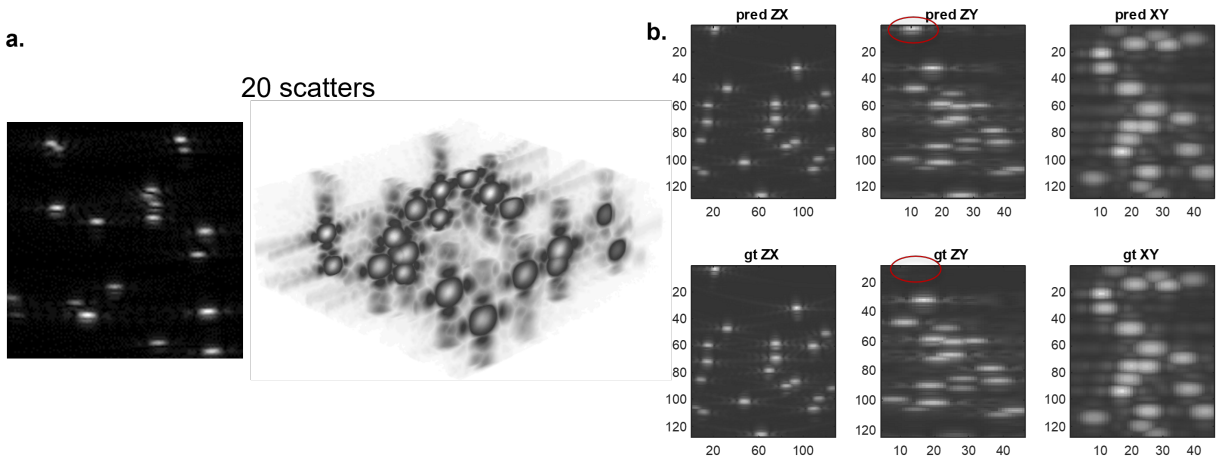


Figure 6.3: a.3D reconstruction (right) using projection Bmode image (left) using networks trained in [280]. b. Comparisons of the 3D reconstructed results with the ground truth results, using the MIP image from three directions. 'pred' means reconstructed image, 'gt' means 3D simulation results as the ground truth. Z: depth, X: lateral, Y: elevational.

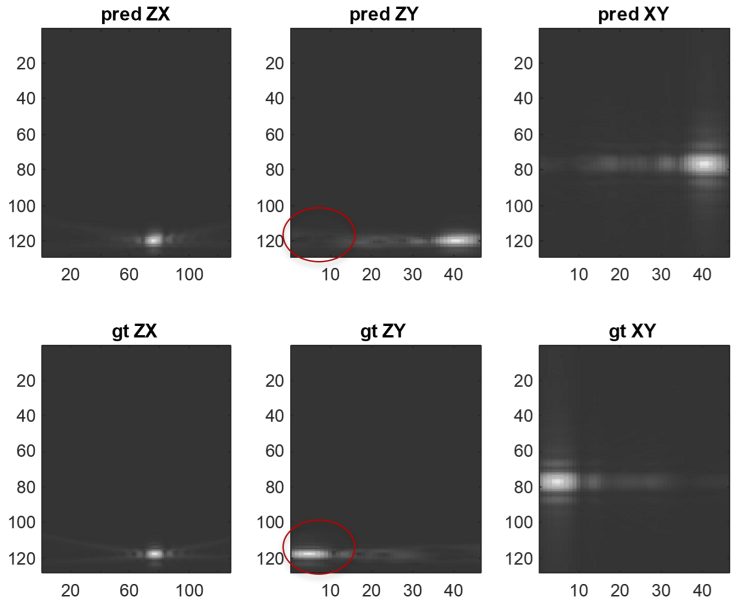


Figure 6.4: Comparisons of the 3D reconstructed results with the ground truth results using single scatterer.

in Fig 6.3 a. It shows the simulated 2D Bmode images on the left and the 3D reconstructions using the trained neural network. The lower row of images in Fig 6.3 b. gt ZX - gt XY. shows the 3D simulation ground truth generated by using the matrix probe and 3D beamforming, which works as the reference. The upper row of images in Fig 6.3 b. pred ZX - pred XY. shows the CNN reconstructed 3D image from three different views.

When comparing the two rows of images of Fig 6.3 b., most of the scatters were successfully

reconstructed from the projection image in the 3D space, whereas the network also generated some fake scatterers as indicated by the red circle. Another problem is that, as seen in Fig 6.4, where the upper row of the image shows the three different views of the CNN reconstructed 3D image and the lower row of the image shows the ground truth as a comparison, the network seems to be able to recognize the absolute displacement of one scatter from the central imaging plane. However, it gets confused about whether this scatter is above or below the center plane. Inspired by the previous study [2], it is hypothesized that using the two projection images from a two-row 1.75D array probe as the training input can help address such a problem. Since the two projection images contain information about the time-of-flight difference caused by the out-of-plane displacement. But whether it can help the network recognize an out-of-plane scatterer has a positive or negative elevational position still needs investigation.

Bibliography

[1] O. M. Viessmann, R. J. Eckersley, K. Christensen-Jeffries, M. X. Tang, and C. Dunsby, "Acoustic super-resolution with ultrasound and microbubbles," *Physics in Medicine and Biology*, vol. 58, no. 18, p. 6447–6458, Sep 2013.

[2] Y. Desailly, O. Couture, M. Fink, and M. Tanter, "Sono-activated ultrasound localization microscopy," *Applied Physics Letters*, vol. 103, no. 17, p. 174107, 2013.

[3] K. Christensen-Jeffries, J. Brown, P. Aljabar, M. Tang, C. Dunsby, and R. J. Eckersley, "In Vivo Acoustic Super-Resolution and Super-Resolved Velocity Mapping Using Microbubbles," *IEEE Transactions on Ultrasonics, Ferroelectrics, and Frequency Control*, vol. 34, no. 2, pp. 443–440, 2015.

[4] C. Errico, J. Pierre, S. Pezet, Y. Desailly, Z. Lenkei, O. Couture, and M. Tanter, "Ultrafast ultrasound localization microscopy for deep super-resolution vascular imaging," *Nature*, vol. 527, no. 7579, pp. 499–502, 2015. [Online]. Available: http://dx.doi.org/10.1038/nature16066

[5] T. Opacic, S. Dencks, B. Theek, M. Piepenbrock, D. Ackermann, A. Rix, T. Lammers, E. Stickeler, S. Delorme, G. Schmitz, and F. Kiessling, "Motion model ultrasound localization microscopy for preclinical and clinical multiparametric tumor characterization," *Nature Communications*, vol. 9, no. 1, 2018.

[6] P. Song, A. Manduca, J. D. Trzasko, and S. Chen, "Ultrasound small vessel imaging with block-wise adaptive local clutter filtering," *IEEE Transactions on Medical Imaging*, vol. 36, no. 1, pp. 251–262, 2017.

[7] J. Yu, L. Lavery, and K. Kim, "Super-resolution ultrasound imaging method for microvasculature in vivo with a high temporal accuracy," *Scientific Reports*, vol. 8, no. 1, pp. 1–11, 2018. [Online]. Available: http://dx.doi.org/10.1038/s41598-018-32235-2

[8] E. Kanoulas, M. Butler, C. Rowley, V. Voulgaridou, K. Diamantis, W. C. Duncan, A. Mcneilly, M. Averkiou, H. Wijkstra, M. Mischi, R. S. Wilson, W. Lu, and V. Sboros, "Super-Resolution Contrast-Enhanced Ultrasound Methodology for the Identification of In Vivo Vascular Dynamics in 2D," *Investigative Radiology*, 2019.

[9] T. Opacic, S. Dencks, B. Theek, M. Piepenbrock, D. Ackermann, A. Rix, T. Lammers, E. Stickeler, S. Delorme, G. Schmitz *et al.*, "Motion model ultrasound localization microscopy for preclinical and clinical multiparametric tumor characterization," *Nature communications*, vol. 9, no. 1, pp. 1–13, 2018.

[10] C. Huang, W. Zhang, P. Gong, U.-W. Lok, S. Tang, T. Yin, X. Zhang, L. Zhu, M. Sang, P. Song *et al.*, "Super-resolution ultrasound localization microscopy based on a high frame-rate clinical ultrasound scanner: An in-human feasibility study," *Physics in Medicine & Biology*, vol. 66, no. 8, p. 08NT01, 2021.

[11] W. Zhang, M. R. Lowerison, Z. Dong, R. J. Miller, K. A. Keller, and P. Song, "Super-resolution ultrasound localization microscopy on a rabbit liver vx2 tumor model: An initial feasibility study," *Ultrasound in medicine & biology*, vol. 47, no. 8, pp. 2416–2429, 2021.

[12] F. Lin, S. E. Shelton, D. Espíndola, J. D. Rojas, G. Pinton, and P. A. Dayton, "T h e r a n o s t i c s 3-D Ultrasound Localization Microscopy for Identifying Microvascular Morphology Features of Tumor Angiogenesis at a Resolution Beyond the Diffraction Limit of Conventional Ultrasound," vol. 7, no. 1, 2017.

[13] C. Bourquin, J. Porée, F. Lesage, and J. Provost, "In vivo pulsatility measurement of cerebral microcirculation in rodents using dynamic ultrasound localization microscopy," *IEEE Transactions on Medical Imaging*, vol. 41, no. 4, pp. 782–792, 2021.

[14] T. Deffieux, C. Demené, and M. Tanter, "Functional ultrasound imaging: A new imaging modality for neuroscience," *Neuroscience*, vol. 474, pp. 110–121, 2021.

[15] M. R. Lowerison, N. V. Chandra Sekaran, Z. Dong, X. Chen, Q. You, D. A. Llano, and P. Song, "Super-resolution ultrasound imaging of cerebrovascular impairment in a mouse model of alzheimer's disease," *bioRxiv*, pp. 2022–10, 2022.

[16] A. Chavignon, V. Hingot, C. Orset, D. Vivien, and O. Couture, "3d transcranial ultrasound localization microscopy for discrimination between ischemic and hemorrhagic stroke in early phase," *Scientific Reports*, vol. 12, no. 1, p. 14607, 2022.

[17] O. Demeulenaere, Z. Sandoval, P. Mateo, A. Dizeux, O. Villemain, R. Gallet, B. Ghaleh, T. Deffieux, C. Demené, M. Tanter *et al.*, "Coronary flow assessment using 3-dimensional ultrafast ultrasound localization microscopy," *Cardiovascular Imaging*, vol. 15, no. 7, pp. 1193–1208, 2022.

[18] P. Cormier, J. Porée, C. Bourquin, and J. Provost, "Dynamic myocardial ultrasound localization angiography," *IEEE Transactions on Medical Imaging*, vol. 40, no. 12, pp. 3379–3388, 2021.

[19] K. Christensen-Jeffries, J. Brown, S. Harput, G. Zhang, J. Zhu, M.-X. Tang, C. Dunsby, and R. J. Eckersley, "Poisson statistical model of ultrasound super-resolution imaging acquisition time," *IEEE transactions on ultrasonics, ferroelectrics, and frequency control*, vol. 66, no. 7, pp. 1246–1254, 2019.

[20] C. Huang, M. R. Lowerison, J. D. Trzasko, A. Manduca, Y. Bresler, S. Tang, P. Gong, U.-W. Lok, P. Song, and S. Chen, "Short acquisition time super-resolution ultrasound microvessel imaging via microbubble separation," *Scientific reports*, vol. 10, no. 1, p. 6007, 2020.

[21] "Sushi: Sparsity-based ultrasound super-resolution hemodynamic imaging," *IEEE Transactions on Ultrasonics, Ferroelectrics, and Frequency Control*, vol. 65, no. 12, 2018.

[22] R. J. van Sloun, O. Solomon, M. Bruce, Z. Z. Khaing, H. Wijkstra, Y. C. Eldar, and M. Mischi, "Super-resolution ultrasound localization microscopy through deep learning," *IEEE transactions on medical imaging*, vol. 40, no. 3, pp. 829–839, 2020.

[23] X. Chen, M. R. Lowerison, Z. Dong, N. V. C. Sekaran, D. A. Llano, and P. Song, "Localization free super-resolution microbubble velocimetry using a long short-term memory neural network," *IEEE transactions on medical imaging*, vol. 42, no. 8, pp. 2374–2385, 2023.

[24] M. A. O'Reilly and K. Hynynen, "A super-resolution ultrasound method for brain vascular mapping," *Medical physics*, vol. 40, no. 11, p. 110701, 2013.

[25] O. Demeulenaere, A. Bertolo, S. Pezet, N. Ialy-Radio, B. Osmanski, C. Papadacci, M. Tanter, T. Deffieux, and M. Pernot, "In vivo whole brain microvascular imaging in mice using transcranial 3d ultrasound localization microscopy," *EBioMedicine*, vol. 79, 2022.

[26] J. Provost, C. Papadacci, J. E. Arango, M. Imbault, M. Fink, J.-L. Gennisson, M. Tanter, and M. Pernot, "3d ultrafast ultrasound imaging in vivo," *Physics in Medicine & Biology*, vol. 59, no. 19, p. L1, 2014.

[27] F. Foroozan, M. A. O'Reilly, and K. Hynynen, "Microbubble localization for three-dimensional superresolution ultrasound imaging using curve fitting and deconvolution methods," *IEEE Transactions on Biomedical Engineering*, vol. 65, no. 12, pp. 2692–2703, 2018.

[28] H. J. Granger, M. E. Schelling, R. E. Lewis, D. C. Zawieja, and C. J. Meininger, "Physiology and pathobiology of the microcirculation," *American Journal of Otolaryngology*, vol. 9, no. 6, pp. 264–277, 1988.

[29] R. N. Pittman, "Oxygen transport in the microcirculation and its regulation," *Microcirculation*, vol. 20, no. 2, pp. 117–137, 2013.

[30] P. F. Davies, S.-P. Olesen, D. E. Clapham, E. M. Morrel, and F. J. Schoen, "Endothelial communication. state of the art lecture." *Hypertension*, vol. 11, no. 6_pt_2, pp. 563–572, 1988.

[31] J. Vajda, M. Milojević, U. Maver, and B. Vihar, "Microvascular tissue engineering—a review," *Biomedicines*, vol. 9, no. 6, p. 589, 2021.

[32] V. Muthukkaruppan, L. Kubai, and R. Auerbach, "Tumor-induced neovascularization in the mouse eye," *Journal of the National Cancer Institute*, vol. 69, no. 3, pp. 699–708, 1982.

[33] N. Nishida, H. Yano, T. Nishida, T. Kamura, and M. Kojiro, "Angiogenesis in cancer," *Vascular health and risk management*, vol. 2, no. 3, pp. 213–219, 2006.

[34] J. M. Gijtenbeek, P. Wesseling, C. Maass, L. Burgers, and J. A. van der Laak, "Three-dimensional reconstruction of tumor microvasculature: simultaneous visualization of multiple components in paraffin-embedded tissue," *Angiogenesis*, vol. 8, pp. 297–305, 2006.

[35] C. A. Den Uil, E. Klijn, W. K. Lagrand, J. J. Brugts, C. Ince, P. E. Spronk, and M. L. Simoons, "The microcirculation in health and critical disease," *Progress in cardiovascular diseases*, vol. 51, no. 2, pp. 161–170, 2008.

[36] J. E. Tooke, "Microvascular function in human diabetes: a physiological perspective," *Diabetes*, vol. 44, no. 7, pp. 721–726, 1995.

[37] E. J. Barrett, Z. Liu, M. Khamaisi, G. L. King, R. Klein, B. E. Klein, T. M. Hughes, S. Craft, B. I. Freedman, D. W. Bowden *et al.*, "Diabetic microvascular disease: an endocrine society scientific statement," *The Journal of Clinical Endocrinology & Metabolism*, vol. 102, no. 12, pp. 4343–4410, 2017.

[38] Z. He and G. L. King, "Microvascular complications of diabetes," *Endocrinology and Metabolism Clinics*, vol. 33, no. 1, pp. 215–238, 2004.

[39] M. K. Ikram, J. A. Janssen, A. M. Roos, I. Rietveld, J. C. Witteman, M. M. Breteler, A. Hofman, C. M. Van Duijn, and P. T. de Jong, "Retinal vessel diameters and risk of

impaired fasting glucose or diabetes: the rotterdam study," *Diabetes*, vol. 55, no. 2, pp. 506–510, 2006.

[40] M. M. Nentwich and M. W. Ulbig, "Diabetic retinopathy-ocular complications of diabetes mellitus," *World journal of diabetes*, vol. 6, no. 3, p. 489, 2015.

[41] N. Futrakul and P. Futrakul, "Biomarker for early renal microvascular and diabetic kidney diseases," *Renal Failure*, vol. 39, no. 1, pp. 505–511, 2017.

[42] R. Malik, S. Tesfaye, S. Thompson, A. Veves, A. Sharma, A. Boulton, and J. Ward, "Endoneurial localisation of microvascular damage in human diabetic neuropathy," *Diabetologia*, vol. 36, pp. 454–459, 1993.

[43] M. J. Sheetz and G. L. King, "Molecular understanding of hyperglycemia's adverse effects for diabetic complications," *Jama*, vol. 288, no. 20, pp. 2579–2588, 2002.

[44] S. Khatibzadeh, F. Farzadfar, J. Oliver, M. Ezzati, and A. Moran, "Worldwide risk factors for heart failure: a systematic review and pooled analysis," *International journal of cardiology*, vol. 168, no. 2, pp. 1186–1194, 2013.

[45] D. R. Riddle, W. E. Sonntag, and R. J. Lichtenwalner, "Microvascular plasticity in aging," *Ageing research reviews*, vol. 2, no. 2, pp. 149–168, 2003.

[46] J. W. Baish and R. K. Jain, "Fractals and cancer," *Cancer research*, vol. 60, no. 14, pp. 3683–3688, 2000.

[47] E. Bullitt, D. Zeng, G. Gerig, S. Aylward, S. Joshi, J. K. Smith, W. Lin, and M. G. Ewend, "Vessel tortuosity and brain tumor malignancy: a blinded study1," *Academic radiology*, vol. 12, no. 10, pp. 1232–1240, 2005.

[48] A. A. Kalitzeos, G. Y. Lip, and R. Heitmar, "Retinal vessel tortuosity measures and their applications," *Experimental eye research*, vol. 106, pp. 40–46, 2013.

[49] J. De la Torre and G. Stefano, "Evidence that alzheimer's disease is a microvascular disorder: the role of constitutive nitric oxide," *Brain research reviews*, vol. 34, no. 3, pp. 119–136, 2000.

[50] L. Buée, P. Hof, C. Bouras, A. Delacourte, D. Perl, J. Morrison, and H. Fillit, "Pathological alterations of the cerebral microvasculature in alzheimer's disease and related dementing disorders," *Acta neuropathologica*, vol. 87, pp. 469–480, 1994.

[51] S. M. Daly and M. J. Leahy, "'go with the flow': a review of methods and advancements in blood flow imaging," *Journal of biophotonics*, vol. 6, no. 3, pp. 217–255, 2013.

[52] J. Allen and K. Howell, "Microvascular imaging: techniques and opportunities for clinical physiological measurements," *Physiological measurement*, vol. 35, no. 7, p. R91, 2014.

[53] E. Betzig, G. H. Patterson, R. Sougrat, O. W. Lindwasser, S. Olenych, J. S. Bonifacino, M. W. Davidson, J. Lippincott-Schwartz, and H. F. Hess, "Imaging intracellular fluorescent proteins at nanometer resolution," *science*, vol. 313, no. 5793, pp. 1642–1645, 2006.

[54] D. Huang, E. A. Swanson, C. P. Lin, J. S. Schuman, W. G. Stinson, W. Chang, M. R. Hee, T. Flotte, K. Gregory, C. A. Puliafito *et al.*, "Optical coherence tomography," *science*, vol. 254, no. 5035, pp. 1178–1181, 1991.

[55] J. M. Schmitt, "Optical coherence tomography (oct): a review," *IEEE Journal of selected topics in quantum electronics*, vol. 5, no. 4, pp. 1205–1215, 1999.

[56] K. Christensen-Jeffries, O. Couture, P. A. Dayton, Y. C. Eldar, K. Hynynen, F. Kiessling, M. O'Reilly, G. F. Pinton, G. Schmitz, M.-X. Tang *et al.*, "Super-resolution ultrasound imaging," *Ultrasound in medicine & biology*, vol. 46, no. 4, pp. 865–891, 2020.

[57] C. Errico, J. Pierre, S. Pezet, Y. Desailly, Z. Lenkei, O. Couture, and M. Tanter, "Ultrafast ultrasound localization microscopy for deep super-resolution vascular imaging," *Nature*, vol. 527, no. 7579, pp. 499–502, 2015.

[58] J. G. Fujimoto, "Optical coherence tomography for ultrahigh resolution in vivo imaging," *Nature biotechnology*, vol. 21, no. 11, pp. 1361–1367, 2003.

[59] F. I. Feldchtein, G. Gelikonov, V. Gelikonov, R. Iksanov, R. Kuranov, A. M. Sergeev, N. Gladkova, M. Ourutina, J. Warren, and D. Reitze, "In vivo oct imaging of hard and soft tissue of the oral cavity," *Optics express*, vol. 3, no. 6, pp. 239–250, 1998.

[60] N. D. Gladkova, G. Petrova, N. Nikulin, S. Radenska-Lopovok, L. Snopova, Y. P. Chumakov, V. Nasonova, V. Gelikonov, G. Gelikonov, R. Kuranov *et al.*, "In vivo optical coherence tomography imaging of human skin: norm and pathology," *Skin Research and Technology*, vol. 6, no. 1, pp. 6–16, 2000.

[61] E. A. Swanson, J. A. Izatt, M. R. Hee, D. Huang, C. Lin, J. Schuman, C. Puliafito, and J. G. Fujimoto, "In vivo retinal imaging by optical coherence tomography," *Optics letters*, vol. 18, no. 21, pp. 1864–1866, 1993.

[62] N. Nassif, B. Cense, B. Park, M. Pierce, S. Yun, B. Bouma, G. Tearney, T. Chen, and J. De Boer, "In vivo high-resolution video-rate spectral-domain optical coherence tomography of the human retina and optic nerve," *Optics express*, vol. 12, no. 3, pp. 367–376, 2004.

[63] Z. Chen, T. E. Milner, S. Srinivas, X. Wang, A. Malekafzali, M. J. van Gemert, and J. S. Nelson, "Noninvasive imaging of in vivo blood flow velocity using optical doppler tomography," *Optics letters*, vol. 22, no. 14, pp. 1119–1121, 1997.

[64] X. Wang, T. Milner, and J. Nelson, "Characterization of fluid flow velocity by optical doppler tomography," *Optics letters*, vol. 20, no. 11, pp. 1337–1339, 1995.

[65] Y. Zhao, Z. Chen, C. Saxer, S. Xiang, J. F. de Boer, and J. S. Nelson, "Phase-resolved optical coherence tomography and optical doppler tomography for imaging blood flow in human skin with fast scanning speed and high velocity sensitivity," *Optics letters*, vol. 25, no. 2, pp. 114–116, 2000.

[66] B. R. White, M. C. Pierce, N. Nassif, B. Cense, B. H. Park, G. J. Tearney, B. E. Bouma, T. C. Chen, and J. F. De Boer, "In vivo dynamic human retinal blood flow imaging using ultra-high-speed spectral domain optical doppler tomography," *Optics express*, vol. 11, no. 25, pp. 3490–3497, 2003.

[67] M. Xu and L. V. Wang, "Photoacoustic imaging in biomedicine," *Review of scientific instruments*, vol. 77, no. 4, 2006.

[68] P. Beard, "Biomedical photoacoustic imaging," *Interface focus*, vol. 1, no. 4, pp. 602–631, 2011.

[69] Q. Fu, R. Zhu, J. Song, H. Yang, and X. Chen, "Photoacoustic imaging: contrast agents and their biomedical applications," *Advanced Materials*, vol. 31, no. 6, p. 1805875, 2019.

[70] Z. Chaudhary, G. M. Khan, M. M. Abeer, N. Pujara, B. W.-C. Tse, M. A. McGuckin, A. Popat, and T. Kumeria, "Efficient photoacoustic imaging using indocyanine green (icg) loaded functionalized mesoporous silica nanoparticles," *Biomaterials science*, vol. 7, no. 12, pp. 5002–5015, 2019.

[71] K. H. Song, E. W. Stein, J. A. Margenthaler, and L. V. Wang, "Noninvasive photoacoustic identification of sentinel lymph nodes containing methylene blue in vivo in a rat model," *Journal of biomedical optics*, vol. 13, no. 5, pp. 054 033–054 033, 2008.

[72] A. A. Oraevsky, V. A. Andreev, A. A. Karabutov, R. D. Fleming, Z. Gatalica, H. Singh, and R. O. Esenaliev, "Laser optoacoustic imaging of the breast: detection of cancer angiogenesis," in *Optical tomography and spectroscopy of tissue III*, vol. 3597. SPIE, 1999, pp. 352–363.

[73] R. A. Kruger, R. B. Lam, D. R. Reinecke, S. P. Del Rio, and R. P. Doyle, "Photoacoustic angiography of the breast," *Medical physics*, vol. 37, no. 11, pp. 6096–6100, 2010.

[74] H. Wang, C. Liu, X. Gong, D. Hu, R. Lin, Z. Sheng, C. Zheng, M. Yan, J. Chen, L. Cai *et al.*, "In vivo photoacoustic molecular imaging of breast carcinoma with folate receptor-targeted indocyanine green nanoprobes," *Nanoscale*, vol. 6, no. 23, pp. 14 270–14 279, 2014.

[75] J. J. Niederhauser, M. Jaeger, R. Lemor, P. Weber, and M. Frenz, "Combined ultrasound and optoacoustic system for real-time high-contrast vascular imaging in vivo," *IEEE transactions on medical imaging*, vol. 24, no. 4, pp. 436–440, 2005.

[76] S. Jiao, M. Jiang, J. Hu, A. Fawzi, Q. Zhou, K. K. Shung, C. A. Puliafito, and H. F. Zhang, "Photoacoustic ophthalmoscopy for in vivo retinal imaging," *Optics express*, vol. 18, no. 4, pp. 3967–3972, 2010.

[77] M. A. Lediju Bell, "Photoacoustic imaging for surgical guidance: Principles, applications, and outlook," *Journal of applied physics*, vol. 128, no. 6, 2020.

[78] A. N. S. Institute, *American national standard for safe use of lasers*. Laser Institute of America, 2022.

[79] Y. Li, W. Zhang, V. P. Nguyen, N. W. Khan, X. Xia, X. Wang, and Y. M. Paulus, "Retinal safety evaluation of photoacoustic microscopy," *Experimental eye research*, vol. 202, p. 108368, 2021.

[80] K. M. Kempski, A. Wiacek, M. Graham, E. González, B. Goodson, D. Allman, J. Palmer, H. Hou, S. Beck, J. He *et al.*, "In vivo photoacoustic imaging of major blood vessels in the pancreas and liver during surgery," *Journal of biomedical optics*, vol. 24, no. 12, pp. 121 905–121 905, 2019.

[81] P. C. Lauterbur, "Image formation by induced local interactions: examples employing nuclear magnetic resonance," *nature*, vol. 242, no. 5394, pp. 190–191, 1973.

[82] P. Mansfield and P. K. Grannell, "Nmr'diffraction'in solids?" *Journal of Physics C: solid state physics*, vol. 6, no. 22, p. L422, 1973.

[83] R. J. Kim, E. Wu, A. Rafael, E.-L. Chen, M. A. Parker, O. Simonetti, F. J. Klocke, R. O. Bonow, and R. M. Judd, "The use of contrast-enhanced magnetic resonance imaging to identify reversible myocardial dysfunction," *New England Journal of Medicine*, vol. 343, no. 20, pp. 1445–1453, 2000.

[84] A. S. Merbach, L. Helm, and E. Toth, *The chemistry of contrast agents in medical magnetic resonance imaging*. John Wiley & Sons, 2013.

[85] P. Caravan, J. J. Ellison, T. J. McMurry, and R. B. Lauffer, "Gadolinium (iii) chelates as mri contrast agents: structure, dynamics, and applications," *Chemical reviews*, vol. 99, no. 9, pp. 2293–2352, 1999.

[86] D. Pouliquen, J. Le Jeune, R. Perdrisot, A. Ermias, and P. Jallet, "Iron oxide nanoparticles for use as an mri contrast agent: pharmacokinetics and metabolism," *Magnetic resonance imaging*, vol. 9, no. 3, pp. 275–283, 1991.

[87] C. F. van Dijke, R. C. Brasch, T. Roberts, N. Weidner, A. Mathur, D. M. Shames, J. S. Mann, F. Demsar, P. Lang, and H. C. Schwickert, "Mammary carcinoma model: correlation of macromolecular contrast-enhanced mr imaging characterizations of tumor microvasculature and histologic capillary density." *Radiology*, vol. 198, no. 3, pp. 813–818, 1996.

[88] N. J. Pelc, R. J. Herfkens, A. Shimakawa, D. R. Enzmann *et al.*, "Phase contrast cine magnetic resonance imaging," *Magnetic resonance quarterly*, vol. 7, no. 4, pp. 229–254, 1991.

[89] P. D. Gatehouse, J. Keegan, L. A. Crowe, S. Masood, R. H. Mohiaddin, K.-F. Kreitner, and D. N. Firmin, "Applications of phase-contrast flow and velocity imaging in cardiovascular mri," *European radiology*, vol. 15, pp. 2172–2184, 2005.

[90] C. L. Dumoulin and H. Hart Jr, "Magnetic resonance angiography." *Radiology*, vol. 161, no. 3, pp. 717–720, 1986.

[91] W. Y. Kim, P. G. Danias, M. Stuber, S. D. Flamm, S. Plein, E. Nagel, S. E. Langerak, O. M. Weber, E. M. Pedersen, M. Schmidt *et al.*, "Coronary magnetic resonance angiography for the detection of coronary stenoses," *New England Journal of Medicine*, vol. 345, no. 26, pp. 1863–1869, 2001.

[92] M. Stuber, R. M. Botnar, P. G. Danias, D. K. Sodickson, K. V. Kissinger, M. Van Cauteren, J. De Becker, and W. J. Manning, "Double-oblique free-breathing high resolution three-dimensional coronary magnetic resonance angiography," *Journal of the American College of Cardiology*, vol. 34, no. 2, pp. 524–531, 1999.

[93] N. K. Logothetis, "What we can do and what we cannot do with fmri," *Nature*, vol. 453, no. 7197, pp. 869–878, 2008.

[94] K. Uludağ, D. J. Dubowitz, E. J. Yoder, K. Restom, T. T. Liu, and R. B. Buxton, "Coupling of cerebral blood flow and oxygen consumption during physiological activation and deactivation measured with fmri," *Neuroimage*, vol. 23, no. 1, pp. 148–155, 2004.

[95] K. N. Ochsner, S. A. Bunge, J. J. Gross, and J. D. Gabrieli, "Rethinking feelings: an fmri study of the cognitive regulation of emotion," *Journal of cognitive neuroscience*, vol. 14, no. 8, pp. 1215–1229, 2002.

[96] V. G. Kemper, F. De Martino, T. C. Emmerling, E. Yacoub, and R. Goebel, "High resolution data analysis strategies for mesoscale human functional mri at 7 and 9.4 t," *Neuroimage*, vol. 164, pp. 48–58, 2018.

[97] E. Macé, G. Montaldo, I. Cohen, M. Baulac, M. Fink, and M. Tanter, "Functional ultrasound imaging of the brain," *Nature methods*, vol. 8, no. 8, pp. 662–664, 2011.

[98] K.-H. Herrmann, S. Schmidt, A. Kretz, R. Haenold, I. Krumbein, M. Metzler, C. Gaser, O. W. Witte, and J. R. Reichenbach, "Possibilities and limitations for high resolution small animal mri on a clinical whole-body 3t scanner," *Magnetic Resonance Materials in Physics, Biology and Medicine*, vol. 25, pp. 233–244, 2012.

[99] T. C. Arnold, C. W. Freeman, B. Litt, and J. M. Stein, "Low-field mri: clinical promise and challenges," *Journal of Magnetic Resonance Imaging*, vol. 57, no. 1, pp. 25–44, 2023.

[100] A. E. Campbell-Washburn, R. Ramasawmy, M. C. Restivo, I. Bhattacharya, B. Basar, D. A. Herzka, M. S. Hansen, T. Rogers, W. P. Bandettini, D. R. McGuirt *et al.*, "Opportunities in interventional and diagnostic imaging by using high-performance low-field-strength mri," *Radiology*, vol. 293, no. 2, pp. 384–393, 2019.

[101] C.-A. Park, C.-K. Kang, Y.-B. Kim, and Z.-H. Cho, "Advances in mr angiography with 7t mri: From microvascular imaging to functional angiography," *Neuroimage*, vol. 168, pp. 269–278, 2018.

[102] B. E. Warren, *X-ray Diffraction*. Courier Corporation, 1990.

[103] M. Yaffe and J. Rowlands, "X-ray detectors for digital radiography," *Physics in Medicine & Biology*, vol. 42, no. 1, p. 1, 1997.

[104] G. N. Hounsfield, "Computerized transverse axial scanning (tomography): Part 1. description of system," *The British journal of radiology*, vol. 46, no. 552, pp. 1016–1022, 1973.

[105] N. England and N. Improvement, "Diagnostic imaging dataset statistical release," *London: Department of Health*, vol. 421, 2016.

[106] H. Park, E. Yeom, and S. J. Lee, "X-ray piv measurement of blood flow in deep vessels of a rat: An in vivo feasibility study," *Scientific Reports*, vol. 6, no. 1, p. 19194, 2016.

[107] S. Y. Jung, S. Ahn, K. H. Nam, J. P. Lee, and S. J. Lee, "In vivo measurements of blood flow in a rat using x-ray imaging technique," *The international journal of cardiovascular imaging*, vol. 28, pp. 1853–1858, 2012.

[108] R. Tanaka, "Dynamic chest radiography: flat-panel detector (fpd) based functional x-ray imaging," *Radiological physics and technology*, vol. 9, no. 2, pp. 139–153, 2016.

[109] C.-C. Chien, H.-H. Chen, S.-F. Lai, K.-C. Wu, X. Cai, Y. Hwu, C. Petibois, Y. Chu, and G. Margaritondo, "Gold nanoparticles as high-resolution x-ray imaging contrast agents for the analysis of tumor-related micro-vasculature," *Journal of nanobiotechnology*, vol. 10, pp. 1–12, 2012.

[110] J. C. Hsu, L. M. Nieves, O. Betzer, T. Sadan, P. B. Noël, R. Popovtzer, and D. P. Cormode, "Nanoparticle contrast agents for x-ray imaging applications," *Wiley Interdisciplinary Reviews: Nanomedicine and Nanobiotechnology*, vol. 12, no. 6, p. e1642, 2020.

[111] M. Winder, A. J. Owczarek, J. Chudek, J. Pilch-Kowalczyk, and J. Baron, "Are we overdoing it? changes in diagnostic imaging workload during the years 2010–2020 including the impact of the sars-cov-2 pandemic," in *Healthcare*, vol. 9, no. 11. Multidisciplinary Digital Publishing Institute, 2021, p. 1557.

[112] K. Klingenbeck-Regn, S. Schaller, T. Flohr, B. Ohnesorge, A. F. Kopp, and U. Baum, "Subsecond multi-slice computed tomography: basics and applications," *European journal of radiology*, vol. 31, no. 2, pp. 110–124, 1999.

[113] L. A. Feldkamp, L. C. Davis, and J. W. Kress, "Practical cone-beam algorithm," *Josa a*, vol. 1, no. 6, pp. 612–619, 1984.

[114] H. Lusic and M. W. Grinstaff, "X-ray-computed tomography contrast agents," *Chemical reviews*, vol. 113, no. 3, pp. 1641–1666, 2013.

[115] L. Axel, "Cerebral blood flow determination by rapid-sequence computed tomography: theoretical analysis." *Radiology*, vol. 137, no. 3, pp. 679–686, 1980.

[116] D. E. Kuhl, J. Engel Jr, M. E. Phelps, and C. Selin, "Epileptic patterns of local cerebral metabolism and perfusion in humans determined by emission computed tomography of 18fdg and 13nh3," *Annals of Neurology: Official Journal of the American Neurological Association and the Child Neurology Society*, vol. 8, no. 4, pp. 348–360, 1980.

[117] F. Plouraboué, P. Cloetens, C. Fonta, A. Steyer, F. Lauwers, and J.-P. Marc-Vergnes, "X-ray high-resolution vascular network imaging," *Journal of microscopy*, vol. 215, no. 2, pp. 139–148, 2004.

[118] H. Hacker and H. Becker, "Time controlled computed tomographic angiography." *Journal of computer assisted tomography*, vol. 1, no. 4, pp. 405–409, 1977.

[119] E. N. ARNETT, J. M. ISNER, D. R. REDWOOD, K. M. KENT, W. P. BAKER, H. ACKERSTEIN, and W. C. ROBERTS, "Coronary artery narrowing in coronary heart disease: comparison of cineangiographic and necropsy findings," *Annals of internal medicine*, vol. 91, no. 3, pp. 350–356, 1979.

[120] E. Lin and A. Alessio, "What are the basic concepts of temporal, contrast, and spatial resolution in cardiac ct?" *Journal of cardiovascular computed tomography*, vol. 3, no. 6, pp. 403–408, 2009.

[121] A. Hata, M. Yanagawa, O. Honda, N. Kikuchi, T. Miyata, S. Tsukagoshi, A. Uranishi, and N. Tomiyama, "Effect of matrix size on the image quality of ultra-high-resolution ct of the lung: comparison of 512× 512, 1024× 1024, and 2048× 2048," *Academic radiology*, vol. 25, no. 7, pp. 869–876, 2018.

[122] S. Kaul, "Myocardial contrast echocardiography: 15 years of research and development," *Circulation*, vol. 96, no. 10, pp. 3745–3760, 1997.

[123] R. Jun-Yan, F. Guo-Tao, W. Cun-Feng, S. Cui-Li, and W. Long, "Measurement of spatial resolution of the micro-ct system," *Chinese Physics C*, vol. 34, no. 3, p. 412, 2010.

[124] E. L. Ritman, "Micro-computed tomography of the lungs and pulmonary-vascular system," *Proceedings of the American Thoracic Society*, vol. 2, no. 6, pp. 477–480, 2005.

[125] A. S. Papazoglou, E. Karagiannidis, D. V. Moysidis, G. Sofidis, A. Bompoti, N. Stalikas, E. Panteris, C. Arvanitidis, M. D. Herrmann, J. S. Michaelson *et al.*, "Current clinical applications and potential perspective of micro-computed tomography in cardiovascular imaging: A systematic scoping review," *Hellenic Journal of Cardiology*, vol. 62, no. 6, pp. 399–407, 2021.

[126] D. P. Clark and C. Badea, "Micro-ct of rodents: state-of-the-art and future perspectives," *Physica medica*, vol. 30, no. 6, pp. 619–634, 2014.

[127] C. Badea, L. Hedlund, and G. Johnson, "Micro-ct with respiratory and cardiac gating: Micro-ct with respiratory and cardiac gating," *Medical physics*, vol. 31, no. 12, pp. 3324–3329, 2004.

[128] J. Buytaert, J. Goyens, D. De Greef, P. Aerts, and J. Dirckx, "Volume shrinkage of bone, brain and muscle tissue in sample preparation for micro-ct and light sheet fluorescence microscopy (lsfm)," *Microscopy and microanalysis*, vol. 20, no. 4, pp. 1208–1217, 2014.

[129] J. Dewanckele, M. Boone, F. Coppens, D. Van Loo, and A. Merkle, "Innovations in laboratory-based dynamic micro-ct to accelerate in situ research," *Journal of Microscopy*, vol. 277, no. 3, pp. 197–209, 2020.

[130] D. P. Frush and K. Applegate, "Computed tomography and radiation: understanding the issues," *Journal of the American College of Radiology*, vol. 1, no. 2, pp. 113–119, 2004.

[131] M. Traub, M. Stevenson, S. McEvoy, G. Briggs, S. K. Lo, S. Leibman, and T. Joseph, "The use of chest computed tomography versus chest x-ray in patients with major blunt trauma," *Injury*, vol. 38, no. 1, pp. 43–47, 2007.

[132] E. Benmalek, J. Elmhamdi, and A. Jilbab, "Comparing ct scan and chest x-ray imaging for covid-19 diagnosis," *Biomedical Engineering Advances*, vol. 1, p. 100003, 2021.

[133] T. Cresson, R. Chav, D. Branchaud, L. Humbert, B. Godbout, B. Aubert, W. Skalli, and J. A. De Guise, "Coupling 2d/3d registration method and statistical model to perform 3d reconstruction from partial x-rays images data," in *2009 Annual International Conference of the IEEE Engineering in Medicine and Biology Society*. IEEE, 2009, pp. 1008–1011.

[134] P. Maken and A. Gupta, "2d-to-3d: a review for computational 3d image reconstruction from x-ray images," *Archives of Computational Methods in Engineering*, vol. 30, no. 1, pp. 85–114, 2023.

[135] Y. Kasten, D. Doktofsky, and I. Kovler, "End-to-end convolutional neural network for 3d reconstruction of knee bones from bi-planar x-ray images," in *Machine Learning for Medical Image Reconstruction: Third International Workshop, MLMIR 2020, Held in Conjunction with MICCAI 2020, Lima, Peru, October 8, 2020, Proceedings 3*. Springer, 2020, pp. 123–133.

[136] H. Villarraga-Gómez and S. T. Smith, "Effect of the number of projections on dimensional measurements with x-ray computed tomography," *Precision Engineering*, vol. 66, pp. 445–456, 2020.

[137] K. M. Hasebroock and N. J. Serkova, "Toxicity of mri and ct contrast agents," *Expert opinion on drug metabolism & toxicology*, vol. 5, no. 4, pp. 403–416, 2009.

[138] N. Khlebtsov and L. Dykman, "Biodistribution and toxicity of engineered gold nanoparticles: a review of in vitro and in vivo studies," *Chemical Society Reviews*, vol. 40, no. 3, pp. 1647–1671, 2011.

[139] L. E. Cole, R. D. Ross, J. M. Tilley, T. Vargo-Gogola, and R. K. Roeder, "Gold nanoparticles as contrast agents in x-ray imaging and computed tomography," *Nanomedicine*, vol. 10, no. 2, pp. 321–341, 2015.

[140] J. A. Jensen, O. Holm, L. J. Jensen, H. Bendsen, H. M. Pedersen, K. Salomonsen, J. Hansen, and S. Nikolov, "Experimental ultrasound system for real-time synthetic imaging," in *1999 IEEE Ultrasonics Symposium. Proceedings. International Symposium (Cat. No. 99CH37027)*, vol. 2. IEEE, 1999, pp. 1595–1599.

[141] P. Sun, Q. Zhou, B. Zhu, D. Wu, C. Hu, J. M. Cannata, J. Tian, P. Han, G. Wang, and K. K. Shung, "Design and fabrication of pin-pmn-pt single-crystal high-frequency ultrasound transducers," *IEEE transactions on ultrasonics, ferroelectrics, and frequency control*, vol. 56, no. 12, pp. 2760–2763, 2009.

[142] A. Fukumoto, "The application of piezoelectric ceramics in diagnostic ultrasound transducers," *Ferroelectrics*, vol. 40, no. 1, pp. 217–230, 1982.

[143] X. M. Lu and T. Proulx, "Single crystals vs. pzt ceramics for medical ultrasound applications," in *IEEE Ultrasonics Symposium*, vol. 1, 2005, pp. 227–230.

[144] L. F. Brown, "Design considerations for piezoelectric polymer ultrasound transducers," *IEEE transactions on ultrasonics, ferroelectrics, and frequency control*, vol. 47, no. 6, pp. 1377–1396, 2000.

[145] T. Ritter, X. Geng, K. K. Shung, P. D. Lopath, S.-E. Park, and T. R. Shrout, "Single crystal pzn/pt-polymer composites for ultrasound transducer applications," *ieee transactions on ultrasonics, ferroelectrics, and frequency control*, vol. 47, no. 4, pp. 792–800, 2000.

[146] M. Lukacs, M. Sayer, and S. Foster, "Single element high frequency (¡ 50 mhz) pzt sol gel composite ultrasound transducers," *IEEE transactions on ultrasonics, ferroelectrics, and frequency control*, vol. 47, no. 1, pp. 148–159, 2000.

[147] O. Oralkan, A. S. Ergun, J. A. Johnson, M. Karaman, U. Demirci, K. Kaviani, T. H. Lee, and B. T. Khuri-Yakub, "Capacitive micromachined ultrasonic transducers: Next-

generation arrays for acoustic imaging?" *IEEE transactions on ultrasonics, ferroelectrics, and frequency control*, vol. 49, no. 11, pp. 1596–1610, 2002.

[148] B. T. Khuri-Yakub and Ö. Oralkan, "Capacitive micromachined ultrasonic transducers for medical imaging and therapy," *Journal of micromechanics and microengineering*, vol. 21, no. 5, p. 054004, 2011.

[149] I. Wygant, "A comparison of cmuts and piezoelectric transducer elements for 2d medical imaging based on conventional simulation models," in *2011 IEEE International Ultrasonics Symposium*. IEEE, 2011, pp. 100–103.

[150] Y. Qiu, J. V. Gigliotti, M. Wallace, F. Griggio, C. E. Demore, S. Cochran, and S. Trolier-McKinstry, "Piezoelectric micromachined ultrasound transducer (pmut) arrays for integrated sensing, actuation and imaging," *Sensors*, vol. 15, no. 4, pp. 8020–8041, 2015.

[151] Y. He, H. Wan, X. Jiang, and C. Peng, "Piezoelectric micromachined ultrasound transducer technology: recent advances and applications," *Biosensors*, vol. 13, no. 1, p. 55, 2022.

[152] H. Persson and C. Hertz, "Acoustic impedance matching of medical ultrasound transducers," *Ultrasonics*, vol. 23, no. 2, pp. 83–89, 1985.

[153] F. S. Foster, "Transducer materials and probe construction," *Ultrasound in medicine & biology*, vol. 26, pp. S2–S5, 2000.

[154] M. Toulemonde, "New beamforming strategy for improved ultrasound imaging: application to biological tissues nonlinear imaging," Ph.D. dissertation, Université Claude Bernard-Lyon I; Università degli studi (Florence, Italie), 2014.

[155] C. Daft, D. Wildes, L. Thomas, L. Smith, R. Lewandowski, W. Leue, K. Rigby, C. Chalek, and W. Hatfield, "A 1.5 d transducer for medical ultrasound," in *1994 proceedings of IEEE Ultrasonics symposium*, vol. 3. IEEE, 1994, pp. 1491–1495.

[156] D. G. Wildes, R. Y. Chiao, C. M. Daft, K. Rigby, L. S. Smith, and K. E. Thomenius, "Elevation performance of 1.25 d and 1.5 d transducer arrays," *IEEE Transactions on Ultrasonics, Ferroelectrics, and Frequency Control*, vol. 44, no. 5, pp. 1027–1037, 1997.

[157] A. H. Dhanaliwala, J. A. Hossack, and F. W. Mauldin, "Assessing and improving acoustic radiation force image quality using a 1.5-d transducer design," *IEEE transactions on ultrasonics, ferroelectrics, and frequency control*, vol. 59, no. 7, pp. 1602–1608, 2012.

[158] L. Curiel, F. Chavrier, R. Souchon, A. Birer, and J. Y. Chapelon, "1.5-d high intensity focused ultrasound array for non-invasive prostate cancer surgery," *IEEE transactions on ultrasonics, ferroelectrics, and frequency control*, vol. 49, no. 2, pp. 231–242, 2002.

[159] L. Curiel, F. Chavrier, B. Gignoux, S. Pichardo, S. Chesnais, and J. Chapelon, "Experimental evaluation of lesion prediction modelling in the presence of cavitation bubbles: intended for high-intensity focused ultrasound prostate treatment," *Medical and Biological Engineering and Computing*, vol. 42, pp. 44–54, 2004.

[160] A. T. Fernandez, K. L. Gammelmark, J. J. Dahl, C. G. Keen, R. C. Gauss, and G. E. Trahey, "Synthetic elevation beamforming and image acquisition capabilities using an 8/spl times/128 1.75 d array," *IEEE transactions on ultrasonics, ferroelectrics, and frequency control*, vol. 50, no. 1, pp. 40–57, 2003.

[161] R. E. Davidsen, J. A. Jensen, and S. W. Smith, "Two-dimensional random arrays for real time volumetric imaging," *Ultrasonic Imaging*, vol. 16, no. 3, pp. 143–163, 1994.

[162] E. Roux, A. Ramalli, P. Tortoli, C. Cachard, M. C. Robini, and H. Liebgott, "2-d ultrasound sparse arrays multidepth radiation optimization using simulated annealing and spiral-array inspired energy functions," *IEEE transactions on ultrasonics, ferroelectrics, and frequency control*, vol. 63, no. 12, pp. 2138–2149, 2016.

[163] M. F. Rasmussen and J. A. Jensen, "3-d ultrasound imaging performance of a row-column addressed 2-d array transducer: A measurement study," in *2013 IEEE International Ultrasonics Symposium (IUS)*. IEEE, 2013, pp. 1460–1463.

[164] G. T. Clement, J. Sun, T. Giesecke, and K. Hynynen, "A hemisphere array for non-invasive ultrasound brain therapy and surgery," *Physics in Medicine & Biology*, vol. 45, no. 12, p. 3707, 2000.

[165] L. Deng, M. A. O'Reilly, R. M. Jones, R. An, and K. Hynynen, "A multi-frequency sparse hemispherical ultrasound phased array for microbubble-mediated transcranial therapy and simultaneous cavitation mapping," *Physics in Medicine & Biology*, vol. 61, no. 24, p. 8476, 2016.

[166] K. Ivanov, M. Kalinina, and Y. I. Levkovich, "Blood flow velocity in capillaries of brain and muscles and its physiological significance," *Microvascular research*, vol. 22, no. 2, pp. 143–155, 1981.

[167] F. Ye, S. Yin, M. Li, Y. Li, and J. Zhong, "In-vivo full-field measurement of microcirculatory blood flow velocity based on intelligent object identification," *Journal of biomedical optics*, vol. 25, no. 1, pp. 016 003–016 003, 2020.

[168] S. H. C. Ortiz, T. Chiu, and M. D. Fox, "Ultrasound image enhancement: A review," *Biomedical Signal Processing and Control*, vol. 7, no. 5, pp. 419–428, 2012.

[169] J. T. Bushberg, J. A. Seibert, E. M. Leidholdt Jr, and J. M. Boone, "The essential physics of medical imaging, lippincott williams & wilkins," *Philadelphia, USA*, 2002.

[170] F. d'Astous and F. Foster, "Frequency dependence of ultrasound attenuation and backscatter in breast tissue," *Ultrasound in medicine & biology*, vol. 12, no. 10, pp. 795–808, 1986.

[171] C. Passmann and H. Ermert, "A 100-mhz ultrasound imaging system for dermatologic and ophthalmologic diagnostics," *IEEE transactions on ultrasonics, ferroelectrics, and frequency control*, vol. 43, no. 4, pp. 545–552, 1996.

[172] S. Ladame and J. Chang, *Bioengineering Innovative Solutions for Cancer*. Academic Press, 2019.

[173] A. Hindi, C. Peterson, and R. G. Barr, "Artifacts in diagnostic ultrasound," *Reports in Medical Imaging*, pp. 29–48, 2013.

[174] A. Ng and J. Swanevelder, "Resolution in ultrasound imaging," *Continuing Education in Anaesthesia Critical Care & Pain*, vol. 11, no. 5, pp. 186–192, 2011.

[175] M. Davidović and M. Božić, "Geometrical, fresnel, and fraunhofer regimes of single-slit diffraction," *The Physics Teacher*, vol. 57, no. 3, pp. 176–178, 2019.

[176] E. Hecht, *Optics*. Pearson Education India, 2012.

[177] B. B. Goldberg, J.-B. Liu, and F. Forsberg, "Ultrasound contrast agents: a review," *Ultrasound in medicine & biology*, vol. 20, no. 4, pp. 319–333, 1994.

[178] D. Cosgrove, "Ultrasound contrast agents: an overview," *European journal of radiology*, vol. 60, no. 3, pp. 324–330, 2006.

[179] A. L. Klibanov, "Ultrasound contrast agents: development of the field and current status," *Contrast agents II: Optical, ultrasound, X-ray and radiopharmaceutical imaging*, pp. 73–106, 2002.

[180] J.-M. Gorce, M. Arditi, and M. Schneider, "Influence of bubble size distribution on the echogenicity of ultrasound contrast agents: A study of sonovue™," *Investigative radiology*, vol. 35, no. 11, pp. 661–671, 2000.

[181] P. Frinking, T. Segers, Y. Luan, and F. Tranquart, "Three decades of ultrasound contrast agents: a review of the past, present and future improvements," *Ultrasound in medicine & biology*, vol. 46, no. 4, pp. 892–908, 2020.

[182] P. Marmottant, S. Van Der Meer, M. Emmer, M. Versluis, N. De Jong, S. Hilgenfeldt, and D. Lohse, "A model for large amplitude oscillations of coated bubbles accounting for buckling and rupture," *The Journal of the Acoustical Society of America*, vol. 118, no. 6, pp. 3499–3505, 2005.

[183] T. Leighton, *The acoustic bubble*. Academic press, 2012.

[184] J. Brown, K. Christensen-Jeffries, S. Harput, G. Zhang, J. Zhu, C. Dunsby, M.-X. Tang, and R. J. Eckersley, "Investigation of microbubble detection methods for super-resolution imaging of microvasculature," *IEEE transactions on ultrasonics, ferroelectrics, and frequency control*, vol. 66, no. 4, pp. 676–691, 2019.

[185] M.-X. Tang, H. Mulvana, T. Gauthier, A. Lim, D. Cosgrove, R. Eckersley, and E. Stride, "Quantitative contrast-enhanced ultrasound imaging: a review of sources of variability," *Interface focus*, vol. 1, no. 4, pp. 520–539, 2011.

[186] T. L. Szabo, *Diagnostic ultrasound imaging: inside out*. Academic press, 2004.

[187] T. Şen, O. Tüfekçioğlu, and Y. Koza, "Mechanical index," *Anatolian journal of cardiology*, vol. 15, no. 4, p. 334, 2015.

[188] M. Lerendegui, K. Riemer, B. Wang, C. Dunsby, and M.-X. Tang, "Bubble flow field: a simulation framework for evaluating ultrasound localization microscopy algorithms," *arXiv preprint arXiv:2211.00754*, 2022.

[189] J. A. Jensen, "Simulation of advanced ultrasound systems using field ii," in *2004 2nd IEEE International Symposium on Biomedical Imaging: Nano to Macro (IEEE Cat No. 04EX821)*. IEEE, 2004, pp. 636–639.

[190] M. A. Parrales, J. M. Fernandez, M. Perez-Saborid, J. A. Kopechek, and T. M. Porter, "Acoustic characterization of monodisperse lipid-coated microbubbles: Relationship between size and shell viscoelastic properties," *The Journal of the Acoustical Society of America*, vol. 136, no. 3, pp. 1077–1084, 2014.

[191] E. Talu, K. Hettiarachchi, S. Zhao, R. L. Powell, A. P. Lee, M. L. Longo, and P. A. Dayton, "Tailoring the size distribution of ultrasound contrast agents: possible method for improving sensitivity in molecular imaging," *Molecular imaging*, vol. 6, no. 6, pp. 7290–2007, 2007.

[192] T. Segers, P. Kruizinga, M. P. Kok, G. Lajoinie, N. De Jong, and M. Versluis, "Monodisperse versus polydisperse ultrasound contrast agents: non-linear response, sensitivity,

and deep tissue imaging potential," *Ultrasound in medicine & biology*, vol. 44, no. 7, pp. 1482–1492, 2018.

[193] A. Helbert, E. Gaud, T. Segers, C. Botteron, P. Frinking, and V. Jeannot, "Monodisperse versus polydisperse ultrasound contrast agents: In vivo sensitivity and safety in rat and pig," *Ultrasound in Medicine & Biology*, vol. 46, no. 12, pp. 3339–3352, 2020.

[194] F. Lin, J. K. Tsuruta, J. D. Rojas, and P. A. Dayton, "Optimizing sensitivity of ultrasound contrast-enhanced super-resolution imaging by tailoring size distribution of microbubble contrast agent," *Ultrasound in medicine & biology*, vol. 43, no. 10, pp. 2488–2493, 2017.

[195] T. V. Bartolotta, M. Midiri, E. Quaia, M. Bertolotto, M. Galia, F. Cademartiri, R. Lagalla, and A. E. Cardinale, "Benign focal liver lesions: spectrum of findings on sonovue-enhanced pulse-inversion ultrasonography," *European radiology*, vol. 15, pp. 1643–1649, 2005.

[196] R. Hoffmann, S. von Bardeleben, F. ten Cate, A. C. Borges, J. Kasprzak, C. Firschke, S. Lafitte, N. Al-Saadi, S. Kuntz-Hehner, M. Engelhardt *et al.*, "Assessment of systolic left ventricular function: a multi-centre comparison of cineventriculography, cardiac magnetic resonance imaging, unenhanced and contrast-enhanced echocardiography," *European heart journal*, vol. 26, no. 6, pp. 607–616, 2005.

[197] J.-J. Hwang and D. H. Simpson, "Two pulse technique for ultrasonic harmonic imaging," Sep. 14 1999, uS Patent 5,951,478.

[198] D. H. Simpson, C. T. Chin, and P. N. Burns, "Pulse inversion doppler: a new method for detecting nonlinear echoes from microbubble contrast agents," *IEEE transactions on ultrasonics, ferroelectrics, and frequency control*, vol. 46, no. 2, pp. 372–382, 1999.

[199] G. A. Brock-Fisher, M. D. Poland, and P. G. Rafter, "Means for increasing sensitivity in non-linear ultrasound imaging systems," Nov. 26 1996, uS Patent 5,577,505.

[200] R. J. Eckersley, C. T. Chin, and P. N. Burns, "Optimising phase and amplitude modulation schemes for imaging microbubble contrast agents at low acoustic power," *Ultrasound in medicine & biology*, vol. 31, no. 2, pp. 213–219, 2005.

[201] T. Misaridis and J. A. Jensen, "Use of modulated excitation signals in medical ultrasound. part i: Basic concepts and expected benefits," *IEEE transactions on ultrasonics, ferroelectrics, and frequency control*, vol. 52, no. 2, pp. 177–191, 2005.

[202] C. Leavens, R. Williams, F. S. Foster, P. N. Burns, and M. D. Sherar, "Golay pulse encoding for microbubble contrast imaging in ultrasound," *IEEE transactions on ultrasonics, ferroelectrics, and frequency control*, vol. 54, no. 10, pp. 2082–2090, 2007.

[203] J. Shen and E. S. Ebbini, "A new coded-excitation ultrasound imaging system. i. basic principles," *IEEE transactions on ultrasonics, ferroelectrics, and frequency control*, vol. 43, no. 1, pp. 131–140, 1996.

[204] P. Phillips, "Contrast pulse sequences (cps): imaging nonlinear microbubbles," in *2001 IEEE Ultrasonics Symposium. Proceedings. An International Symposium (Cat. No. 01CH37263)*, vol. 2. IEEE, 2001, pp. 1739–1745.

[205] M. A. Averkiou, "Tissue harmonic imaging," in *2000 IEEE Ultrasonics Symposium. Proceedings. An International Symposium (Cat. No. 00CH37121)*, vol. 2. IEEE, 2000, pp. 1563–1572.

[206] N. de Jong, A. Bouakaz, and F. J. Ten Cate, "Contrast harmonic imaging," *Ultrasonics*, vol. 40, no. 1-8, pp. 567–573, 2002.

[207] F. Tranquart, N. Grenier, V. Eder, and L. Pourcelot, "Clinical use of ultrasound tissue harmonic imaging," *Ultrasound in medicine & biology*, vol. 25, no. 6, pp. 889–894, 1999.

[208] T. S. Desser and R. B. Jeffrey, "Tissue harmonic imaging techniques: physical principles and clinical applications," in *Seminars in Ultrasound, CT and MRI*, vol. 22, no. 1. Elsevier, 2001, pp. 1–10.

[209] N. de Jong, A. Bouakaz, and P. Frinking, "Harmonic imaging for ultrasound contrast agents," in *2000 IEEE Ultrasonics Symposium. Proceedings. An International Symposium (Cat. No. 00CH37121)*, vol. 2. IEEE, 2000, pp. 1869–1876.

[210] R. J. Eckersley, M.-X. Tang, K. Chetty, and J. V. Hajnal, "Microbubble contrast agent detection using binary coded pulses," *Ultrasound in medicine & biology*, vol. 33, no. 11, pp. 1787–1795, 2007.

[211] J. A. Jensen, S. I. Nikolov, K. L. Gammelmark, and M. H. Pedersen, "Synthetic aperture ultrasound imaging," *Ultrasonics*, vol. 44, pp. e5–e15, 2006.

[212] M. Couade, M. Pernot, M. Tanter, E. Messas, A. Bel, M. Ba, A.-A. Hagège, and M. Fink, "Ultrafast imaging of the heart using circular wave synthetic imaging with phased arrays," in *2009 IEEE International Ultrasonics Symposium*. IEEE, 2009, pp. 515–518.

[213] B. Delannoy, R. Torguet, C. Bruneel, E. Bridoux, J. Rouvaen, and H. Lasota, "Acoustical image reconstruction in parallel-processing analog electronic systems," *Journal of Applied Physics*, vol. 50, no. 5, pp. 3153–3159, 1979.

[214] O. Villemain, J. Baranger, M. K. Friedberg, C. Papadacci, A. Dizeux, E. Messas, M. Tanter, M. Pernot, and L. Mertens, "Ultrafast ultrasound imaging in pediatric and adult cardiology: techniques, applications, and perspectives," *Cardiovascular Imaging*, vol. 13, no. 8, pp. 1771–1791, 2020.

[215] M. Tanter and M. Fink, "Ultrafast imaging in biomedical ultrasound," *IEEE transactions on ultrasonics, ferroelectrics, and frequency control*, vol. 61, no. 1, pp. 102–119, 2014.

[216] G. Montaldo, M. Tanter, J. Bercoff, N. Benech, and M. Fink, "Coherent plane-wave compounding for very high frame rate ultrasonography and transient elastography," *IEEE transactions on ultrasonics, ferroelectrics, and frequency control*, vol. 56, no. 3, pp. 489–506, 2009.

[217] J. Bercoff, G. Montaldo, T. Loupas, D. Savery, F. Mézière, M. Fink, and M. Tanter, "Ultrafast compound doppler imaging: Providing full blood flow characterization," *IEEE*

transactions on ultrasonics, ferroelectrics, and frequency control, vol. 58, no. 1, pp. 134–147, 2011.

[218] A. Hoeks, J. Van de Vorst, A. Dabekaussen, P. Brands, and R. Reneman, "An efficient algorithm to remove low frequency doppler signals in digital doppler systems," *Ultrasonic imaging*, vol. 13, no. 2, pp. 135–144, 1991.

[219] A. P. Kadi and T. Loupas, "On the performance of regression and step-initialized iir clutter filters for color doppler systems in diagnostic medical ultrasound," *IEEE transactions on ultrasonics, ferroelectrics, and frequency control*, vol. 42, no. 5, pp. 927–937, 1995.

[220] E. Chornoboy, "Initialization for improved iir filter performance," *IEEE Transactions on Signal Processing*, vol. 40, no. 3, pp. 543–550, 1992.

[221] S. Bjærum, H. Torp, and K. Kristoffersen, "Clutter filter design for ultrasound color flow imaging," *IEEE transactions on ultrasonics, ferroelectrics, and frequency control*, vol. 49, no. 2, pp. 204–216, 2002.

[222] L. Lovstakken, S. Bjaerum, K. Kristoffersen, R. Haaverstad, and H. Torp, "Real-time adaptive clutter rejection filtering in color flow imaging using power method iterations," *IEEE transactions on ultrasonics, ferroelectrics, and frequency control*, vol. 53, no. 9, pp. 1597–1608, 2006.

[223] D. E. Kruse and K. W. Ferrara, "A new high resolution color flow system using an eigendecomposition-based adaptive filter for clutter rejection," *IEEE transactions on ultrasonics, ferroelectrics, and frequency control*, vol. 49, no. 10, pp. 1384–1399, 2002.

[224] C. Demené, T. Deffieux, M. Pernot, B.-F. Osmanski, V. Biran, J.-L. Gennisson, L.-A. Sieu, A. Bergel, S. Franqui, J.-M. Correas *et al.*, "Spatiotemporal clutter filtering of ultrafast ultrasound data highly increases doppler and fultrasound sensitivity," *IEEE transactions on medical imaging*, vol. 34, no. 11, pp. 2271–2285, 2015.

[225] J. Baranger, B. Arnal, F. Perren, O. Baud, M. Tanter, and C. Demené, "Adaptive spatiotemporal svd clutter filtering for ultrafast doppler imaging using similarity of spatial

singular vectors," *IEEE transactions on medical imaging*, vol. 37, no. 7, pp. 1574–1586, 2018.

[226] P. Song, A. Manduca, J. D. Trzasko, and S. Chen, "Ultrasound small vessel imaging with block-wise adaptive local clutter filtering," *IEEE transactions on medical imaging*, vol. 36, no. 1, pp. 251–262, 2016.

[227] U.-W. Lok, P. Song, J. D. Trzasko, R. Daigle, E. A. Borisch, C. Huang, P. Gong, S. Tang, W. Ling, and S. Chen, "Real time svd-based clutter filtering using randomized singular value decomposition and spatial downsampling for micro-vessel imaging on a verasonics ultrasound system," *Ultrasonics*, vol. 107, p. 106163, 2020.

[228] J. Baranger, J. Aguet, and O. Villemain, "Fast thresholding of svd clutter filter using the spatial similarity matrix and a sum-table algorithm," *IEEE Transactions on Ultrasonics, Ferroelectrics, and Frequency Control*, vol. 70, no. 8, pp. 821–830, 2023.

[229] O. Couture, V. Hingot, B. Heiles, P. Muleki-Seya, and M. Tanter, "Ultrasound localization microscopy and super-resolution: A state of the art," *IEEE transactions on ultrasonics, ferroelectrics, and frequency control*, vol. 65, no. 8, pp. 1304–1320, 2018.

[230] K. Christensen-Jeffries, R. J. Browning, M.-X. Tang, C. Dunsby, and R. J. Eckersley, "In vivo acoustic super-resolution and super-resolved velocity mapping using microbubbles," *IEEE transactions on medical imaging*, vol. 34, no. 2, pp. 433–440, 2014.

[231] J. Yu, L. Lavery, and K. Kim, "Super-resolution ultrasound imaging method for microvasculature in vivo with a high temporal accuracy," *Scientific reports*, vol. 8, no. 1, p. 13918, 2018.

[232] E. Kanoulas, M. Butler, C. Rowley, V. Voulgaridou, K. Diamantis, W. C. Duncan, A. McNeilly, M. Averkiou, H. Wijkstra, M. Mischi *et al.*, "Super-resolution contrast-enhanced ultrasound methodology for the identification of in vivo vascular dynamics in 2d," *Investigative radiology*, vol. 54, no. 8, p. 500, 2019.

[233] G. Zhang, S. Harput, S. Lin, K. Christensen-Jeffries, C. H. Leow, J. Brown, C. Dunsby, R. J. Eckersley, and M.-X. Tang, "Acoustic wave sparsely activated localization mi-

croscopy (awsalm): Super-resolution ultrasound imaging using acoustic activation and deactivation of nanodroplets," *Applied Physics Letters*, vol. 113, no. 1, 2018.

[234] K. Riemer, M. Toulemonde, J. Yan, M. Lerendegui, E. Stride, P. D. Weinberg, C. Dunsby, and M.-X. Tang, "Fast and selective super-resolution ultrasound in vivo with acoustically activated nanodroplets," *IEEE Transactions on Medical Imaging*, vol. 42, no. 4, pp. 1056–1067, 2022.

[235] G. P. Luke, A. S. Hannah, and S. Y. Emelianov, "Super-resolution ultrasound imaging in vivo with transient laser-activated nanodroplets," *Nano letters*, vol. 16, no. 4, pp. 2556–2559, 2016.

[236] F. Dong, J. An, J. Zhang, J. Yin, W. Guo, D. Wang, F. Feng, S. Huang, J. Zhang, and H. Cheng, "Blinking acoustic nanodroplets enable fast super-resolution ultrasound imaging," *ACS nano*, vol. 15, no. 10, pp. 16 913–16 923, 2021.

[237] P. Song, J. M. Rubin, and M. R. Lowerison, "Super-resolution ultrasound microvascular imaging: Is it ready for clinical use?" *Zeitschrift für Medizinische Physik*, 2023.

[238] J. Zhu, C. Zhang, K. Christensen-Jeffries, G. Zhang, S. Harput, C. Dunsby, P. Huang, and M.-X. Tang, "Super-resolution ultrasound localization microscopy of microvascular structure and flow for distinguishing metastatic lymph nodes–an initial human study," *Ultraschall in der Medizin-European Journal of Ultrasound*, vol. 43, no. 06, pp. 592–598, 2022.

[239] S. Harput, K. Christensen-Jeffries, J. Brown, Y. Li, K. J. Williams, A. H. Davies, R. J. Eckersley, C. Dunsby, and M.-X. Tang, "Two-stage motion correction for super-resolution ultrasound imaging in human lower limb," *IEEE transactions on ultrasonics, ferroelectrics, and frequency control*, vol. 65, no. 5, pp. 803–814, 2018.

[240] G. Goudot, A. Jimenez, N. Mohamedi, J. Sitruk, L. Khider, H. Mortelette, C. Papadacci, F. Hyafil, M. Tanter, E. Messas *et al.*, "Assessment of takayasu's arteritis activity by ultrasound localization microscopy," *Ebiomedicine*, vol. 90, 2023.

[241] N. Renaudin, C. Demené, A. Dizeux, N. Ialy-Radio, S. Pezet, and M. Tanter, "Functional ultrasound localization microscopy reveals brain-wide neurovascular activity on a microscopic scale," *Nature methods*, vol. 19, no. 8, pp. 1004–1012, 2022.

[242] F. Lin, S. E. Shelton, D. Espíndola, J. D. Rojas, G. Pinton, and P. A. Dayton, "3-d ultrasound localization microscopy for identifying microvascular morphology features of tumor angiogenesis at a resolution beyond the diffraction limit of conventional ultrasound," *Theranostics*, vol. 7, no. 1, p. 196, 2017.

[243] J. Zhu, E. M. Rowland, S. Harput, K. Riemer, C. H. Leow, B. Clark, K. Cox, A. Lim, K. Christensen-Jeffries, G. Zhang *et al.*, "3d super-resolution us imaging of rabbit lymph node vasculature in vivo by using microbubbles," *Radiology*, vol. 291, no. 3, pp. 642–650, 2019.

[244] K. Christensen-Jeffries, J. Brown, P. Aljabar, M. Tang, C. Dunsby, and R. J. Eckersley, "3-d in vitro acoustic super-resolution and super-resolved velocity mapping using microbubbles," *IEEE transactions on ultrasonics, ferroelectrics, and frequency control*, vol. 64, no. 10, pp. 1478–1486, 2017.

[245] Y. Desailly, O. Couture, M. Fink, and M. Tanter, "Sono-activated ultrasound localization microscopy," *Applied Physics Letters*, vol. 103, no. 17, 2013.

[246] B. Heiles, M. Correia, V. Hingot, M. Pernot, J. Provost, M. Tanter, and O. Couture, "Ultrafast 3d ultrasound localization microscopy using a 32×32 matrix array," *IEEE Transactions on Medical Imaging*, vol. 38, no. 9, pp. 2005–2015, 2019.

[247] C. Zhang, S. Lei, A. Ma, B. Wang, S. Wang, J. Liu, D. Shang, Q. Zhang, Y. Li, H. Zheng *et al.*, "Evaluation of tumor microvasculature with 3d ultrasound localization microscopy based on 2d matrix array," *European Radiology*, pp. 1–10, 2024.

[248] A. Ramalli, E. Boni, A. S. Savoia, and P. Tortoli, "Density-tapered spiral arrays for ultrasound 3-d imaging," *IEEE Transactions on ultrasonics, ferroelectrics, and frequency control*, vol. 62, no. 8, pp. 1580–1588, 2015.

[249] S. Harput, K. Christensen-Jeffries, A. Ramalli, J. Brown, J. Zhu, G. Zhang, C. H. Leow, M. Toulemonde, E. Boni, P. Tortoli *et al.*, "3-d super-resolution ultrasound imaging with a 2-d sparse array," *IEEE transactions on ultrasonics, ferroelectrics, and frequency control*, vol. 67, no. 2, pp. 269–277, 2019.

[250] A. Chavignon, B. Heiles, V. Hingot, C. Orset, D. Vivien, and O. Couture, "3d transcranial ultrasound localization microscopy in the rat brain with a multiplexed matrix probe," *IEEE Transactions on Biomedical Engineering*, vol. 69, no. 7, pp. 2132–2142, 2021.

[251] NHS England and NHS Improvment, "Diagnostic Imaging Dataset Statistical Release," *NHS England*, vol. 1, 2020. [Online]. Available: https://www.england.nhs.uk/statistics/wp-content/uploads/sites/2/2015/08/Provisional-Monthly-Diagnostic-Imaging-Dataset-Statistics-2016-03-17.pdf

[252] J. A. Jensen, D. Lyngby, P. Medical, B. Engineering, J. A. Jensen, and I. Technology, "Paper presented at the 10th Nordic-Baltic Conference on Biomedical Imaging : Field : A Program for Simulating Ultrasound Systems Field : A Program for Simulating Ultrasound Systems," vol. 34, pp. 351–353, 1996.

[253] B. Heiles, A. Chavignon, V. Hingot, P. Lopez, E. Teston, and O. Couture, "Performance benchmarking of microbubble-localization algorithms for ultrasound localization microscopy," *Nature Biomedical Engineering*, 2022.

[254] S. Harput, K. Christensen-jeffries, A. Ramalli, J. Brown, J. Zhu, G. Zhang, C. H. Leow, M. Toulemonde, E. Boni, P. Tortoli, R. J. Eckersley, C. Dunsby, and M.-x. Tang, "3-D Super-Resolution Ultrasound Imaging with a 2-D Sparse Array," *IEEE Transactions on Ultrasonics, Ferroelectrics, and Frequency Control*, vol. PP, p. 1, 2019.

[255] S. Lin, A. Shah, J. Hernández-Gil, A. Stanziola, B. I. Harriss, T. O. Matsunaga, N. Long, J. Bamber, and M.-X. Tang, "Optically and acoustically triggerable sub-micron phase-change contrast agents for enhanced photoacoustic and ultrasound imaging," *Photoacoustics*, vol. 6, pp. 26–36, 2017.

[256] T. Deffieux, M. Tanter, I. Cohen, O. Baud, V. Biran, M. Pernot, A. Bergel, C. Demene, J.-M. Correas, B.-F. Osmanski, L.-A. Sieu, J.-L. Gennisson, and S. Franqui, "Spatiotemporal Clutter Filtering of Ultrafast Ultrasound Data Highly Increases Doppler and fUltrasound Sensitivity," *IEEE Transactions on Medical Imaging*, vol. 34, no. 11, pp. 2271–2285, 2015.

[257] P. Song, J. D. Trzasko, A. Manduca, B. Qiang, R. Kadirvel, D. F. Kallmes, and S. Chen, "Accelerated Singular Value-Based Ultrasound Blood Flow Clutter Filtering with Randomized Singular Value Decomposition and Randomized Spatial Downsampling," *IEEE Transactions on Ultrasonics, Ferroelectrics, and Frequency Control*, vol. 64, no. 4, pp. 706–716, 2017.

[258] J. Baranger, B. Arnal, F. Perren, O. Baud, M. Tanter, and C. Demene, "Adaptive Spatiotemporal SVD Clutter Filtering for Ultrafast Doppler Imaging Using Similarity of Spatial Singular Vectors," *IEEE Transactions on Medical Imaging*, vol. 37, no. 7, 2018.

[259] K. Christensen-Jeffries, O. Couture, P. A. Dayton, Y. C. Eldar, K. Hynynen, F. Kiessling, M. O'Reilly, G. F. Pinton, G. Schmitz, M.-X. Tang, M. Tanter, and R. J. van Sloun, "Super-resolution Ultrasound Imaging," *Ultrasound in Medicine & Biology*, vol. 46, no. 4, pp. 865–891, Apr. 2020. [Online]. Available: https://linkinghub.elsevier.com/retrieve/pii/S0301562919315959

[260] D. Ackermann and G. Schmitz, "Detection and tracking of multiple microbubbles in ultrasound B-mode images," *IEEE Transactions on Ultrasonics, Ferroelectrics, and Frequency Control*, vol. 63, no. 1, pp. 72–82, 2016.

[261] J. Yan, T. Zhang, J. Broughton-Venner, P. Huang, and M. X. Tang, "Super-Resolution Ultrasound Through Sparsity-Based Deconvolution and Multi-Feature Tracking," *IEEE Transactions on Medical Imaging*, vol. 0062, no. c, pp. 1–10, 2022.

[262] N. Renaudin, S. Pezet, N. Ialy-Radio, C. Demene, and M. Tanter, "Backscattering amplitude in ultrasound localization microscopy," *bioRxiv*, pp. 2023–04, 2023.

[263] H. Favre, M. Pernot, M. Tanter, and C. Papadacci, "Boosting transducer matrix sensitivity for 3D large field ultrasound localization microscopy using a multi-lens diffracting layer: a simulation study," *Physics in Medicine & Biology*, vol. 67, no. 8, p. 085009, 2022.

[264] T. L. Christiansen, M. F. Rasmussen, J. P. Bagge, L. N. Moesner, J. A. Jensen, and E. V. Thomsen, "3-d imaging using row–column-addressed arrays with integrated apodization— part ii: transducer fabrication and experimental results," *IEEE Transactions on Ultrasonics, Ferroelectrics, and Frequency Control*, vol. 62, no. 5, pp. 959–971, 2015.

[265] A. Bar-Zion, O. Solomon, C. Tremblay-Darveau, D. Adam, and Y. C. Eldar, "Sushi: Sparsity-based ultrasound super-resolution hemodynamic imaging," *IEEE transactions on ultrasonics, ferroelectrics, and frequency control*, vol. 65, no. 12, pp. 2365–2380, 2018.

[266] J. Yan, B. Wang, K. Riemer, J. Hansen-Shearer, M. Lerendegui, M. Toulemonde, C. J. Rowlands, P. D. Weinberg, and M.-X. Tang, "Fast 3d super-resolution ultrasound with adaptive weight-based beamforming," *IEEE Transactions on Biomedical Engineering*, 2023.

[267] M. Versluis, E. Stride, G. Lajoinie, B. Dollet, and T. Segers, "Ultrasound Contrast Agent Modeling: A Review," *Ultrasound in Medicine and Biology*, vol. 46, no. 9, pp. 2117–2144, 2020.

[268] J. J. Dahl, S. A. McAleavey, G. F. Pinton, M. S. Soo, and G. E. Trahey, "Adaptive imaging on a diagnostic ultrasound scanner at quasi real-time rates," *IEEE transactions on ultrasonics, ferroelectrics, and frequency control*, vol. 53, no. 10, pp. 1832–1843, 2006.

[269] A. Aguirre, P. Guo, J. Gamelin, S. Yan, M. M. Sanders, M. Brewer, and Q. Zhu, "Coregistered three-dimensional ultrasound and photoacoustic imaging system for ovarian tissue characterization," *Journal of biomedical optics*, vol. 14, no. 5, pp. 054 014–054 014, 2009.

[270] "Optically and acoustically triggerable sub-micron phase-change contrast agents for enhanced photoacoustic and ultrasound imaging," *Photoacoustics*, vol. 6, pp. 26–36, 2017. [Online]. Available: http://dx.doi.org/10.1016/j.pacs.2017.04.001

[271] J. Brook, M.-y. Kim, S. Koutsoftidis, D. Pitcher, D. Agha-Jaffar, A. Sufi, C. Jenkins, K. Tzortzis, S. Ma, R. J. Jabbour *et al.*, "Development of a pro-arrhythmic ex vivo intact human and porcine model: cardiac electrophysiological changes associated with cellular uncoupling," *Pflügers Archiv-European Journal of Physiology*, vol. 472, pp. 1435–1446, 2020.

[272] D. Kroon, "B-spline grid, image and point based registration-file exchange-matlab central," *http://www. mathworks. com/matlabcentral/fileexchange/20057/.*

[273] D. Rueckert, L. I. Sonoda, C. Hayes, D. L. Hill, M. O. Leach, and D. J. Hawkes, "Non-rigid registration using free-form deformations: application to breast mr images," *IEEE transactions on medical imaging*, vol. 18, no. 8, pp. 712–721, 1999.

[274] L. Milecki, J. Porée, H. Belgharbi, C. Bourquin, R. Damseh, P. Delafontaine-Martel, F. Lesage, M. Gasse, and J. Provost, "A deep learning framework for spatiotemporal ultrasound localization microscopy," *IEEE Transactions on Medical Imaging*, vol. 40, no. 5, pp. 1428–1437, 2021.

[275] K. G. Brown and K. Hoyt, "Evaluation of nonlinear contrast pulse sequencing for use in super-resolution ultrasound imaging," *IEEE transactions on ultrasonics, ferroelectrics, and frequency control*, vol. 68, no. 11, pp. 3347–3361, 2021.

[276] B. Wang, J. Yan, K. Riemer, M. Toulemonde, J. Hansen-Shearer, and M.-X. Tang, "Comparison of localization methods for 3d super-resolution ultrasound imaging," in *2022 IEEE International Ultrasonics Symposium (IUS)*. IEEE, 2022, pp. 1–3.

[277] K. Christensen-Jeffries and R. J. Eckersley, "Physics of microbubble contrast agents," *Contrast-Enhanced Ultrasound in Pediatric Imaging*, pp. 1–11, 2021.

[278] M. Kaya, S. Feingold, K. Hettiarachchi, A. P. Lee, and P. A. Dayton, "Acoustic responses of monodisperse lipid encapsulated microbubble contrast agents produced by flow focusing," *Bubble Science, Engineering & Technology*, vol. 2, no. 2, pp. 33–40, 2010.

[279] D. Ghosh, F. Xiong, S. R. Sirsi, P. W. Shaul, R. F. Mattrey, and K. Hoyt, "Toward optimization of in vivo super-resolution ultrasound imaging using size-selected microbubble contrast agents," *Medical physics*, vol. 44, no. 12, pp. 6304–6313, 2017.

[280] L. Shen, W. Zhao, and L. Xing, "Patient-specific reconstruction of volumetric computed tomography images from a single projection view via deep learning," *Nature biomedical engineering*, vol. 3, no. 11, pp. 880–888, 2019.